Quantum transport at oxide interfaces

Rincon Vieira Lugarinho Monteiro, Mafalda

DOI
10.4233/uuid:9a580a83-22e5-461b-b9d4-5de9a2e6fe3f

Publication date
2019

Document Version
Final published version

Citation (APA)
Rincon Vieira Lugarinho Monteiro, M. (2019). *Quantum transport at oxide interfaces*. [Dissertation (TU Delft), Delft University of Technology]. https://doi.org/10.4233/uuid:9a580a83-22e5-461b-b9d4-5de9a2e6fe3f

Quantum Transport at Oxide Interfaces

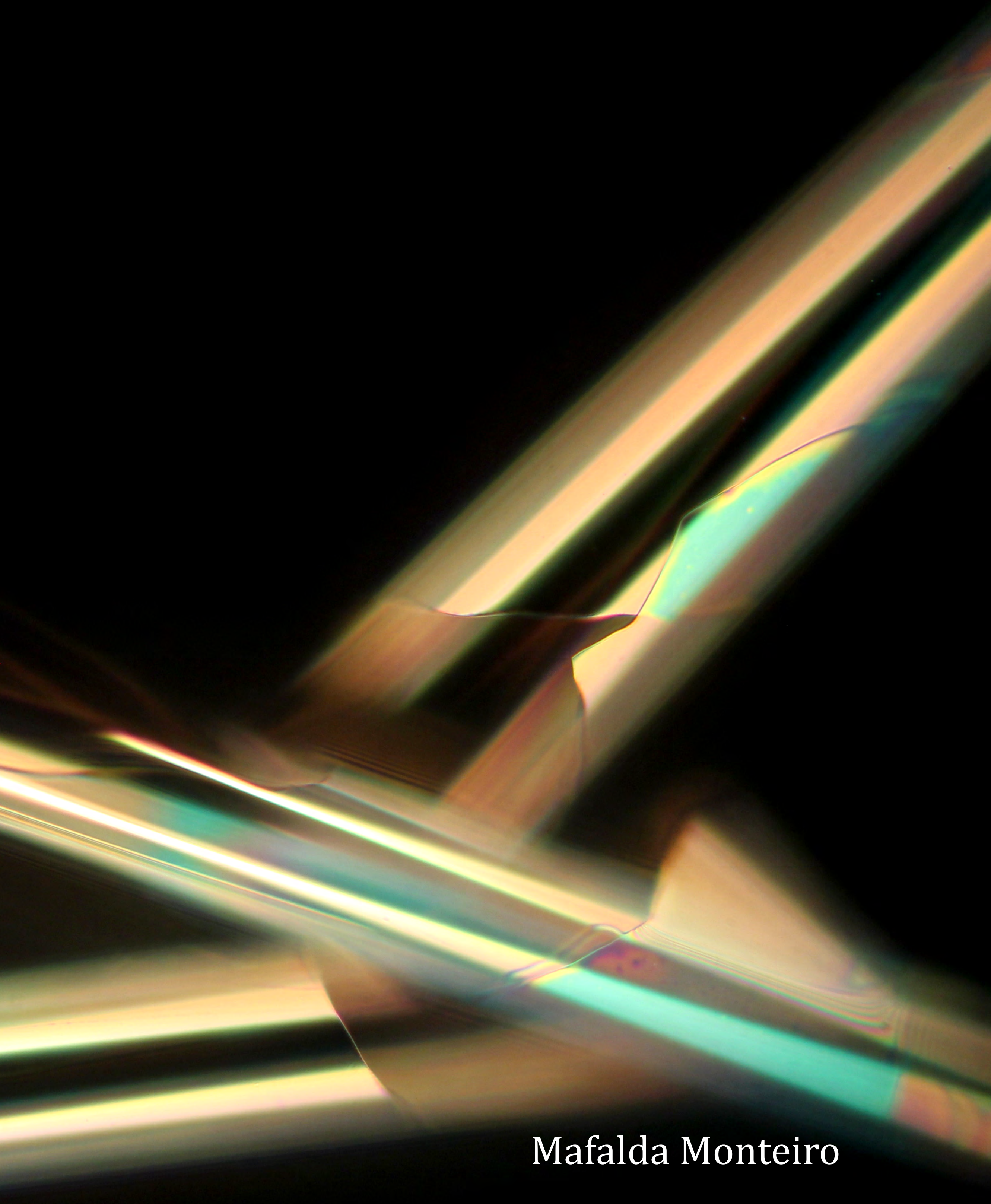

Mafalda Monteiro

QUANTUM TRANSPORT AT OXIDE INTERFACES

QUANTUM TRANSPORT AT OXIDE INTERFACES

Dissertation

for the purpose of obtaining the degree of doctor
at Delft University of Technology
by the authority of the Rector Magnificus Prof. dr. ir. T. H. J. J. van der Hagen,
Chair of the Board for Doctorates,
to be defended publicly on Monday, 21 January 2019 at 15:00

by

Ana Mafalda RINCON VIEIRA LUGARINHO MONTEIRO

Master of Science in Physics Engineering,
Universidade do Porto, Portugal,
born in Vila Real, Portugal.

This dissertation has been approved by

Promotor: Dr. A. D. Caviglia
Promotor: Prof. dr. ir. H. S. J. van der Zant

Composition of the doctoral committee:

Rector Magnificus,	Chairperson
Dr. A. D. Caviglia,	Delft University of Technology
Prof. dr. ir. H. S. J. van der Zant,	Delft University of Technology
Independent members:	
Prof. dr. Ya. Blanter,	Delft University of Technology
Prof. dr. M. Gabay,	Université Paris-Sud
Prof. dr. ir. J. W. M. Hilgenkamp,	University of Twente
Dr. A. McCollam,	Radboud University
Dr. G. Herranz,	Institut de Ciència de Materials de Barcelona (Spain)
Prof. dr. A. F. Otte,	Delft University of Technology *(reserve)*

This work is part of the research programme of the Foundation for Fundamental Research on Matter (FOM), which is part of the Netherlands Organisation for Scientific Research (NWO).

Keywords: Complex oxide interfaces, magnetotransport, field-effect, superconductivity, electronic correlations, spin–orbit coupling, free-standing oxides

Printed by: Gildeprint, Enschede

Front & Back: Dark-field optical image of an epitaxially grown, rolled-up $SrTiO_3$ layer.

Casimir PhD series 2018-51

ISBN 978-90-8593-382-3

An electronic version of this dissertation is available at
`http://repository.tudelft.nl/`.

All men dream, but not equally.
Those who dream by night in the dusty recesses of their minds,
wake in the day to find that it was vanity: but the dreamers of the day are dangerous men,
for they may act on their dreams with open eyes, to make them possible.

T. E. Lawrence

CONTENTS

SUMMARY

The realization of interfaces between different transition metal oxides has heralded a new era of materials and physics research. Notably, it enabled a uniquely diverse set of coexisting physical properties to be combined with an ever-increasing degree of experimental control.

The primary focus of this thesis is the celebrated interface between the two wide band-gap insulators $LaAlO_3$ and $SrTiO_3$, which exhibits a variety of phenomena such as conductivity, superconductivity and spin–orbit coupling — all of which are gate-tunable, demonstrating the promise of this system for fundamental research and technological applications alike.

We start by discussing the role of spin–orbit coupling in the magnetotransport properties of the system. Namely, we show how it can drive a giant in-plane magnetoresistance. On a more technically challenging perspective, we realize tunable Josephson junctions by means of lateral confinement and local side-gating. This technique, due to its simplicity, can be expanded to a broad group of interfacial systems. We then investigate $LaAlO_3/SrTiO_3$ interfaces along the (111) crystallographic direction, discovering that it condenses into a superconducting ground state and elucidating the important role played by electronic correlations.

Finally, this thesis ends with a twist to the story. Moving away from epitaxial interfaces, we employ an innovative technique to obtain free-standing oxide films by etching a water-soluble sacrificial buffer layer. This exciting development paves the way to integrating complex oxides with van der Waals materials and engineering new phases in hybrid devices.

SAMENVATTING

De realisatie van grensvlakken tussen verschillende transitiemetaaloxides heeft een nieuw tijdperk van materiaal en natuurkundig onderzoek teweeggebracht. Het liet met name toe dat een unieke set van naast elkaar bestaande fysische eigenschappen kon worden gecombineerd met een toenemende mate van experimentele controle.

De primaire focus van dit proefschrift is het gevierde grensvlak tussen de twee isolatoren $LaAlO_3$ en $SrTiO_3$ dat een verscheidenheid aan verschijnselen vertoont zoals geleiding, supergeleiding en spin-baankoppeling — allen zijn controleerbaar door het aanbrengen van schakelspanningen, wat getuigt van het potentieel van dit systeem voor fundamenteel onderzoek en technologische toepassingen.

We beginnen door de rol van spin-baankoppeling in de magnetische transporteigenschappen van het systeem te bediscussiëren. We laten namelijk zien hoe het een enorme magnetoweerstand in het vlak teweeg kan brengen. Op een meer technologisch uitdagend vlak realiseren we controleerbare Josephson juncties bij wijze van laterale begrenzing en het lokaal aanbrengen van schakelspanningen. Deze techniek kan door zijn eenvoud toegepast worden op een brede groep grensvlaksystemen. We bestuderen vervolgens $LaAlO_3/SrTiO_3$ grensvlakken in de (111) kristallografische richting en ontdekken dat het in een supergeleidende grondtoestand condenseert, en verhelderen de belangrijke rol die ingenomen wordt door elektronische correlaties.

Uiteindelijk eindigt dit proefschrift met een onverwachte wending. We gaan weg van epitaxiale grensvlakken en gebruiken een innovatieve techniek om vrijstaande oxide films te bemachtigen door een wateroplosbare bufferlaag weg te etsen. Deze spannende ontwikkeling maakt de weg vrij om complexe oxides te integreren met van der Waals materialen en nieuwe toestanden in hybride apparaten te ontwerpen.

LIST OF ABBREVIATIONS

2D	two-dimensional
2DES	two-dimensional electron system
a.u.	arbitrary units
AFM	atomic force microscopy
AHE	anomalous Hall effect
BKT	Berenzinskii–Kosterlitz–Thouless
BZ	Brillouin zone
HLN	Hikami–Larkin–Nagaoka
JJ	Josephson junction
LAO	$LaAlO_3$
MF	Maekawa–Fukuyama
MIT	metal–insulator transition
MR	magnetoresistance
PDMS	polydimethylsiloxane
PLD	pulsed laser deposition
QCP	quantum critical point
RHEED	reflection high-energy electron diffraction
SAO	$Sr_3Al_2O_6$
SIO	$SrIrO_3$
SOC	spin–orbit coupling
SQUID	superconducting quantum interference device
STO	$SrTiO_3$
TEM	transmission electron microscopy
TMO	transition metal oxide
u.c.	unit cell

UCF	universal conductance fluctuations
XAS	X-ray absorption spectroscopy
XRD	X-ray diffraction

1

INTRODUCTION

Where nature finishes producing its own species, man begins,
using natural things and in harmony with this very nature,
to create an infinity of species.

Leonardo da Vinci

THE fundamental importance of materials is made clear from the naming of ages of civilizations – the stone, iron and bronze ages – with each new era being brought about by a new material. In the Stone Age, people built and used simple stone tools which enabled them to improve their lives and advance their civilization. This age saw the Agricultural Revolution begin, during which humans began the systematic husbandry of plants and animals [1]. As agriculture advanced, most humans transitioned from a nomadic to a settled lifestyle as farmers in permanent settlements, fundamentally changing the human lifestyle. In the Bronze Age, the development of advanced metalworking enabled a number of technological innovations which profoundly altered the landscape of the civilization, ultimately making the Stone Age obsolete. Iron and steel were the defining materials of the Iron Age, allowing engineers to give full rein to their dreams of creating suspension bridges, railways, steam engines and passenger liners. Isambard Kingdom Brunel used them as a manifesto to transform the landscape and sow the seeds of modernism [2, 3]. Rapid and farther transportation became possible, and people then explored many lands and seas, otherwise unreachable before.

1.1. THE SILICON AGE

A profound change in direction was initiated at the end of the 19^{th} century by a remarkable event: the discovery of the electron [4]. In his laboratory in Cambridge, J. J. Thomson was performing detailed fundamental experiments to try to determine the composition of the mysterious radiation emitted by negative metallic electrodes — so-called “cathode rays”. Thomson was able to show that the rays are made of negatively charged particles, with a mass almost 2000 times lighter than a hydrogen atom. Soon it was recognized that Thomson’s cathode ray particles are the same as those that carry current in wires and they became known as electrons.

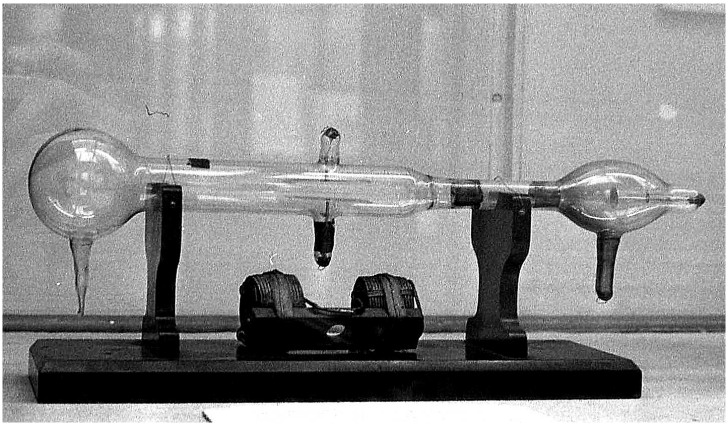

Figure 1.1: Glass apparatus (electromagnetic tube) used by J. J. Thomson to measure the ratio of charge to mass of cathode rays. Science Museum, London, 1975. Photo by I. Peterson.

For his fundamental studies, Thomson developed glass tubes strong enough to withstand the pumping out of most of the air molecules (see Fig. 1.1), which provided engineers with the design for the first electronic devices: three-terminal devices called vacuum tubes or triodes [5] which could be used as switches, for amplification, and to make simple logic circuits. Vacuum tubes offered the first glimpse of the tremendous capabilities that might be provided by electrical circuits. Since, however, they were bulky, sometimes unreliable and devoured energy, they also provided device physicists and materials scientists with a strong incentive to find a route to a more convenient three-terminal device. The resulting development of the semiconductor transistor [6, 7] — first in germanium and soon after in silicon due to its superior material properties — is certainly one of the most significant breakthroughs of the 20th century.

As a result, our current time is often referred to as the *Silicon Age*, with silicon transistors forming the core of much of the microelectronics that enable our modern way of life. Devices have gotten smaller, faster, more efficient, more powerful, and cheaper. However, as the size of transistors — the building blocks of electronics — approaches the size of the individual silicon atoms, we will run into fundamental physical limits [8] and the silicon revolution will inevitably be forced to come to an end. Might there still be a future for silicon, provided it is given new capabilities? Or has the time come when a replacement for silicon can no longer be avoided? Moving away from silicon, the subject of this thesis is the richness of the electronic phases and enhanced functionality afforded by transition metal oxides (TMOs).

1.2. AN EMERGENT PHASE OF ELECTRONICS

The introduction of interfaces into semiconductor structures spawned numerous semiconductor devices of immense utility, at the same time as it allowed a multitude of fascinating discoveries in fundamental science. Transistors, lasers, and solar cells all exploit interfacial phenomena — interfaces enable data processing, memory, and electronic communication. Herbert Kroemer began his Nobel lecture by stating [9]:

> *"Often, it may be said that the interface is the device."*,

but away from interfaces, in the bulk of the material, the behavior of electrons in semiconductors such as silicon is less exciting. The electrons zip through the crystal lattice essentially as independent, free particles. In contrast, the electron interactions in the bulk of TMOs give rise to spectacular phenomena, such as colossal magnetoresistance [10, 11] and high-temperature superconductivity. These phenomena arise in oxides from regularly spaced ions interacting with the electrons, from the unique electronic character of oxygen ions, and from the electronic correlations — interactions among the electrons themselves, which make them deviate from free-particle behavior. By analogy with the silicon case, it is tantalizing to incorporate well-defined interfaces into TMOs to generate completely novel phenomena.

1.2.1. ELECTRONIC CORRELATIONS: INTERFACES MATTER

The electric and magnetic properties of TMOs are often dominated by electrons in d-orbitals. The large Coulomb repulsion between electrons accommodated in the spatially constrained d-orbitals tends to block the motion of electrons from one atom to another, and the electrons are highly interacting. Just like interacting atoms and molecules, the correlated electrons can form solid (insulator), liquid (metal), and superfluid (superconductor) states inside the solid. The presence of the electron's three degrees of freedom — charge, spin, and orbital — enrich these electronic phases further. Complex combinations of charge-, spin-, and orbital-ordered states indeed appear in the phase diagrams of TMOs.

The strength and relevance of the correlations among electrons are characterized by parameters such as the on-site Coulomb repulsion energy U and exchange energy J [12]. As these parameters are sensitive to the local ionic structure, they are usually highly susceptible to changes occurring at interfaces [13]. One exciting example is an interface–driven reduction of the electronic screening, possibly caused by the broken periodicity of the ion lattice, leading to an enhanced on-site Coulomb energy U.

1.3. LAO/STO: A CONDUCTING LAYER BETWEEN TWO INSULATORS

The ability of creating complex oxide heterostructures — interfaces formed between two different TMOs — has heralded a new era of materials and physics research [14]. The physical phenomena that emerge at oxide interfaces go well beyond those exhibited by conventional semiconductor interfaces because new and largely unexplored physics becomes relevant, enabling novel electronic phases. Moreover, they represent an ideal configuration for future electronic applications, since (i) they work at room temperature, (ii) can be tuned by externally applied electric fields [15] and (iii) feature high carrier mobilities.

The best example is the seminal discovery of a conducting electron system at interfaces between the wide band-gap band insulators $LaAlO_3$ (LAO) and $SrTiO_3$ (STO) [16]. If LAO is epitaxially grown on the TiO_2-terminated and (001)-oriented surface of STO, a conducting electron-doped (n-type) sheet is generated at the interface.

Typical mobilities of the electron system at the LAO/STO interface are $\sim 1\,\mathrm{cm^2V^{-1}s^{-1}}$ and $\sim 10^3\,\mathrm{cm^2V^{-1}s^{-1}}$ at room and low temperature, respectively. Carrier densities are usually in the range of $10^{13}\,\mathrm{cm^{-2}}$ [17]. In the direction perpendicular to the interface, the conducting sheet is at most a few nanometers thick [18]. These characteristics, which differ remarkably from the typical properties of semiconductor interfaces, are exhibited by samples that are annealed in an oxygen atmosphere after epitaxial growth. Under these conditions, the conducting sheet generated by electronic reconstruction is not shunted by electrons arising from doping of STO by oxygen vacancies [19].

In recent years, the LAO/STO electron mobility has been enhanced by surface engineering or film growth control. These techniques, which enabled carrier mobilities of $\sim 10^4\,\mathrm{cm^2V^{-1}s^{-1}}$, include:

- lowering the deposition temperature [20],
- writing charges on the sample surface [21],
- introduction of a $SrCuO_2$ cap layer of a few unit cells [22],
- modulation doping [23].

1.3.1. POLAR CATASTROPHE AND ELECTRONIC RECONSTRUCTION

One of the key features of the LAO/STO system is the polar discontinuity that occurs at the interface. As shown in Fig. 1.2a, along the (001) direction STO is composed of alternating neutral TiO_2 and SrO planes, while LAO is composed of alternating AlO_2 and LaO planes which are charged $-e$ and $+e$ (per surface unit cell), respectively. The resulting polar discontinuity leads to an electric field inside the LAO layer and an electrostatic potential that grows as the LAO layer thickness increases. This is the so-called "polar catastrophe scenario" that leads to an instability as the LAO layer thickness is increased [24]. The voltage grows with the LAO thickness to such large values that, above a critical LAO thickness of 3 unit cells, electrons reduce their Coulomb energy by moving from the LAO sheet to the interface, as depicted in Fig. 1.2b. This process leaves the overall structure neutral, with the Ti ion at the interface becoming $Ti^{3.5+}$, and the potential no longer diverges.

To cancel the polar field, a charge transfer of exactly $1/2e$ per surface unit cell is necessary, which translates into a carrier density of $3 \times 10^{14}\,cm^{-2}$. However, as previously mentioned, experimentally measured carrier concentrations from the Hall effect are generally an order of magnitude lower [25, 26], raising the question: where are the missing electrons? One explanation proposes that there are two populations of electrons at the interface, one that is tightly bound to the interface and strongly localized through impurities and defects, while the other is more loosely bound and mobile [27, 28].

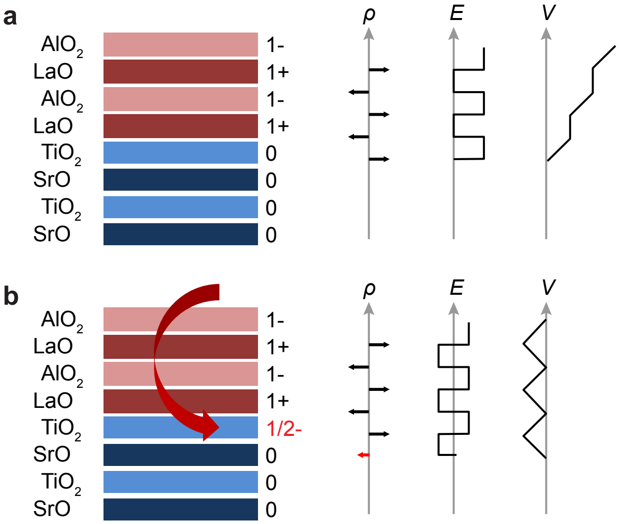

Figure 1.2: (a) Unreconstructed interface. Left: charge distribution across the ionic planes. Right: non-negative electric-field (E) and resulting electrostatic potential (V), which diverges with the LAO thickness. (b) Reconstructed interface. Left: charge distribution after half and electron per unit cell is transferred to the last TiO_2 layer. Right: electric field oscillates about 0 and the electrostatic potential remains finite. Reproduced from [24].

Other mechanisms that could give rise to a conducting interface have been discussed, such as La/Sr intermixing at the interface [29] or oxygen vacancies in STO [17, 30, 31].

One point worth noticing is that while such mechanisms may lead to STO doping, that is to conduction, they do not fix the polar catastrophe problem.

Recently, new models have been proposed to explain the occurrence of the 2DES at the LAO/STO interface [32–35]. Although the polar discontinuity is still the driving force for the appearance of a conducting layer, the novelty in these approaches is that the mechanism for charge transfer is not a Zener breakdown but the formation, at the critical thickness, of oxygen vacancies on the top surface of LAO (rather than at the interface) — each neutral oxygen vacancy gives two electrons that are transferred to the interface. These models provide an explanation as to why the top surface is insulating and may also explain why the charge transfer is abrupt at the critical thickness.

Interesting consequences of the polar catastrophe scenario pertain to interfaces oriented along other crystallographic directions. Later in this thesis, we will discuss extensively the case of (111)-oriented interfaces.

1.3.2. GATE-TUNABLE SUPERCONDUCTIVITY

In 2007, superconductivity was discovered at the LAO/STO interface with a critical temperature of ~ 250 mK [36]. Shortly after, a back gate geometry as depicted in Fig. 1.3a was used to tune the carrier density by electric field-effect. Notably, it was discovered that applying an electric field also allows one to switch back and forth between a zero resistance state and a resistive state at low temperature [15]. A typical plot of T_c versus back gate voltage is shown in Fig. 1.3b. Salient features of this phase diagram include (i) a quantum critical point (QCP) separating a localized from a superconducting region at low dopings, (ii) a dome shaped curve culminating at $T_c^{max} \sim 300$ mK and (iii) a superconductor to metal boundary at higher dopings.

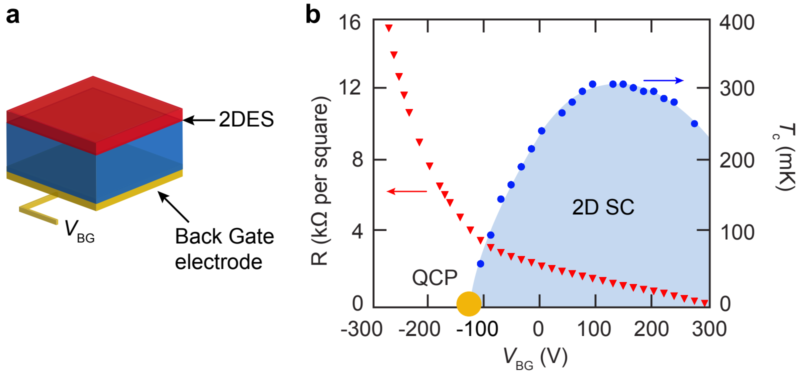

Figure 1.3: (a) Schematic of a field-effect device at LAO/STO interface using a back-gate geometry. (b) Gate-tunable superconductivity at LAO/STO, reproduced from [15]. Critical temperature T_c (right axis, blue dots) is plotted against gate voltage, revealing the superconducting region of the phase diagram. Also plotted is normal-state sheet resistance, (left axis, red triangles) as a function of gate voltage.

1.3.3. ELECTRONIC STRUCTURE

The confinement of the electrons at the (001) interface has important consequences on the electronic structure of the 2DES. Notably, it produces a subband structure and determines the orbital order of the different subbands. X-ray spectroscopy has revealed that the Ti $3d$-t_{2g} bands, which are three-fold degenerate in a cubic crystal (see Figs. 1.4a and 1.4b), exhibit an energy splitting due to the confinement in the direction perpendicular to the interface [37]. As depicted in Fig. 1.4c, the formation of an interface lowers the energy of the states with d_{xy} symmetry with respect to the states with d_{xz}/d_{yz}; the former predominantly reside in TiO_2 planes close to the interface while the latter extend further in the direction perpendicular to the interface [27, 38].

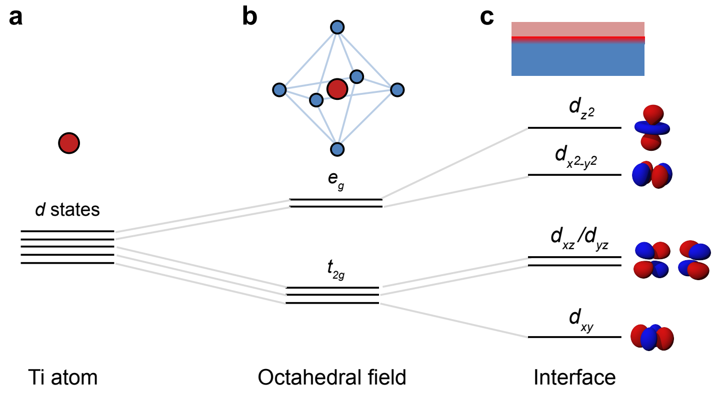

Figure 1.4: Energy levels of the Ti $3d$ orbitals. (a) Isolated Ti atom. (b) Octahedral field from a cubic perovskite. (c) Interface: non inversion-symmetric tetragonal environment.

This has important consequences for electronic transport. Magnetotransport measurements as a function of electrostatic doping have shown that, at low carrier densitities, the Hall voltages are linear in magnetic field, indicating that transport follows a single-band behavior. Above a critical density, Hall curves become non-linear, which is consistent with two-band transport. This transition has been firmly established, as it has been observed by several groups [39–43]. However, it is important to mention that different works report different values for the corresponding critical carrier density, indicating that it might depend on factors other than the band structure alone.

This critical density corresponds to a Lifshitz transition between the population of a single, light, d_{xy} band and the additional population of two heavy bands: the d_{xz} and the d_{yz} (see Fig. 1.5a). The reason for the difference in their mobilities can be understood from a simple geometrical argument: in contrast with yz and xz bands, both lobes of the xy are in plane, resulting in a larger orbital overlap. Gate-dependent angle-resolved photoemission spectroscopy measurements have corroborated this scenario [44]. Band structure calculations [45, 46] show that atomic spin–orbit interactions lift the degeneracy between d_{xz}/d_{yz} bands and give rise to an energy gap Δ_{so}, causing avoided band crossings and mixing the band characters. As a result, a more accurate band structure is depicted in Fig. 1.5b.

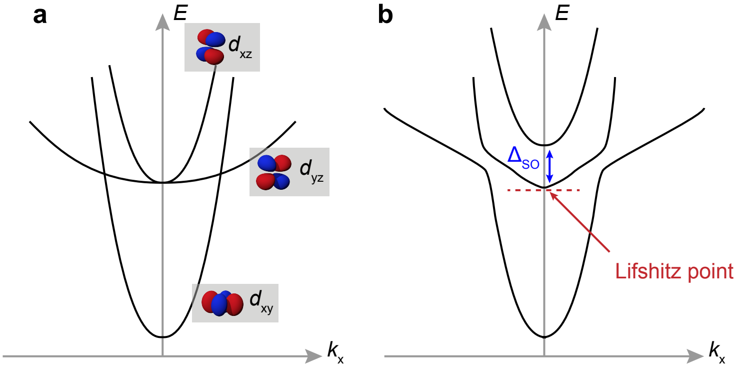

Figure 1.5: Band structure of the 2DES hosted at the LAO/STO interface (a) without and (b) with spin–orbit interactions. At the Γ-point the bands are split by Δ_{SO}.

This simple yet effective band picture has been linked to important experimental observations.

I. Rashba spin–orbit interactions

Rashba spin–orbit coupling can also be dramatically tuned by the gate voltage at LAO/STO interfaces [47, 48]. The spin–orbit strength is found to sharply rise as the carrier density is increased and reaches very large values of the order of 10 meV [47]. The doping range over which the spin-orbit interaction exhibits this steep increase appears to correlate with the aforementioned Lifshitz transition. Atomic spin–orbit interactions should be most prominent where the bands are degenerate, which corresponds exactly to the energy where the heavy bands start being populated — the Lifshitz transition. In turn, the influence of Rashba spin–orbit coupling is also peaked at the Lifshitz point, because it is directly proportional to the atomic spin–orbit coupling.

II. Superconductivity

While the dome-shaped phase diagram of superconductivity at LAO/STO interfaces is well-established, the influence of the Lifshitz transition on superconductivity is still under debate. Experimentally, it has been found that the peak of the superconducting dome occurs in the vicinity of the Lifshitz transition [39, 49]. On the one hand, at higher doping T_c decreases, hinting that the demise of superconductivity is linked to the filling of the d_{xz}/d_{yz} states. On the other hand, at low carrier densities the system is not superconducting, supporting the argument that the superconducting regime cannot be driven by purely d_{xy} states.

An interesting aspect to consider is the possible influence of spin–orbit on the superconducting state. The increase of strength of spin–orbit interactions is concomitant with the onset of superconductivity and reaches values much larger than the superconducting gap (40 μeV [50]). This might lead to a non s-wave symmetry of the order parameter. Future experiments sensitive to the symmetry of the order parameter will allow for a better understanding of the interplay between spin–orbit coupling and superconductivity.

1.4. THIS THESIS

In this thesis, we investigate quantum transport phenomena at oxide interfaces, with particular focus on phenomena at the LAO/STO interface.

In Chapter 2 we demonstrate that spin–orbit coupling and scattering from finite-range impurities can explain the giant in-plane magnetoresistance observed at the LAO/STO interface. The thermal insensitivity of the giant magnetoresistance, in combination with a striking correspondence that we have observed between the gate voltage and temperature dependence of the effect, are features that are difficult to reconcile with the thermally fragile Kondo interpretation — but fit naturally in the semiclassical Boltzmann description.

In Chapter 3, we explore a side gate geometry in order to realize gate-tunable Josephson junctions at the LAO/STO interface. We demonstrate local electrostatic tunability of these junctions while preserving a single lithographic step process by simultaneously defining both the constrictions and the side gate electrodes. We address the high dielectric constant of STO, demonstrating that it renders the action of the side gates comparable to that of an effective "local back gate".

Chapters 4 and 5 are dedicated to the study of LAO/STO interfaces along the (111) crystallographic direction. In Chapter 4 we report the discovery of 2D superconductivity at the (111)LAO/STO interface. The superconducting transition is consistent with a Berezinskii–Kosterlitz–Thouless transition and its 2D nature is further corroborated by the anisotropy of the critical magnetic field. In Chapter 5 we show that along this direction transport occurs through two sets of electron-like sub-bands, and the carrier density of one of the sets shows a non-monotonic dependence on the sample conductance. Using tight-binding modelling, we demonstrate that this behavior stems from a band inversion driven by on- site Coulomb interactions.

In Chapter 6 we investigate the properties of free-standing single-crystal $SrRuO_3$ (SRO). Free-standing ultrathin films are obtained by etching of a water-soluble buffer layer and exhibit ferromagnetic behavior down to at least 3 nm thickness. Magnetotransport measurements show that the anomalous Hall conductivity is modified with respect to epitaxial SRO films grown on STO. We show that the data can be well described by a phenomenological model comprising two channels with opposite signs of their anomalous Hall conductivity.

2

GIANT MAGNETORESISTANCE DRIVEN BY SPIN–ORBIT COUPLING AT THE $LaAlO_3/SrTiO_3$ INTERFACE

The $LaAlO_3/SrTiO_3$ interface hosts a two-dimensional electron system that is unusually sensitive to the application of an in-plane magnetic field. Low-temperature experiments have revealed a giant negative magnetoresistance (dropping by 70%), attributed to a magnetic field induced transition between interacting phases of conduction electrons with Kondo-screened magnetic impurities. Here we report on experiments over a broad temperature range, showing the persistence of the magnetoresistance up to the 20 K *range — indicative of a single-particle mechanism. Motivated by a striking correspondence between the temperature and carrier density dependence of our magnetoresistance measurements we propose an alternative explanation. Working in the framework of semiclassical Boltzmann transport theory we demonstrate that the combination of spin–orbit coupling and scattering from finite-range impurities can explain the observed magnitude of the negative magnetoresistance, as well as the temperature and electron density dependence.*

Parts of this chapter have been published in Physical Review Letters **115**, 016803 [42].
Theoretical modelling using the semi-classical Boltzmann transport equation was performed by M. Diez, E. Cobanera, T. Hyart, N. Bovenzi and C. W. J. Beenakker.

THE mobile electrons at the $LaAlO_3/SrTiO_3$ (LAO/STO) interface [16] display an exotic combination of superconductivity [15, 36] and magnetic order [51–54]. The onset of superconductivity at sub-Kelvin temperatures appears in an interval of electron densities where the effect of Rashba spin–orbit coupling on the band structure at the Fermi level is strongest [47, 48], but whether this correlation implies causation remains unclear.

Transport experiments above the superconducting transition temperature have revealed a very large ("giant") drop in the sheet resistance of the LAO/STO interface upon application of a parallel magnetic field [39, 55–57]. An explanation has been proposed [57, 58] in terms of the Kondo effect: Variation of the electron density or magnetic field drives a quantum phase transition between a high-resistance correlated electronic phase with screened magnetic impurities and a low-resistance phase of polarized impurity moments. The relevance of spin–orbit coupling for magnetotransport is widely appreciated [55, 58–63], but it was generally believed to be too weak an effect to provide a single-particle explanation of the giant magnetoresistance.

In this chapter we provide experimental data (combining magnetic field, gate voltage, and temperature profiles for the resistance of the LAO/STO interface) and theoretical calculations that support an explanation fully within the single-particle context of Boltzmann transport. The key ingredients are the combination of spin–orbit coupling, band anisotropy, and finite-range electrostatic impurity scattering. The thermal insensitivity of the giant magnetoresistance [55, 56], in combination with a striking correspondence that we have observed between the gate voltage and temperature dependence of the effect, are features that are difficult to reconcile with the thermally fragile Kondo interpretation — but fit naturally in the semiclassical Boltzmann description.

2.1. GIANT NEGATIVE MAGNETORESISTANCE

Devices were fabricated by using amorphous LAO (α-LAO) as a hard mask and epitaxially depositing a thin (12 u. c.) film of LAO on top of a TiO_2-terminated (0 0 1)STO single crystal substrate. The film was grown by pulsed laser deposition at 770 °C in O_2 at a pressure of $6 \cdot 10^{-5}$ mbar. The laser fluence was 1 J cm^{-2} and the repetition rate was 1 Hz. The growth of the film was monitored *in-situ* using reflection high energy electron diffraction (RHEED), and layer-by-layer growth was confirmed. After deposition, the sample was annealed for one hour at 600 °C in 300 mbar of O_2. Finally, the sample was cooled down to room temperature in the same atmosphere. Magnetotransport measurements were performed in a four-probe Hall bar geometry and in a field-effect configuration (Fig. 2.1a, inset) established with a homogeneous metallic back gate. The magnetic field B is applied in-plane and perpendicular to the current. The longitudinal sheet resistance $\rho_{xx}(B)$ determines the dimensionless magnetoresistance

$$\mathrm{MR}(B) = \rho_{xx}(B)/\rho_{xx}(0) - 1. \tag{2.1}$$

The left panel of Fig. 2.1a shows the measured magnetoresistance as a function of magnetic field, recorded at 1.4 K, for gate voltages V_G ranging from 0 V to 50 V. In general, we observe the magnetoresistance to remain mainly flat up to some characteristic value of the magnetic field. For larger values, the magnetoresistance drops sharply.

At even higher magnetic fields, the magnetoresistance begins to saturate, producing an overall bell-like curve. At the highest voltage $V_\mathrm{G} = 50\,\mathrm{V}$, a very large negative magnetoresistance is observed (a drop of 70%) over a magnetic field range from 0T to 12T. As V_G is decreased, the overall magnitude of the magnetoresistance drop is suppressed, as the curves flatten out and the characteristic field progressively moves to higher B. At $V_\mathrm{G} = 10\,\mathrm{V}$, the maximum magnetoresistance variation is less than 5%.

The right panel of Fig. 2.1a shows the measured magnetoresistance at a fixed gate voltage of $\mathrm{V_G} = 50\,\mathrm{V}$, for different temperatures ranging from 1.4K to 20K. The correspondence between the bell-shaped magnetoresistance profiles as a function of temperature and gate voltage is striking. As T increases or V_G decreases, both the magnitude of the magnetoresistance and steepness of $\partial\mathrm{MR}/\partial\mathrm{B}$ decrease. Although the negative magnetoresistance is progressively suppressed as the temperature is raised, it is still clearly visible at 20K, in agreement with previous experiments [55, 56]. Notice that the characteristic field scale of the resistance drop increases with temperature.

2.2. THREE-BAND MODEL

For the theoretical description we use a three-band model of the $t_{2\mathrm{g}}$ conduction electrons at the LAO/STO interface [39], with Hamiltonian

$$H = \sum_{\boldsymbol{k},l,l',\sigma,\sigma'} c^\dagger_{\boldsymbol{k},l,\sigma}\,(H_\mathrm{L} + H_\mathrm{SO} + H_\mathrm{Z} + H_\mathrm{B})\,c_{\boldsymbol{k},l',\sigma'}. \tag{2.2}$$

The operators $c^\dagger_{\boldsymbol{k},l,\sigma}$ create electrons of spin σ and momentum $\boldsymbol{k}$ (measured in units of the lattice constant $a = 0.4\,\mathrm{nm}$), in orbitals $l = d_{xy}, d_{xz}, d_{yz}$ of the Ti atoms close to the interface. We describe the various terms in this three-band Hamiltonian, with parameter values from the literature [39, 44, 46, 64–69] that we will use in our calculations.

The lobes of the d_{xy} orbital are in-plane, producing two equivalent hopping integrals $t_l = 340\,\mathrm{meV}$. For the two other orbitals, the x-lobe or y-lobe is in-plane and the z-lobe is out-of-plane, giving rise to one large and one small hopping element t_l and $t_h = 12.5\,\mathrm{meV}$, respectively. The d_{xz} and d_{yz} orbitals are hybridized by a non-diagonal hopping $t_d = t_h$. Confinement lowers the d_{xy} orbital in energy by $\Delta_E = 60\,\mathrm{meV}$. All this information is encoded in

$$H_\mathrm{L} = \begin{pmatrix} \epsilon_{xy}(k) - \Delta_\mathrm{E} & 0 & 0 \\ 0 & \epsilon_{xz}(k) & \delta(k) \\ 0 & \delta(k) & \epsilon_{yz}(k) \end{pmatrix} \otimes \hat{\sigma}_0, \tag{2.3}$$

$$\begin{aligned} \epsilon_{xy}(k) &= 2t_l(2 - \cos k_x - \cos k_y), \\ \epsilon_{xz}(k) &= 2t_l(1 - \cos k_x) + 2t_h(1 - \cos k_y), \\ \epsilon_{yz}(k) &= 2t_h(1 - \cos k_x) + 2t_l(1 - \cos k_y), \\ \delta(k) &= 2t_d \sin k_x \sin k_y. \end{aligned} \tag{2.4}$$

We use $\hat{\sigma}_{x,y,z}$ and $\hat{\sigma}_0$ to denote the Pauli-matrices and the identity acting on the electron spin. The intrinsic electric field at the interface breaks inversion symmetry and produces

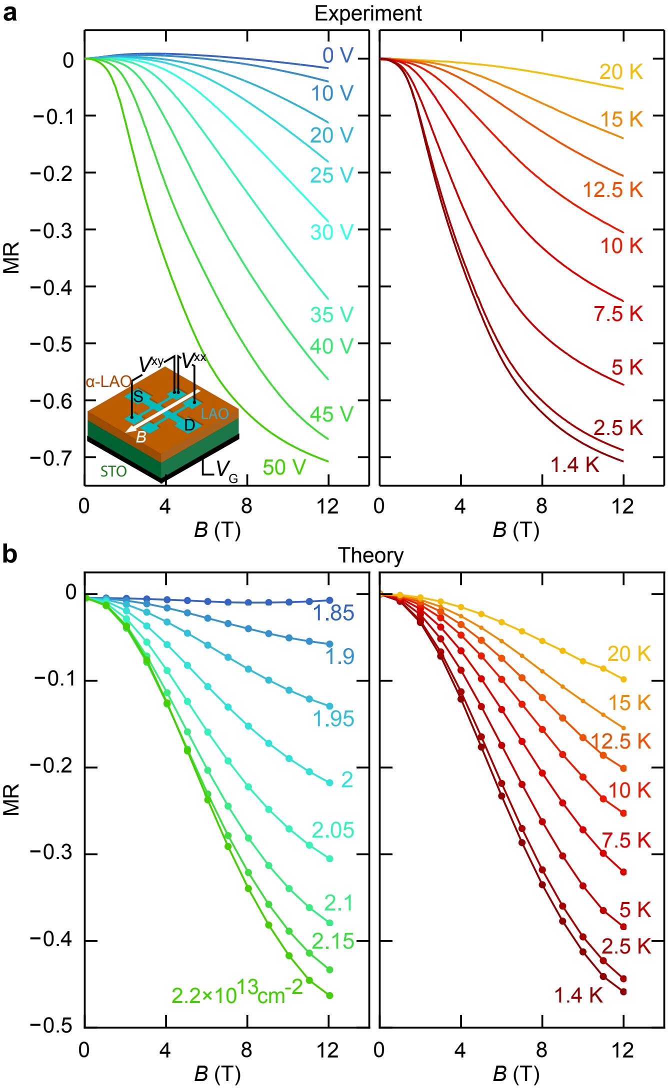

Figure 2.1: (a) Measured magnetoresistance at $T = 1.4\,\mathrm{K}$ for different gate voltages (left panel) and at $V_G = 50\,\mathrm{V}$ for various temperatures (right panel). Inset: Schematic drawing of the device in a Hall bar geometry (in-plane field perpendicular to current direction), showing the source S, drain D, longitudinal voltage V^{xx}, transverse voltage V^{xy} and gate voltage V_G. (b) Magnetoresistance calculated from the Boltzmann equation, at fixed $T = 1.4\,\mathrm{K}$ (left panel) and at fixed $n = 2.2 \cdot 10^{13}\,\mathrm{cm}^{-2}$ (right panel).

the term

$$H_Z = \Delta_Z \begin{pmatrix} 0 & i\sin k_y & i\sin k_x \\ -i\sin k_y & 0 & 0 \\ -i\sin k_x & 0 & 0 \end{pmatrix} \otimes \hat{\sigma}_0, \tag{2.5}$$

with $\Delta_Z = 15\,\text{meV}$. Atomic spin–orbit coupling gives

$$H_{SO} = \frac{\Delta_{SO}}{2} \begin{pmatrix} 0 & i\hat{\sigma}_x & -i\hat{\sigma}_y \\ -i\hat{\sigma}_x & 0 & i\hat{\sigma}_z \\ i\hat{\sigma}_y & -i\hat{\sigma}_z & 0 \end{pmatrix}, \tag{2.6}$$

with an amplitude $\Delta_{SO} = 5\,\text{meV}$. Together, H_Z and H_{SO} cause a Rashba-type splitting of the bands, coupling the d_{xy} orbital with the $d_{xz/yz}$ orbitals above the Lifshitz point at the bottom of the $d_{xz/yz}$ bands.

The term $H_B = \mu_B(\boldsymbol{L} + g\boldsymbol{S}) \cdot \boldsymbol{B}/\hbar$, with $g = 5$ [69], describes the coupling of the applied magnetic field to the spin and orbital angular momentum of the electrons, where $\boldsymbol{S} = \hbar\hat{\boldsymbol{\sigma}}/2$ and

$$L_x = \hbar \begin{pmatrix} 0 & i & 0 \\ -i & 0 & 0 \\ 0 & 0 & 0 \end{pmatrix}, L_y = \hbar \begin{pmatrix} 0 & 0 & -i \\ 0 & 0 & 0 \\ i & 0 & 0 \end{pmatrix}, L_z = \hbar \begin{pmatrix} 0 & 0 & 0 \\ 0 & 0 & i \\ 0 & -i & 0 \end{pmatrix}. \tag{2.7}$$

The resulting highly anisotropic band structure is shown in Fig. 2.2. Notice the unusually close relevant energy scales: When measured from the bottom of the upper, anisotropic bands, the Fermi energy, spin–orbit coupling induced spin-splitting, Zeeman energy (10 T) and temperature (10 K) all are on the order of 1 meV.

2.3. BOLTZMANN TRANSPORT

We calculate the magnetoresistance from the model Hamiltonian (2.2) using the semiclassical Boltzmann transport equation for the momentum $\boldsymbol{k}$ and band index ν-dependent distribution function $f_{\boldsymbol{k},\nu} = f_0(\epsilon_{\boldsymbol{k},\nu}) + g_{\boldsymbol{k},\nu}$. We linearize around the equilibrium Fermi–Dirac distribution f_0, at temperature T and chemical potential μ (determined self-consistently to obtain a prescribed carrier density n). In this way we find the conductivity tensor

$$\sigma_{ij} = e \sum_{\boldsymbol{k},\nu} (\boldsymbol{v}_{\boldsymbol{k},\nu})_i \partial g_{\boldsymbol{k},\nu} / \partial E_j \tag{2.8}$$

in linear response to the electric field $\boldsymbol{E}$.

The longitudinal resistivity ρ_{xx} then follows upon inversion of the $\boldsymbol{\sigma}$-tensor. The band structure determines the velocity $\boldsymbol{v}_{\boldsymbol{k},\nu} = \hbar^{-1}\nabla_{\boldsymbol{k}}\epsilon_{\boldsymbol{k},\nu}$, which is not parallel to the momentum $\hbar\boldsymbol{k}$ because of the anisotropic Fermi surface.

Calculations of this type are routinely simplified using Ziman's relaxation-time approximation [70, 71], but the combination of finite-range scattering and anisotropic band structure renders this approximation unreliable [72]. We have therefore resorted to a numerical solution of the full partial differential equation:

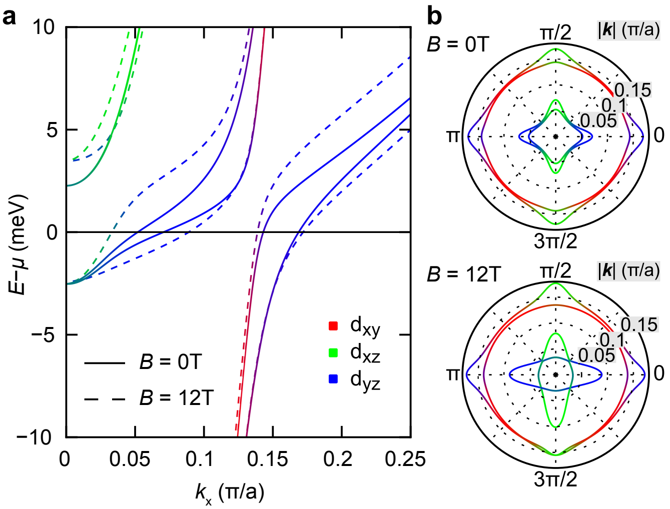

Figure 2.2: (a) Dispersion relation for the mobile electrons at the $LaAlO_3/SrTiO_3$ interface, calculated from the model Hamiltonian (2.2) for $n = 2.2\cdot 10^{13}\,\mathrm{cm}^{-2}$ at $B = 0\,\mathrm{T}$ (solid line) and $B = 12\,\mathrm{T}$ (dashed line). Colors indicate the orbital character of the bands. (b) Corresponding Fermi surfaces when the chemical potential is located at the "sweet spot" above the Lifshitz point where the system becomes very sensitive to changes in carrier density and magnetic field.

$$
\begin{aligned}
-e(\boldsymbol{v}_{\boldsymbol{k},\nu}\cdot\boldsymbol{E})\partial f_0/\partial\epsilon_{\boldsymbol{k},\nu} &= (e/\hbar)(\boldsymbol{v}_{\boldsymbol{k},\nu}\times\boldsymbol{B})\cdot\nabla_{\boldsymbol{k}}g_{\boldsymbol{k},\nu}\\
&+\sum_{\boldsymbol{k}',\nu'}(g_{\boldsymbol{k},\nu}-g_{\boldsymbol{k}',\nu'})q_{\boldsymbol{k}\nu,\boldsymbol{k}'\nu'}\delta(\epsilon_{\boldsymbol{k},\nu}-\epsilon_{\boldsymbol{k}',\nu'}).
\end{aligned}
\tag{2.9}
$$

Elastic impurity scattering enters with a rate

$$
q_{\boldsymbol{k}\nu,\boldsymbol{k}'\nu'} = \tfrac{2}{3}\pi^3\hbar^{-1}\delta^2 xi^4 n_{\mathrm{imp}}\, e^{-\xi^2|\boldsymbol{k}-\boldsymbol{k}'|^2/2}|\langle u_{\boldsymbol{k}\nu}|u_{\boldsymbol{k}'\nu'}\rangle|^2. \tag{2.10}
$$

The impurity density n_{imp} and scattering amplitude δ drop out of the magnetoresistance (2.1), so they need not be specified. The scattering potential has correlation length ξ, for which we take $2\,\mathrm{nm} \simeq 5$ lattice constants, consistent with experiments on scattering by dislocations [73]. (We will discuss the role of this finite correlation length later on.) Both intraband and interband scattering are included via the structure factor $|\langle u_{\boldsymbol{k}\nu}|u_{\boldsymbol{k}'\nu'}\rangle|^2$, which takes into account the finite overlap $\langle\psi_\nu(\boldsymbol{k})|V(\boldsymbol{r})|\psi_{\nu'}(\boldsymbol{k}')\rangle$ of the Bloch states $\psi_\nu(\boldsymbol{k}) = u_{\boldsymbol{k}\nu}(\boldsymbol{r})e^{i\boldsymbol{k}\cdot\boldsymbol{r}}$ and $\psi_{\nu'}(\boldsymbol{k}') = u_{\boldsymbol{k}'\nu'}(\boldsymbol{r})e^{i\boldsymbol{k}'\cdot\boldsymbol{r}}$.

The magnetoresistance resulting from the Boltzmann equation is shown in Fig. 2.1b. The similarity in the bell-shaped magnetoresistance curves, with a corresponding dependence on carrier density and temperature, is clear and remarkable in view of the simplicity of the theoretical model. We conclude that a semiclassical single-particle description can produce a "giant" magnetoresistance, up to 50% for a quite conservative choice of parameter values. Two main ingredients explain how such a large negative magnetoresistance could follow from a model without electron-electron interac-

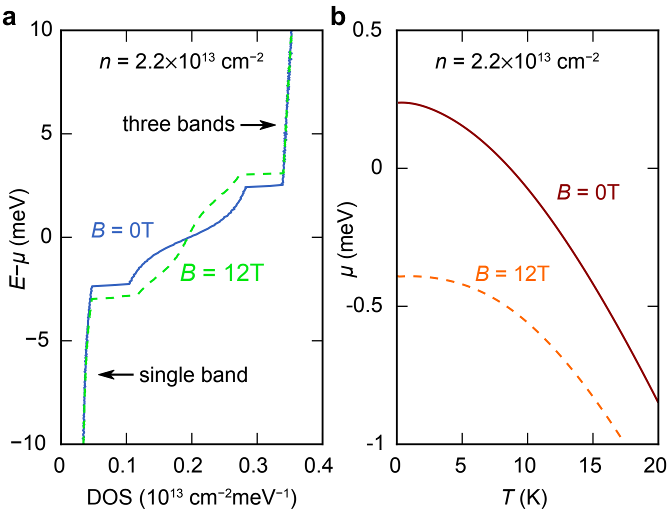

Figure 2.3: (a) Energy-dependent density of states. (b) Temperature-dependent chemical potential. Both quantities are calculated from the three band Hamiltonian (2.2) and shown for the “sweet-spot” carrier density $n = 2.2 \cdot 10^{13}\,\mathrm{cm}^{-2}$, at $B = 0\,\mathrm{T}$ (solid line) and $B = 12\,\mathrm{T}$ (dashed line).

tions. The *first ingredient* is the orbital-mixing character of the atomic and inversion-symmetry-breaking spin–orbit coupling terms H_{SO} and H_{Z}. As a result, the spin–orbit splitting is very non-linear and produces a “sweet spot”, that is, a narrow range of Fermi energies (carrier densities $n^* \simeq 2.2 \cdot 10^{13}/\mathrm{cm}^2$) in which the system becomes sensitive to small changes in the density. If the density (or the corresponding gate voltage) is near the sweet spot, the spin–orbit induced band mixing gives rise to a substantial contribution to the (zero-field) resistance stemming from inter-band scattering. The Zeeman energy in turn favors an alignment of the spin with the magnetic field and drives a highly anisotropic deformation of the Fermi surface into spin-polarized bands (see Fig. 2.2). Inter-band scattering is suppressed which explains the decrease in sheet-resistance. At densities $n < n^*$ only a single band is occupied and spin–orbit coupling is well described by a conventional Rashba term $\alpha_{\mathrm{SO}}(\hat{\boldsymbol{\sigma}} \times \boldsymbol{p})$ [47, 66, 74] and our calculation gives a vanishingly small magnetoresistance. At densities $n > n^*$ the calculated magnetoresistance starts to saturate and eventually becomes small again.

The *second ingredient* is the finite correlation length ξ of the disorder potential. The resulting anisotropic scattering rate (2.10) is largest at small momenta $|\boldsymbol{k} - \boldsymbol{k}'|$. Moderate values of ξ on the order of a few lattice constants suppress back-scattering processes within the outer Fermi surface with large average momentum k_{F}, while still allowing for inter-band scattering. This is accompanied by a quasi-particle lifetime which can be significantly smaller for the inner band (smaller average k_{F}). The imbalance of band mobilities promotes the importance of inter-band scattering when transport is dominated by quasi-particles in the outer bands which have a larger Fermi velocity and a small intra-band back-scattering rate. In comparison we have found that the isotropic scattering by a delta-function impurity potential cannot produce an MR exceeding 15%.

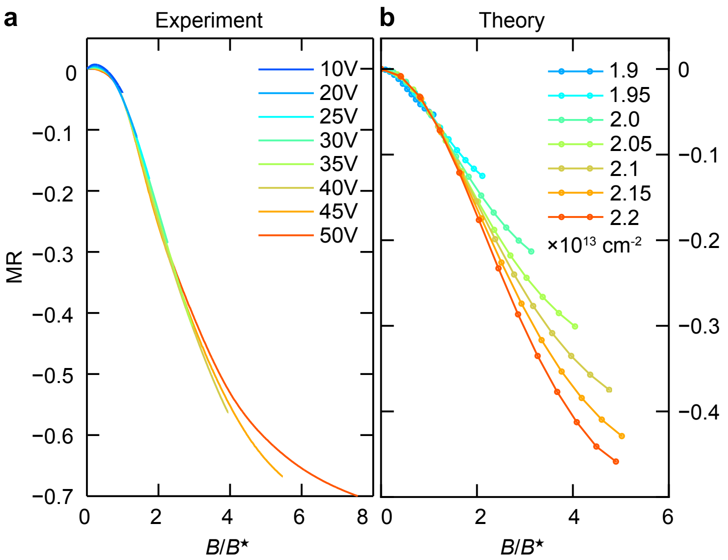

Figure 2.4: (a) Measured and (b) calculated magnetoresistance at 1.4 K for different densities or gate voltages as a function of the rescaled magnetic field $B/B^\star$. The characteristic field $B^\star$ is chosen such that the rescaled curves all pass through the point with MR = −0.05.

Our theoretical curves show a smooth dependence on temperature, with the negative magnetoresistance persisting beyond 20 K, and they show a striking correspondence between the temperature dependence of the magnetoresistance for a fixed density and the density dependence for a fixed temperature. This correspondence, a hallmark of our experimental data, can be understood as a consequence of the renormalization of the chemical potential as a function of temperature, see Fig. 2.3b. The weak temperature dependence of the Hall resistance in separate measurements point towards a constant carrier density in the range 1–20 K. As shown in Fig. 2.3a the density of states increases steeply with band energy in the vicinity of the sweet spot, much more than in typical semiconductors.

To keep the total carrier density fixed with increasing temperature, the chemical potential is lowered by more than 1 meV at 20 K compared to its low temperature limit. This is why increasing the temperature is equivalent to probing the band structure at a lower energy, explaining the similarity in the magnetoresistance curves in the left and right panels of Fig. 2.1.

These are the two key arguments in favor of a single-particle spin–orbit coupling based mechanism for the giant negative magnetoresistance: Firstly, the persistence of the effect to elevated temperatures, and secondly the corresponding effect of temperature increase and density decrease. It seems difficult to incorporate these features of the data in the correlated-electron mechanism [57, 58], based on Kondo-screening of magnetic moments. There is a third noteworthy feature of the data that is not well reproduced by our calculation, and has been interpreted as evidence for a transition into a low-field Kondo phase [57, 58]: A rescaling of the magnetic field $B \to B/B^{\star}$ by a density-dependent value $B^{\star}$ collapses the measured magnetoresistance at different densities onto a single curve, see Fig. 2.4a. If we apply this $B/B^{\star}$ scaling to our numerical results a significant n-dependence remains, see Fig. 2.4b. The experimental scaling law points to some relevant physics that is not yet included in our minimal model.

In fact, while the two mechanisms have an altogether different origin, it may well be that the spin–orbit coupling mechanism is assisted by magnetic moments in the vicinity of the interface. Even in the case of only weak exchange interactions between mobile carriers and localized moments, a field driven magnetization of the moments may increase the microscopic field beyond the externally applied one, thereby enhancing the negative magnetoresistance.

2.4. CONCLUSION

In conclusion, we have presented experimental data and theoretical calculations that support a semiclassical single-particle mechanism for the giant magnetoresistance of the LAO/STO interface. The Boltzman transport equation with spin–orbit coupling, in combination with anisotropy of Fermi surface and scattering rates, suffices to produce a large resistance drop upon application of a magnetic field. The characteristic temperature and carrier-density dependence agree quite well with what is observed experimentally, but the $B/B^{\star}$ scaling will likely require an extension of the simplest three-band model.

Our explanation of the sudden onset of the magnetoresistance when the carrier density approaches a “sweet spot” of amplified spin–orbit coupling has addressed the normal-state transport above the superconducting transition temperature. Since superconductivity happens in the vicinity of the same “sweet spot”, it would be interesting to investigate whether spin–orbit coupling plays a dominant role in that transition as well.

3

TUNABLE JOSEPHSON JUNCTIONS AND QUANTUM INTERFERENCE AT THE $LaAlO_3/SrTiO_3$ INTERFACE

Novel physical phenomena arising at the interface of complex oxide heterostructures offer exciting opportunities for the development of future electronic devices. Using the prototypical $LaAlO_3/SrTiO_3$ *interface as a model system, we employ a single-step lithographic process to realize gate tunable Josephson junctions through a combination of lateral confinement and local side gating. The action of the side gates is found to be comparable to that of a local back gate, constituting a robust and efficient way to control the properties of the interface at the nanoscale. We demonstrate that the side gates enable reliable tuning of both the normal-state resistance and the critical (Josephson) current of the constrictions. The conductance and Josephson current show mesoscopic fluctuations as a function of the applied side gate voltage, and the analysis of their amplitude enables the extraction of the phase coherence and thermal lengths. Finally, we realize a superconducting quantum interference device in which the critical currents of each of the constriction-type Josephson junctions can be controlled independently via the side gates.*

Parts of this chapter have been published in Nano Letters **17**, 715-720 [75].
Finite element simulations were performed by N. Manca.

Complex oxide heterostructures host a diverse set of novel physical phenomena which, in combination with an ever-advancing degree of experimental control, shows their promise for fundamental discovery and technological applications [14, 76]. Over the past decade, the creation and control of interface superconductivity in oxide heterostructures has attracted a great deal of attention, with special emphasis on the two-dimensional electron system (2DES) hosted at the interface between the two wide band-gap insulators $LaAlO_3$ (LAO) and $SrTiO_3$ (STO) [16, 36]. Superconductivity at the LAO/STO interface occurs in an exotic environment with strong spin–orbit coupling [42, 47, 48] in coexistence with localized magnetic moments[52, 53] and ferroelastic domains [77, 78]. Moreover, the superfluid density can be tuned using the electrostatic field-effect [79], allowing for an on-off switch of superconductivity by means of an externally applied gate voltage [15, 80]. Despite substantial experimental efforts [50, 79, 81] accompanied by a growing body of theoretical works [82–84], the microscopic details of superconductivity in the system are still not completely understood. Efforts to clarify this question have propelled the realization of devices to perform phase-sensitive measurements, opening the possibility to garner information about the symmetry of the superconducting order parameter of the system [50, 79]. Josephson coupling has recently been reported in STO-based 2DESs, first in top-gated structures where the weak link is electrostatically defined [85–87], and later in constriction-type Josephson junctions (c-JJ) [88]. Quantum interference was observed through the integration of two such weak links in a superconducting loop, forming a superconducting quantum interference device (SQUID) [88]. While the top-gating approach benefits from the ability to independently tune each of the weak links, it is rather complex due to the requirement of multiple aligned lithography steps. Moreover, it is well established that the properties of the 2DES at the LAO/STO interface are extremely sensitive to metals and chemicals adsorption [89–91] at the surface. These problems can be overcome by employing the simpler c-JJ approach, which requires only a single lithographic step and no further processing after the LAO growth. However, it remains to be shown whether local tunability can be achieved in such weak links.

In this chapter, we explore a side gate geometry in order to realize gate-tunable c-JJs at the LAO/STO interface. We demonstrate local electrostatic tunability of these c-JJs while preserving a single lithographic step process by simultaneously defining both the constrictions and the side gate electrodes. Similar approaches are often employed in conventional semiconductor based 2DESs to obtain lateral confinement and electrostatically control the effective channel width [92]. Here, however, we find the electric field dependence of the STO permittivity to play a crucial role, rendering the action of the side gates comparable to that of an effective “local back gate”. For a single junction, phase-coherent transport gives rise to mesoscopic fluctuations of the conductance and of the (Josephson) critical current as a function of side gate voltage. The amplitude of these fluctuations enables us to extract the phase coherence and thermal lengths. Furthermore, we demonstrate the reliability of the side gate electrodes to locally and independently tune the weak links by integrating two side gated c-JJs in a SQUID and controlling the (a)symmetry of its response.

3.1. DEVICE FABRICATION

Device fabrication relies on a pre-patterning technique [93, 94] involving a single lithographic step, which makes use of a template to define the insulating regions on the STO substrate prior to the epitaxial growth of the LAO thin film. Starting from a TiO_2-terminated STO(001) substrate, we first pattern a resist mask using electron-beam lithography. After development, a thin (13 nm) AlO_x layer is deposited by sputtering and the remaining resist is removed by lift-off in acetone. As a result, the areas of the STO surface protected by the resist during AlO_x deposition are cleared, whereas the exposed regions are coated by AlO_x. Next, a 12 u.c. LAO film is deposited by pulsed laser deposition. In the areas where the STO surface is exposed, the LAO film grows crystalline (c-LAO) and the 2DES forms at the interface. The regions covered by AlO_x, where the LAO film grows amorphous (α-LAO), remain insulating. The growth process is monitored *in-situ* using reflection high energy electron diffraction (RHEED), displaying a layer-by-layer growth mode. The LAO films were grown at two different temperatures, namely 770° and 840°. Lower growth temperature results in samples with higher sheet resistance, whereas samples grown at higher temperature exhibit lower sheet resistance and superconductivity.

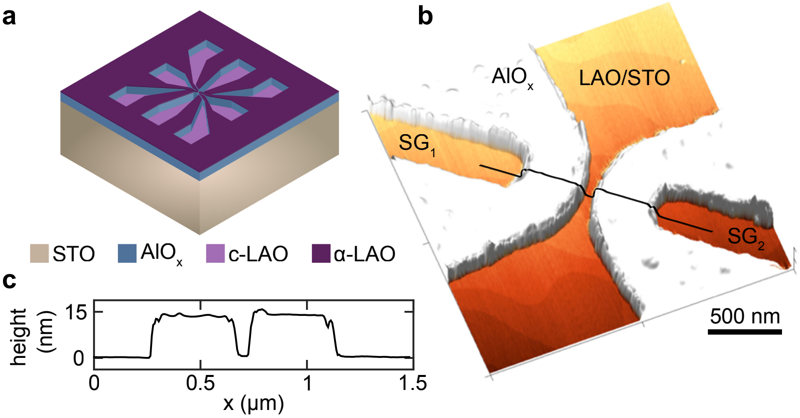

Figure 3.1: (a) 3D schematic of a side gated constriction. α-LAO: amorphous LAO; c-LAO: crystalline LAO. (b) AFM image of a typical device showing the constriction and two side gates (SG_1 and SG_2). The 2DES is formed only at the interface between c-LAO and STO. (c) Height profile along the black line in panel (b), showing a constriction width of approximately 50 nm.

A 3D schematic of a side gated constriction is shown in Fig. 3.1a. The AlO_x mask delimits the areas where the channel, the bonding pads, and the side gate electrodes are formed. An atomic force microscopy (AFM) image of a constriction and the two side gates is presented in Fig. 3.1b. The height profile in Fig. 3.1c reveals a channel width (w) of approximately 50 nm. We have fabricated different devices varying the distance between the side gates and the conducting channel, and the growth temperature of the LAO thin film. The parameters of the constriction devices presented in this work are summarized in Table 3.1 and all devices show qualitatively similar behavior.

	Dev1	Dev2	Dev3
w (nm)	50	50	50
L (nm)	500	500	500
d (nm)	200	100	100
T_{growth} (°C)	770	770	840

Table 3.1: Parameters of the side gate devices presented in this work: width (w) and length (L) of the conducting channel, distance between the channel and the side gates (d) and the growth temperature of the LAO thin film (T_{growth}).

3.2. FINITE ELEMENT SIMULATIONS

The measurement configuration used is shown in Fig. 3.2a. A constant DC current (I_{bias}) is injected through the conducting channel and the voltage drop (V) is locally measured at the constriction using two probes on the side. Voltages can be applied independently to the two side gates (V_{SG}^1 and V_{SG}^2), enabling local modulation of transport across the constriction by field-effect. In order to understand how the local side gates modulate transport through the constriction in this geometry, we performed Finite Element Analysis (FEA) in COMSOL®.Calculations are performed for the geometry sketched in Fig. 3.2b, using a channel width $w \approx 50\,\text{nm}$ and a distance $d \approx 100\,\text{nm}$ between the side gates and the channel. An important aspect that has to be addressed is the role of the strong electric field dependence of the permittivity of the STO substrate, which is not commonly found in other systems. Its electric field dependence is modeled as [95, 96]

$$\varepsilon_{\text{STO}}(E) = 1 + \frac{B}{[1+(E/E_0)^2]^{1/3}} \tag{3.1}$$

with $B = 23{,}500$ and $E_0 = 82{,}000\,\text{V/m}$ [97]. The side gate electrodes are modeled as areas of fixed voltage and the conducting channel as a ground plane. This approximation is valid provided the voltage drop across the constriction is negligible when compared to the magnitude of the voltages applied to the side gate electrodes.

Figure 3.2b shows a spatial map of the calculated out-of-plane electric polarization (P) in a symmetric gating configuration with $V_{\text{SG}}^{1,2} = -50\,\text{mV}$. The out-of-plane polarization is directly related to the accumulated charge carrier density at the interface by $\Delta n_{2\text{D}} = P/e$. Due to the coplanar capacitor arrangement, crowding of electric field lines occurs at the edges of the constriction. Figure 3.2c shows the resulting variation of P across the channel (white line in Fig. 3.2b) for different values of $V_{\text{SG}}^{1,2}$. For all the curves, the magnitude of P is maximum at the edges of the channel and minimum at its center. In turn, the enhancement of the local electric field intensity at the edges of the constriction results in a large decrease of the ε_{STO} as shown in Fig. 3.2d. This has two consequences that affect the electrostatic gating mechanism. Firstly, it leads to a progressive saturation of the depleted carrier density in the channel, reducing the gating efficiency as $V_{\text{SG}}^{1,2}$ increases in magnitude. Secondly, it redistributes the electric field lines towards the centre of the constriction, flattening out the depletion profile. The first effect is reported in Fig. 3.2e where the calculated polarization at the center of the channel ($P_{x=0\,\text{nm}}$) is plotted as a function of $V_{\text{SG}}^{1,2}$. The electric field dependence of ε_{STO} produces a deviation from the linear behavior one would obtain for ε_{STO} = constant, resulting in

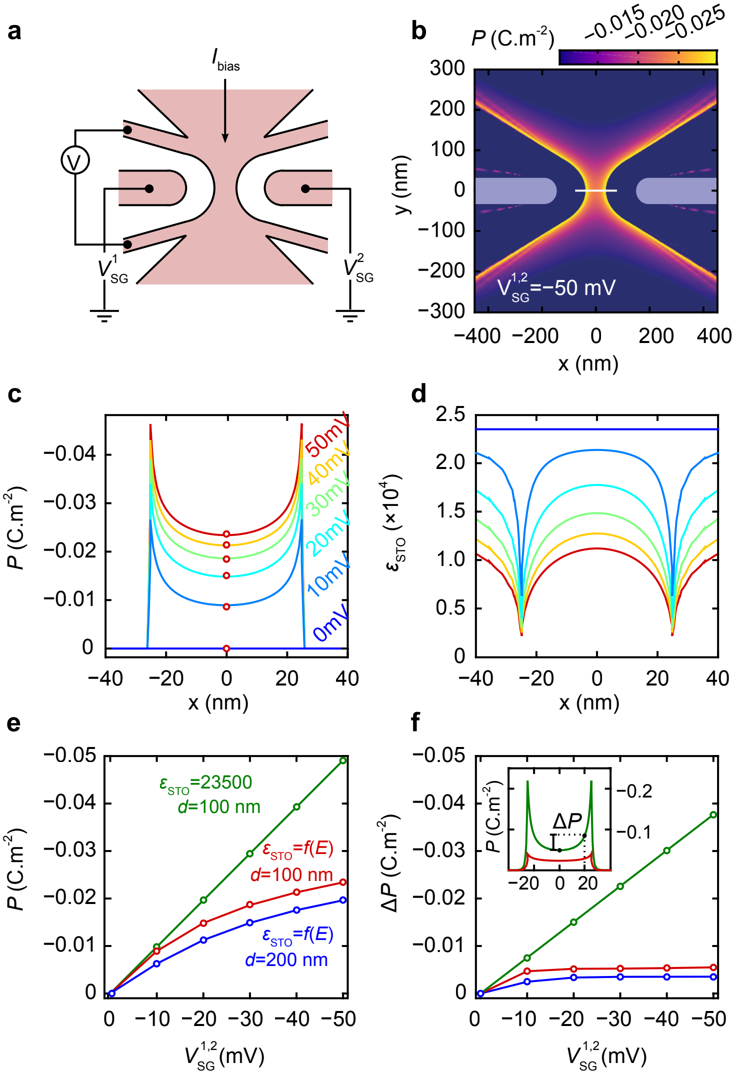

Figure 3.2: (a) Sketch of the device geometry showing the electrical connections for transport measurements. (b) Spatial map of the out-of-plane electric polarization (P) for $V^{1,2}_{\text{SG}} = -50\,\text{mV}$, obtained by finite-element simulations. (c) and (d) Evolution of P and ε_{STO}, respectively, across the constriction for different values of $V^{1,2}_{\text{SG}}$. (e) Value of P at the center of the constriction ($x = 0\,\text{nm}$) as a function of $V^{1,2}_{\text{SG}}$. (f) ΔP as a function of $V^{1,2}_{\text{SG}}$. Color code as in panel (e). Inset: electric polarization profiles across the constriction.

a reduction of the depleted charge. Moreover, within the same side gate voltage range, the magnitude of the induced polarization is smaller for the case $d = 200\,\text{nm}$ than for $d = 100\,\text{nm}$. This highlights the fact that the charge depletion is strongly dependent on the distance between the side gate electrodes and the channel. In Fig. 3.2f we show how the steepness of the polarization profile across the channel is affected by the field dependence of $\varepsilon_{\mathrm{STO}}$. To evaluate this effect we consider the variation of the polarization between $x = 0\,\mathrm{nm}$ and $x = 20\,\mathrm{nm}$, $\Delta P = P_{x=20\,\mathrm{nm}} - P_{x=0\,\mathrm{nm}}$. For the case $\varepsilon_{\mathrm{STO}} = \mathrm{constant}$, the magnitude of ΔP increases linearly with applied side gate voltage, representing a proportional scaling of the polarization profile. In contrast, for the case $\varepsilon_{\mathrm{STO}} = f(E)$, it rapidly saturates at $\sim 5\,\mu\mathrm{C/cm}^2$. This limits the extent to which side gating can reduce the effective width of the channel, since the depletion profile is less steep due to the dielectric response of the STO, as opposed to the stronger sideways depletion that would be obtained if $\varepsilon_{\mathrm{STO}} = \mathrm{constant}$ (red and green curves in the inset of Fig. 3.2f, respectively). This is in good agreement with previous reports on side gate electrodes at the LAO/STO interface, which show the electric field lines reaching the gas from below [97]. Therefore, the side gates are expected to act as an effective "local back gate" due to the proximity to the channel and can be used to locally modulate the carrier density at the nanoscale with the application of small voltages.

3.3. NORMAL STATE CHARACTERIZATION

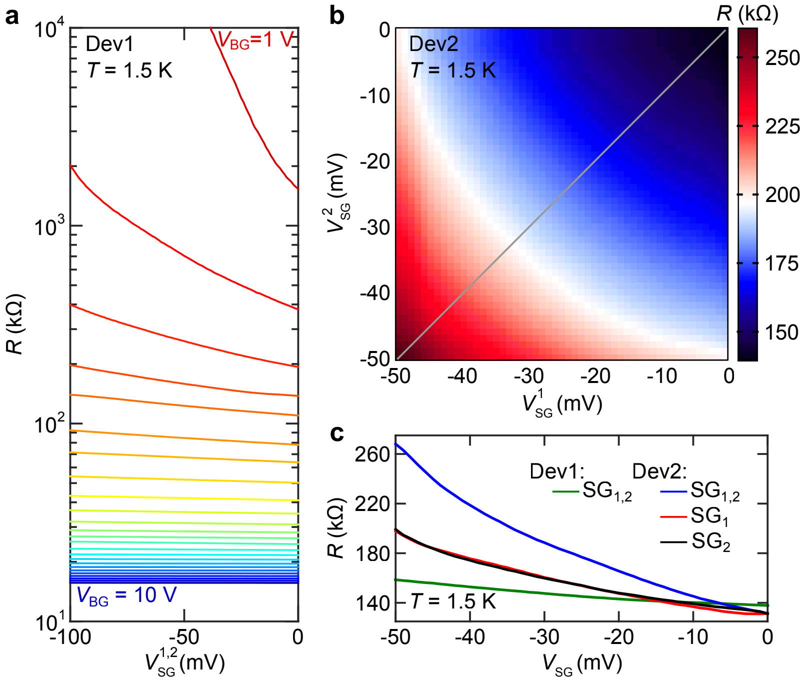

Figure 3.3: (a) 4-probe resistance (R) of as a function of side gate voltage $V_{\mathrm{SG}}^{1,2}$ measured for different V_{BG}. (b) Map of R as a function of V_{SG}^1 and V_{SG}^2. The voltage step is 0.2 mV. (c) R as a function of side gate voltage. Dev1: $V_{\mathrm{SG}}^1 = V_{\mathrm{SG}}^2$ (green). Dev2: $V_{\mathrm{SG}}^1 = V_{\mathrm{SG}}^2$ (blue), $V_{\mathrm{SG}}^2 = 0\,\mathrm{mV}$ (red) and $V_{\mathrm{SG}}^1 = 0\,\mathrm{mV}$ (black).

We first characterize the constrictions and the action of the two side gates through transport measurements in the normal state, at 1.5 K. Figure 3.3 shows electrical measurements of devices Dev1 and Dev2, where the side gates are separated from the constriction by 200 nm and 100 nm, respectively. In both devices, the overall carrier density can be tuned by the application of a back gate voltage (V_{BG}). The evolution of the 4-probe resistance (R) across the constriction in Dev1 as a function of $V_{\mathrm{SG}}^{1,2}$ for different V_{BG} is shown in Fig. 3.3a. At $V_{\mathrm{BG}} = 10\,\mathrm{V}$, R remains fairly unchanged within the side gate voltage range considered. This results from the fact that the change in carrier density $\Delta n_{2\mathrm{D}}$ induced by the side gates is a small fraction of the total carrier density accumulated by the back gate. As the back gate voltage is decreased, the effect of the side gates becomes increasingly appreciable and at $V_{\mathrm{BG}} = 1\,\mathrm{V}$, the side gates can completely deplete the channel.

Having established a range of V_{BG} in which the voltages applied to the side gates induce appreciable changes in the transport through the constriction, we now study the individual action of the side gates. Figure 3.3b shows a 2D map of the 4-probe resistance across the constriction of Dev2 as a function of V_{SG}^{1} and V_{SG}^{2}. The action of each side gate on the constriction is identical, evidenced by the symmetry across the diagonal (gray line). This is also reflected in the good overlap between the red and black curves in Fig. 3.3c, measured as SG_1 and SG_2 were individually driven from 0 to $-50\,\mathrm{mV}$, while keeping the other side gate at 0 mV. When both SG_1 and SG_2 are swept symmetrically, the resistance change is roughly twice as large (blue curve). This underlines the reliability of the patterning technique, where the action of the side gates is determined by the geometrical design. When comparing the induced change in resistance as a function of $V_{\mathrm{SG}}^{1,2}$ for Dev1 and Dev2, we observe it to be much smaller for Dev1, where the side gate electrodes are patterned further away from the constriction. This corroborates the expectation that the tunability of the resistance strongly depends on d, in good agreement with the simulations from Figs. 3.2e and 3.2f.

3.4. SUPERCONDUCTING STATE

We now turn our attention to the study of the superconducting regime. In previous work it was shown that such constrictions act as a weak link between the two superconducting reservoirs, forming a Josephson junction (c-JJ type) [88]. We first focus on the study and side gate modulation of transport through a single Josephson junction. In Fig. 3.4a, the differential resistance dV/dI is plotted in color scale as a function of bias current I_{bias} and side gates voltage $V_{\mathrm{SG}}^{1,2}$, i.e., in the symmetric side gating configuration. The measurement was performed at $T = 50\,\mathrm{mK}$ with a fixed back gate voltage $V_{\mathrm{BG}} = -11\,\mathrm{V}$. It can be seen that, on average, the supercurrent range (black region) is reduced when $V_{\mathrm{SG}}^{1,2}$ is driven to larger negative values, due to the consequent decrease of the electron carrier density. The corresponding values of critical current I_{c} as a function of $V_{\mathrm{SG}}^{1,2}$ are plotted in Fig. 3.4b. In the same graph, the differential conductance G is plotted in units of $2e^2/h$. I_{c} and G were determined from the differential resistance dV/dI, from the position of its maximum and its value at the maximum I_{bias}, respectively.It can be seen that both I_{c} and G fluctuate in an aperiodic manner as a function of applied side gate voltage. Measurements over several sweeping cycles indicate that these fluctuations are time-independent and reproducible within the sample. Moreover, we observe that the fluctuation pattern of I_{c} is similar to that of G, indicating a common physical origin. We

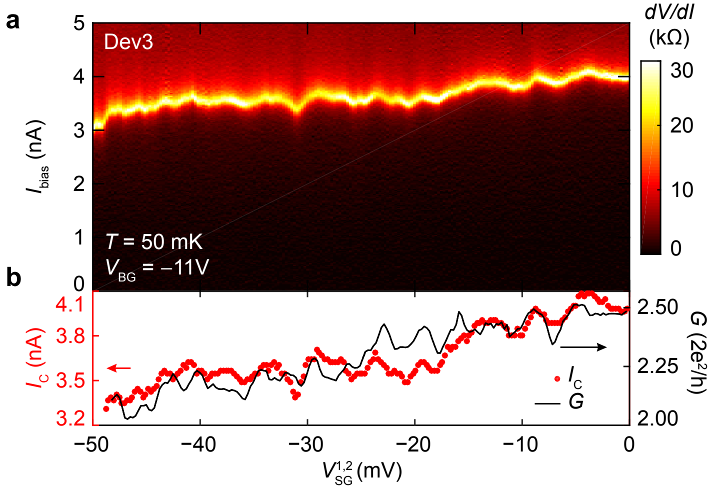

Figure 3.4: (a) Differential resistance (dV/dI) plotted as a function of bias current $I_{\rm bias}$ and side gate voltage $V_{\rm SG}^{1,2}$, measured at $V_{\rm BG} = -11$ V and $T = 50$ mK. (b) Fluctuations of the conductance G and the critical current $I_{\rm c}$ as a function of applied side gate voltage $V_{\rm SG}^{1,2}$.

note the absence of such mesoscopic fluctuations in Dev2 at 1.5 K, due to the low $T_{\rm growth}$ and consequent high sheet resistance.

The mesoscopic fluctuations of the critical current and conductance — so-called universal conductance fluctuations (UCF) — originate from the phase-coherent transport in a system with dimensions comparable to the phase coherence length (L_ϕ), where only a limited number of inelastic scattering centres are involved [98]. Previous transport studies [99] at the LAO/STO interface have yielded a coherence length $L_\phi \sim 110$ nm at 40 mK. From the AFM image we estimate a junction length $L \approx 500$ nm, therefore our c-JJs are expected to display mesoscopic fluctuations.

From the theoretical point of view, fluctuations in the critical current of a Josephson junction have been treated in two limits. For the short junction limit, where the junction length is much shorter than the superconductor coherence length ($L \ll \xi$), Beenakker [100] has shown that the fluctuations are universal and that their amplitude depends only on the superconducting gap Δ: $\delta I_{\rm c}^{\rm rms} \sim e\Delta/h$. One does not expect our devices to fit this regime, since the measured length of the constriction $L \approx 500$ nm is larger than previously reported values [36, 101] $\xi \sim 100$ nm (at optimal doping). In the long junction limit, the reduction in the amplitude of the critical current fluctuations is caused by classical self-averaging due to inelastic scattering events, i.e., $L_\phi < L$. In addition, at finite temperatures thermal averaging needs to be taken into consideration when $k_{\rm B}T > hD/L_\phi^2$, where D is the diffusion constant. The length associated with this dephasing mechanism is the thermal length $L_{\rm T} = \sqrt{hD/k_{\rm B}T}$. Al'tshuler and Spivak [102] have considered the theoretical description of the oscillations in critical current for the case $L_\phi \gg L \gg L_{\rm T}$. Since the aforementioned dephasing mechanisms should contribute to the reduction of the amplitude of mesoscopic oscillations in the same way, we consider an effective length $L_{\text{eff}} = (L_{\text{T}}^{-2} + L_{\phi}^{-2})^{-1/2}$. Then, for the limit $L_{\text{eff}} \gg w, t$, where $t \approx 10\,\text{nm}$ is the thickness of the 2DES [101], the root mean square of the oscillations in critical current becomes [102]

$$\delta I_{\text{c}}^{\text{rms}} = \frac{4ek_{\text{B}}T}{h} \cdot \sqrt{\exp\left(\frac{-2L}{L_{\text{eff}}}\right) \cdot (2\pi)^{5/2} \frac{L}{L_{\text{eff}}}}. \tag{3.2}$$

From the experimentally observed value $\delta I_{\text{c}}^{\text{rms}} = 0.09\,\text{nA}$ we extract $L_{\text{eff}} \approx 100\,\text{nm}$, which provides a relation between L_{T} and L_{ϕ}.

The amplitude of the conductance fluctuations now enables us to extract numerical values for these two length scales. In the microscopic theory of Lee, Stone, and Fukuyama [98], the root mean square of the conductance oscillations (δG^{rms}) was evaluated analytically only in the asymptotic regimes of $L_{\phi} \ll L_{\text{T}}$ and $L_{\text{T}} \ll L_{\phi}$. At the LAO/STO interface, however, these two characteristic length scales are comparable [103], namely, $L_{\phi} \sim L_{\text{T}}$. In order to facilitate comparison with the quasi-1D limit ($w < L_{\text{T}}, L_{\phi} < L$), Beenakker and van Houten have proposed an approximate formula to interpolate between the two asymptotic regimes

$$\delta G^{\text{rms}} = \alpha \cdot \left(\frac{e^2}{h}\right) \cdot \left(\frac{L_{\phi}}{L_x}\right)^{3/2} \cdot \left[1 + (\alpha^2/\beta^2)(L_{\phi}/L_T)^2\right]^{-1/2}. \tag{3.3}$$

We take $\alpha = \beta = 0.73$, which recover the asymptotic results originally obtained in Ref. [98]. From the data in Fig. 3.4b we obtain $\delta G^{\text{rms}} = 0.086e^2/h$, which, together with $L_{\text{eff}} = 100\,\text{nm}$, yields $L_{\phi} \approx 170\,\text{nm}$ and $L_{\text{T}} \approx 120\,\text{nm}$. Hence, we can estimate a diffusion constant $D \approx 0.16\,\text{cm}^2/\text{s}$ and a Thouless energy $E_{\text{Th}} = D\hbar/L_{\phi}^2 \approx 0.4\,\mu\text{eV}$. As previously mentioned, we expect the studied device to belong to the long junction limit based on the value of L estimated from the AFM image. In this regime, the Thouless energy should be the dominant energy scale, i.e., $E_{\text{Th}} \ll \Delta$. Within the range of side gate voltages considered, $eI_{\text{c}}R \approx 20\,\mu\text{eV}$, which allows us to estimate $\Delta \approx 7$ - $14\,\mu\text{eV}$. Hence, the value of E_{Th} determined from the combined analysis of the critical current and conductance fluctuations is in good agreement with the long junction limit.

Finally, we demonstrate the tunability offered by the side gates by integrating two side gated c-JJs in a superconducting loop to create a SQUID. Figure 3.5a shows an AFM image of the device which comprises a left (SG_{L}) and right (SG_{R}) side gate electrode to allow independent control of each c-JJ. If an external magnetic field is applied perpendicularly to the superconducting loop, the measured critical current oscillates periodically with the changes in phase at the two c-JJ junctions, as seen in Fig. 3.5b. We plot the differential resistance in color scale as a function of current bias (I_{bias}) and applied (out-of-plane) magnetic field (B) for different combinations of side gate voltages. We start by investigating the case when no voltages are applied to the side gate electrodes (top panel), where periodic oscillations of the critical current as a function of magnetic field are observed. The period of these oscillations is $\Delta B = 19\,\mu\text{T}$, which yields an effective loop area $A_{\text{eff}} = h/2e\Delta B$ of approximately $8 \times 8\,\mu\text{m}^2$, indicated by the dashed line in 3.5a. The difference between the estimated effective area and the area of the central insulating region ($5 \times 5\,\mu\text{m}^2$) is expected, and originates from flux-focusing effects due to the fact that the dimensions of the SQUID are smaller than the Pearl length ($\sim 1\,\text{mm}$) [88].

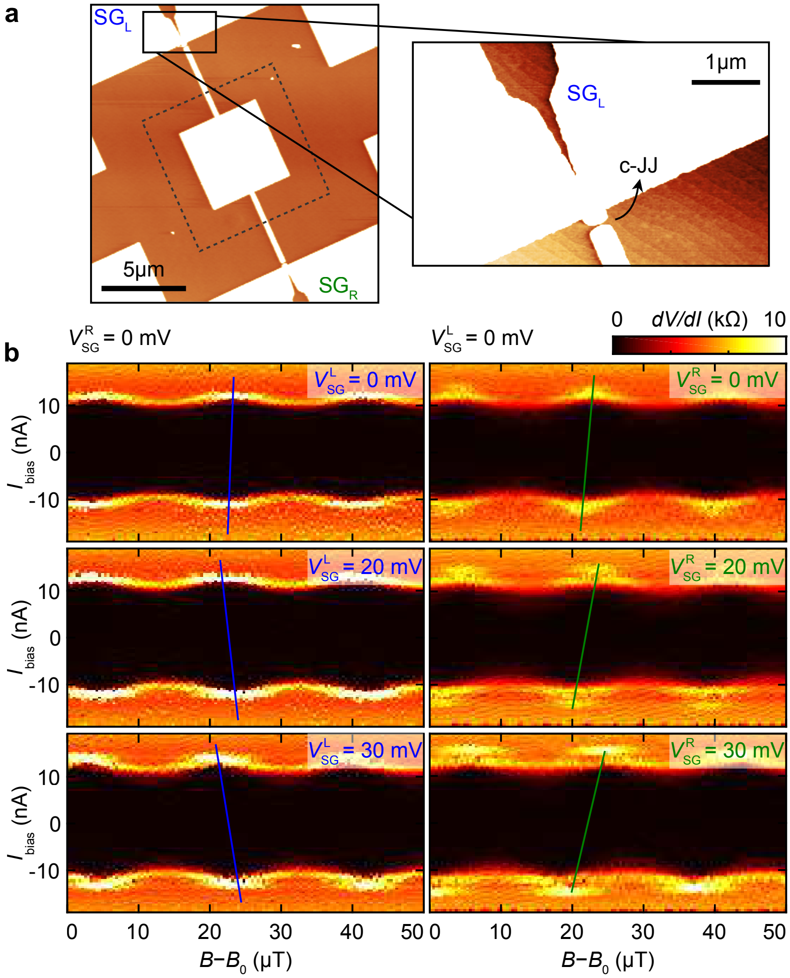

Figure 3.5: (a) AFM image of the SQUID device which comprises a left (SG$_\mathrm{L}$) and right (SG$_\mathrm{R}$) side gate electrodes. Inset: c-JJ of the left arm and the the respective side gate electrode. (b) Tunability of the the SQUID oscillations. Left column: $V^\mathrm{R}_\mathrm{SG} = 0\,\mathrm{mV}$ and different values of V^L_SG. Right column: $V^\mathrm{L}_\mathrm{SG} = 0\,\mathrm{mV}$ and different values of V^R_SG. B_0 is an experimentally determined offset in the magnetic field and has an uncertainty greater than one oscillation period.

However, a small offset along the B-axis can be observed between the oscillations of positive and negative critical current. This asymmetry arises due to self flux effects, which are particularly important for SQUIDs with a large kinetic inductance (L_k). This is indeed the case for SQUIDs made at the LAO/STO interface [88], where the low superfluid density results in an exceptionally large kinetic inductance. The tunability of the superfluid density by electric field-effect therefore provides a direct way to modulate the kinetic inductance through the application of a gate voltage. In our device, the reduced width of the c-JJs causes the kinetic inductance of each arm to be dominated by the weak link. The local modulation of the side gates therefore simultaneously affects the critical current of the weak link and the kinetic inductance of the arm. Thus, the independent tunability of each c-JJ should allow for the control of the asymmetry in the positive and negative critical current oscillations. By keeping $V_{\mathrm{SG}}^{\mathrm{R}}$ fixed at 0 mV while driving $V_{\mathrm{SG}}^{\mathrm{L}}$ to positive values (left column), the offset of the positive and negative $I_{\mathrm{c}}(B)$ along the B axis increases, as denoted by the blue lines connecting two maxima of both branches. In turn, when $V_{\mathrm{SG}}^{\mathrm{L}}$ is kept fixed at 0 mV and $V_{\mathrm{SG}}^{\mathrm{R}}$ made more positive (right column), the offset occurs in the opposite direction, as expected. This underlines the reliability of the side gate geometry in providing independent modulation of the c-JJs, thus enabling the control of the SQUID asymmetry.

3.5. CONCLUSION

In summary, we have realized nanoscale constrictions at the LAO/STO interface in conjunction with side gate electrodes, which are patterned in the 2DES itself, allowing for a single lithography step process. We have shown that such side gates allow for the reliable local modulation of transport across the constriction by electric field-effect. Finite element simulations show that, due to the electric field dependence of the permittivity of STO, the action of these side gate electrodes is comparable to that of an effective "local back gate". Transport measurements in the normal state have corroborated the reliability of the pre-patterning technique used, by demonstrating a symmetric action of both side gates. In the superconducting regime, mesoscopic oscillations of conductance and Josephson supercurrent allow for the estimation of L_{ϕ} and L_{T}. Lastly, we integrate two side gated c-JJs in a superconducting loop to realize a SQUID. The subsequent control of the (a)symmetry of the SQUID response via the side gate electrodes underscores the reliability of our single-step technique. We demonstrate efficient local electrostatic control of the c-JJs, with the additional advantage of not requiring any post processing after the LAO growth. The results reported in this chapter open exciting perspectives for the study of quasi-one dimensional superconductivity and for the realization of devices such as superconducting quantum point contacts.

3.6. SUPPLEMENTAL INFORMATION

3.6.1. FABRICATION

The steps for the fabrication of the nanoscale constrictions and side gate electrodes are illustrated in Fig. 3.6a. As previously discussed, a template with the desired pattern is realized on the STO substrates by depositing a thin AlOx layer before the epitaxial growth of the LAO thin film. To this purpose, we use a single-step electron beam lithography procedure optimized for insulating materials.

The process starts off with single crystal TiO_2-terminated STO(001) substrates, purchased from CrysTec GmbH. A double-layer layer of positive resist (PMMA 495K/950K) is spun on the surface of the as-received substrates and subsequently covered by a conductive protective coating for e-beam resist (Elektra 92). This layer acts as a charge dissipation layer, thus reducing accumulation of surface charges on the STO insulating substrate. The pattern resolution and the exposure dose required due to the added Elek-

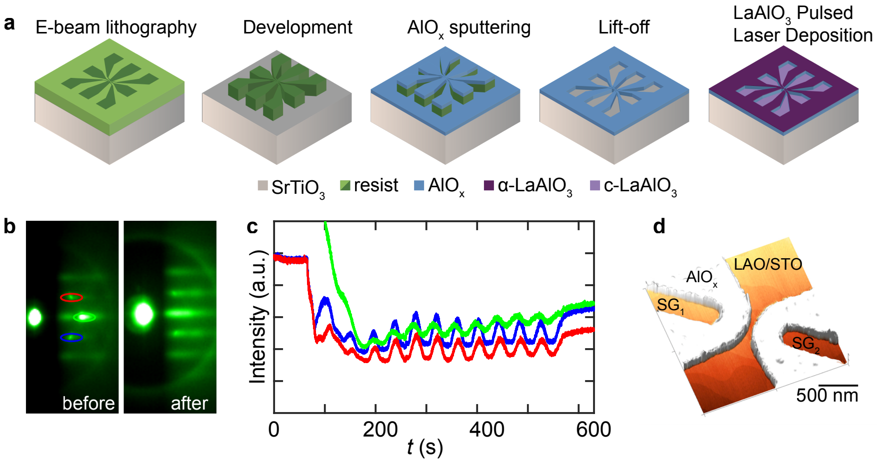

Figure 3.6: (a) Schematic representation of the fabrication process steps. (b) Reflection high energy electron diffraction (RHEED) patterns before (left) and after (right) LaAlO$_3$ deposition. (c) RHEED oscillations obtained during the deposition. (d) Atomic force microscopy image of a side gated device.

tra layer have been studied and optimized. The optimal dose for a beam-spot size of 3 nm was 850 μC/cm^2. After exposure, the Elektra layer layer is removed by dipping in DI-water, after which the PMMA is developed using a diluted methyl isobutyl ketone (MIBK) solution, revealing the pattern. After development, we sputter a thin (~ 13 nm) AlOx layer, before removing the resist with a lift-off procedure. With the described procedure, we obtain an insulating hard-mask with the desired pattern on the STO substrate. Finally, crystalline LAO (c-LAO) is grown via pulsed laser deposition (PLD), monitored in-situ by reflection high energy electron diffraction (RHEED) to confirm layer-by-layer growth (Fig. 3.6c). The RHEED diffraction pattern corroborates the two-dimensional nature of the growth (Fig. 3.6b). The LAO films are grown at an oxygen pressure of 6×10^{-5} mbar and two different temperatures: 770°C and 840°C. Lower growth temperature results in samples with lower carrier densities, whereas samples grown at higher temperature exhibit higher carrier density and superconductivity. A KrF excimer laser with a fluency of 1 J/cm^2 and a repetition rate of 1 Hz is used. Immediately after deposition, the samples are annealed in oxygen: the deposition chamber is filled with 300 mbar of oxygen and the sample temperature is kept at 600° for 1 hour. The sample is then slowly cooled down to room temperature in the same oxygen atmosphere. After growth, a metallic back gate is established with silver conductive epoxy on the back of the STO substrate. Ultrasonic wedge bonding with Al wire is used to make electrical contact to the conducting regions. An atomic force microscope image of a side gated nano-constriction realized with this technique is shown in Fig. 3.6d.

3.6.2. ESTIMATION OF THE LITHOGRAPHIC LENGTH OF THE CONSTRICTION

The length of the constriction was estimated from the AFM images, as shown in Fig. 3.7. The edges of the narrow region are defined by 2 large circles, which then open up in a linear fashion, at a 45° angle. The length was estimated by extrapolating the lines tangent to the circles and taking their intersection at both ends of the channel. This yields $L \approx 500\,\text{nm}$.

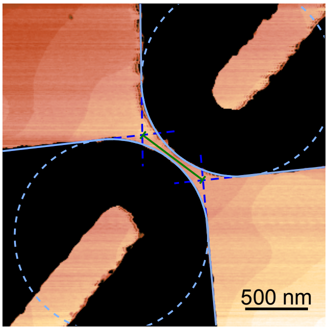

Figure 3.7: Schematic representation of the estimation of the lithographic length of the constriction.

3.6.3. DETERMINATION OF G, I_c, δG^{rms} AND δI_c^{rms}

The values of I_c and G were both determined from the differential resistance dV/dI curves, from the position of the maximum and the value of the normal state resistance at $I_{\text{bias}} = 10\,\text{nA}$, respectively, as shown in Figs. 3.8a and 3.8b.

To extract the values of quadratic mean of the fluctuations in G and I_c, we first remove the monotonically decreasing background component that arises from the decrease in carrier density induced by the application of negative voltages in the side gate electrodes. In both cases, this is done by subtracting a second degree polynomial fitted to the data. The fits to G and I_c as a function of side gate voltage are shown in Figs. 3.8c and 3.8d, respectively. The resulting fluctuations after subtraction of the background modulation, which are used to determine δG^{rms} and δI_c^{rms}, are shown in Fig. 3.8e.

3.6.4. REPRODUCIBILITY OF THE MESOSCOPIC FLUCTUATIONS

In order to confirm that the observed fluctuations are time-independent and reproducible, we have compared the fluctuation patterns of two different sweeps. Figure 3.9 shows the variations in G and I_c as a function of side gate voltage, where a good agreement is observed between both measurements.

3.6.5. FLUCTUATIONS OF R_N AND I_c AS A FUNCTION OF THE INDIVIDUAL SIDE GATE VOLTAGES

The independent control of the side gates enables the investigation of the fluctuations in R_N and I_c as a function of the independent side gate voltages V_{SG}^1 and V_{SG}^2, as shown in Figs. 3.10a and 3.10b, respectively. In both cases, a similar pattern of fluctuations is revealed which is not symmetric across the diagonal. As mentioned before, these fluctuations appear at sufficiently low temperatures, stemming from phase coherent effects determined by the local disorder potential. Figure 3.10c shows a spatial map of the calculated out-of-plane electric polarization in a configuration of asymmetric biasing of

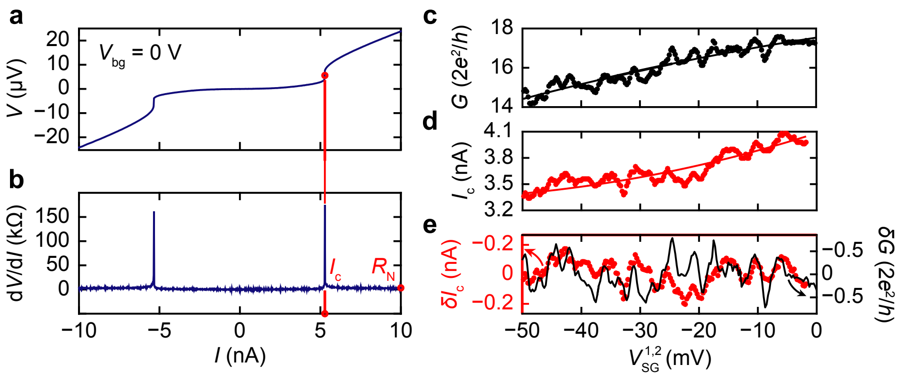

Figure 3.8: (a) VI characteristic and (b) corresponding differential resistance dV/dI curve, recorded at $V_{\mathrm{bg}} = 0\,\mathrm{V}$. (c) Conductance G and (d) critical current I_{c} as a function of applied side gate voltage. Solid lines correspond to fits to a second degree polynomial fits. (e) Fluctuations δG^{rms} and $\delta I_{\mathrm{c}}^{\mathrm{rms}}$ as a function of applied side gate voltage after subtraction of the background modulation.

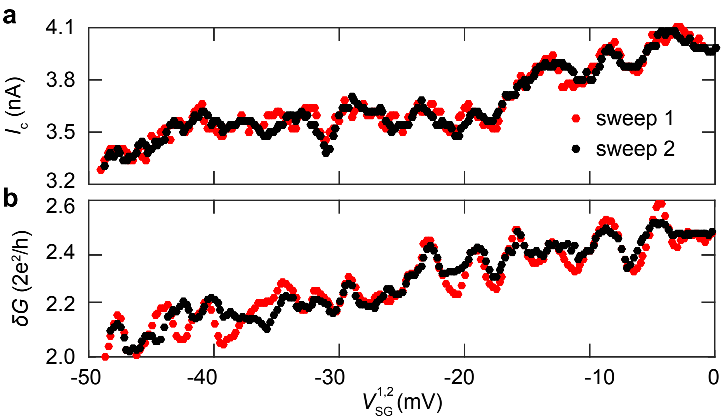

Figure 3.9: (a) Critical current I_{c} and (b) conductance G oscillation patterns for two different measurements.

the side gates. One can immediately observe that the charge depletion is strongest at the constriction edge near SG_2. A closer look at the polarization profile for this configuration (Fig. 3.10d) indeed shows that the minimum of the magnitude of P is not located in the middle of the constriction, but shifted towards SG_1. Moreover, when V_{SG}^1 is kept fixed at 10 mV and V_{SG}^2 assumes progressively lower values, the minimum of P continuously shifts towards SG_2, as shown in Fig. 3.10e. Thus, asymmetric biasing of the side gates results in probing different regions of the channel. Since the impurities responsible for the scattering of the itinerant electrons are randomly distributed across the constriction, switching V_{SG}^1 and V_{SG}^2 effectively results in probing a different disorder landscape, hence the lack of symmetry across the diagonal in the maps of R_{N} and I_c.

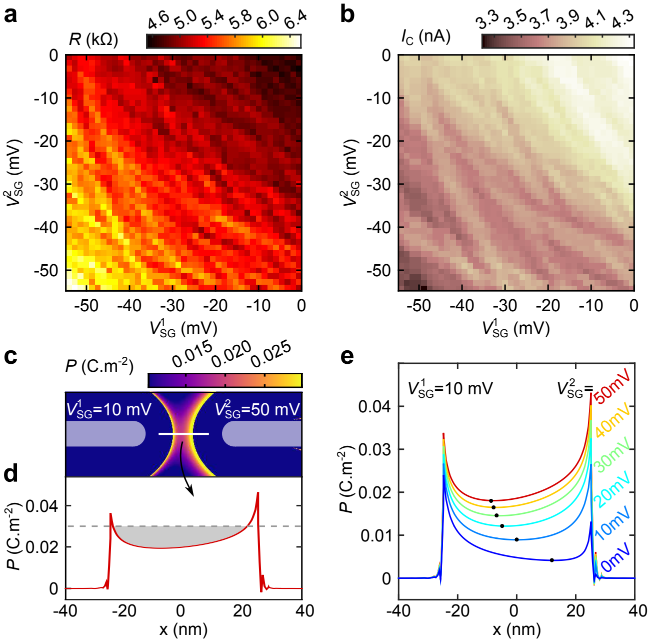

Figure 3.10: (a) 2D map of resistance (R) and (b) critical current I_c as a function of side gate voltages V^1_{SG} and V^2_{SG}, measured at $V_{BG} = -11\,V$ and $T = 50\,mK$. (c) Spatial map of the out-of-plane electric polarization P from FEA under asymmetric bias of the side gates ($V^1_{SG} = -10\,mV$ and $V^2_{SG} = -50\,mV$) and (d) corresponding cut-line at the constriction center showing the polarization profile. (e) Electric polarization P across the channel (along the white line in panel c) for V^2_{SG} ranging from 0 to $-50\,mV$ while V^1_{SG} is fixed at $-10\,mV$. The black dots indicate the minimum magnitude of P for each profile.

4

TWO-DIMENSIONAL SUPERCONDUCTIVITY AT THE (111)LAALO$_3$/SRTIO$_3$ INTERFACE

We report on the discovery and transport study of the superconducting ground state present at the (111)LaAlO$_3$/SrTiO$_3$ interface. The superconducting transition is consistent with a Berezinskii–Kosterlitz–Thouless transition and its 2D nature is further corroborated by the anisotropy of the critical magnetic field, as calculated by Tinkham. The estimated superconducting layer thickness and coherence length are 10 nm *and* 60 nm*, respectively. The results provide new insight to clarify the microscopic details of superconductivity in LAO/STO interfaces, in particular in what concerns the link with orbital symmetry.*

Parts of this chapter have been published in Physical Review B **96**, 020504(R) [104].

TRansition metal oxide interfaces host a rich spectrum of functional properties which are not present in their parent bulk constituents [14]. Following the ground-breaking discovery of a high-mobility two-dimensional electron system (2DES) at the interface between the two wide band-gap insulators $LaAlO_3$ (LAO) and $SrTiO_3$ (STO) [16], a growing body of research efforts have brought to light many of its interesting properties. The system features a gate tunable metal-to-insulator transition[105, 106], strong Rashba spin–orbit coupling [47] and superconductivity[36], possibly in coexistence with magnetism[52, 53]. To date, the vast majority of research efforts has been directed towards the investigation of the (001)-oriented LAO/STO interface. However, it is well recognized that the direction of confinement plays a pivotal role in determining hierarchy of orbital symmetries and, consequently, in properties such as the spatial extension of the 2DES and the Rashba spin–orbit fields [107]. Recent work suggests that (111)-oriented ABO_3 perovskites are potentially suitable for the realization of topologically non-trivial phases [108], since along this direction a bilayer of B-site ions forms a honeycomb lattice. The 2DES at the (111)LAO/STO interface [109] is an interesting subject of investigation, combining a polar discontinuity at the interface with such a hexagonal lattice. Signatures of the 6-fold symmetry related to the (111)STO orientation have recently been observed by angle-resolved photoemission spectroscopy [110, 111] (ARPES) and magnetoresistance[112, 113] measurements, making the system potentially suitable for exotic time-reversal symmetry breaking superconductivity[114]. Moreover, ARPES measurements at the surface of (111)STO have confirmed a distinct orbital ordering of the t_{2g} manifold[110], where all the bands are degenerate at the Γ-point. This implies the absence of a Lifshitz point, considered to be at the origin of many physical properties at the (001)-oriented interface. In particular, the ‘optimal doping’ for superconductivity was found to occur concomitantly with the Lifshitz transition [39]. Therefore, within this view, it is timely to investigate whether a 2D superconducting ground state arises at the (111) orientation.

4.1. FABRICATION

The (111)LAO/STO interface under investigation was prepared by pulsed laser deposition. An LAO film with a thickness of 9 unit cells (u.c.) was epitaxially grown on a commercially available (111)STO substrate with Ti-rich surface. The film was deposited at 840°C in an oxygen pressure of 6×10^{-5} mbar. The laser pulses were supplied by a KrF excimer source ($\lambda = 248$ nm) with an energy density of 1 J/cm^2 and a frequency of 1 Hz. The growth process was followed by an annealing step in order to refill oxygen vacancies. The chamber was filled with 300 mbar of oxygen and the sample temperature was kept at 600°C for 1 hour. The sample was then cooled down to room temperature at a rate of 10° C/min in the same oxygen atmosphere. The growth process was monitored *in-situ* using reflection high-energy electron diffraction (RHEED), which indicates a layer-by-layer growth mode, as shown in Fig. 4.1a. An atomic force microscope (AFM) topographic image of the surface after growth is shown in Fig. 4.1b, where an atomically flat surface with step-and-terrace structure can be observed. The step height corresponds to the (111)STO interplanar distance (≈ 0.26Å). Transport measurements were carried out in a Hall bar geometry, as shown in Fig. 4.1c. The fabrication process relied on argon

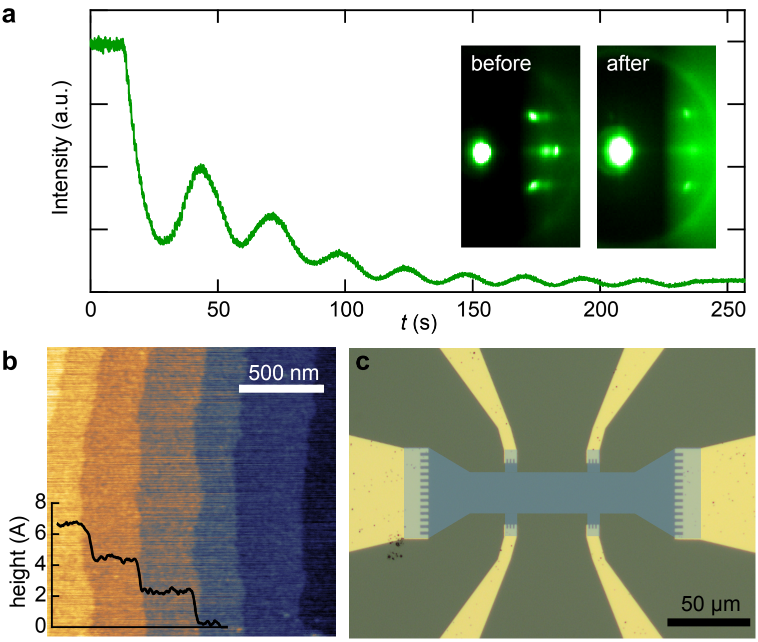

Figure 4.1: (a) RHEED intensity oscillations of the specular spot during the epitaxial growth of a 9 u.c. $LaAlO_3$ film on a (111)$SrTiO_3$ substrate. Inset: RHEED pattern before and after growth. (b) AFM topographic image of the surface after growth. Inset: height profile. (c) Optical image of a Hall bar. The channel is false-coloured in blue.

dry etching in order to define the channel and e-beam evaporation of metal contacts (for a detailed description, see Supplemental Information). Hall bars were patterned along different in-plane orientations (0°, 30°, 60°, and 90°) in order to investigate possible anisotropies in the transport properties.

4.2. Berezinskii–Kosterlitz–Thouless transition

The temperature dependence of the sheet resistance (R) is shown in Fig. 4.2a, evidencing a clear metallic behavior and absence of carrier localisation down to 1.5 K. At this temperature the back gate voltage is swept to the maximum applied voltage (90 V) and back to 0 V. At variance with previous reports, we observed no hysteretic or anisotropic transport behavior attributed to the presence of oxygen vacancies [115]. All further measurements presented in this work are shown for one Hall bar recorded at a fixed back gate voltage of 30 V. The detailed investigation of the evolution of the transport properties with electrostatic doping shall be discussed elsewhere.

In the milliKelvin regime, a superconducting transition with a critical temperature $T_c \approx 117\,\mathrm{mK}$ is observed (Fig. 4.2a). The value of T_c was defined as the temperature at which the resistance is 50% of its normal state value (R_n, measured at $T = 180\,\mathrm{mK}$). The width of the transition, defined between 20% and 80% of R_n, is $\Delta T_c = 17\,\mathrm{mK}$.

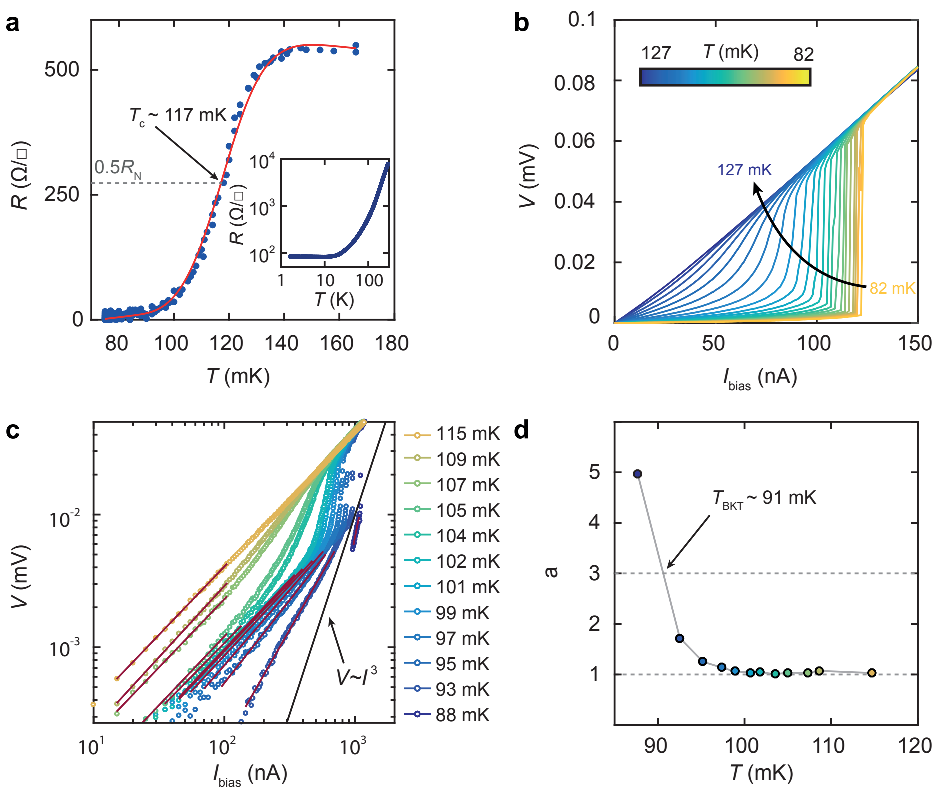

Figure 4.2: (a) Sheet resistance (R) as a function of temperature (T) in the milliKelvin regime with an applied back gate voltage of 30 V. Inset: $R(T)$ in the high-temperature range down to 1.5 K. (b) $V(I)$ characteristics measured at different temperatures. (c) Selected curves of panel (b) plotted in logarithmic scale. The red lines are fits of the data along the transition. The black line corresponds to $V \propto I^3$. (d) Temperature dependence of the power-law exponent $a(T)$ as deduced from the fits shown in (c).

For a 2D system, it is well established that superconductivity should exhibit a Berezinskii–Kosterlitz–Thouless (BKT) transition, at a characteristic temperature T_{BKT}. Below this temperature, vortex-antivortex pairs are formed. As the temperature increases and approaches T_{BKT}, a thermodynamic instability occurs and the vortex-antivortex pairs spontaneously unbind into free vortices. The resulting proliferation of free vortices destroys superconductivity, yielding a finite-resistance state. According to the BKT scenario, a strong non-Ohmic behavior in the $V(I)$ characteristics emerges near T_{BKT}, following a power law behavior $V \propto I^{a(T)}$ with $a = 3$ at T_{BKT}.

In order to investigate the 2D character of superconductivity in the system, we measured the $V(I)$ characteristics of a 9 u.c. (111)LAO/STO interface as a function of temperature. The characteristics were recorded from 82 mK, where the samples are completely superconducting, up to the temperature at which the sample fully recovers to the normal state. As shown in Fig. 4.2b, there is a clear superconducting current plateau for the

$V(I)$ curve at 82 mK. As the temperature is increased, the supercurrent plateau becomes progressively shorter, until it vanishes at approximately 127 mK. At this temperature, the $V(I)$ curve becomes completely linear. Concomitantly with the disappearance of the superconducting plateau, power-law type $V(I)$ curves emerge, indicating a BKT transition. In order to confirm this scenario, we plot the $V(I)$ characteristics on a logarithmic scale, as shown in Fig. 4.2c. At sufficiently low current, the $V(I)$ characteristics display Ohmic behaviour in the entire temperature range due to well-known finite size effects [116, 117]. At higher current values, the $V(I)$ curves show a clear $V \propto I^{a(T)}$ power-law dependence, as indicated by the red lines. The black line corresponds to $V \propto I^3$. The exponents $a(T)$ are obtained by fitting all the characteristics and are plotted as a function of temperature in Fig. 4.2d, revealing that $T_{\mathrm{BKT}} \approx 91$ mK. At $T > T_{\mathrm{BKT}}$, $V \propto I$ at low currents, transitioning to a strongly non-linear behaviour at higher currents and showing the characteristic rounding. In contrast, at $T < T_{\mathrm{BKT}}$ the power-law behaviour terminates abruptly with a voltage jump at a well defined current. It should be noted that the evolution of $a(T)$ does not display the characteristic discontinuous jump from $a(T^+_{\mathrm{BKT}}) = 1$ to $a(T^-_{\mathrm{BKT}}) = 3$, but rather transitions smoothly from 1 to 3 over a range of several milliKelvin. This behaviour, also observed in (001)- and 110)-oriented interfaces [36, 118], stems from inhomogeneties in the local superconducting properties of the system (such as inhomogeneous superfluid density [79] or structural twin domains of the STO substrate [119]) which smear the universal jump [120].

4.3. SUPERCONDUCTING COHERENCE LENGTH AND THE LAYER THICKNESS

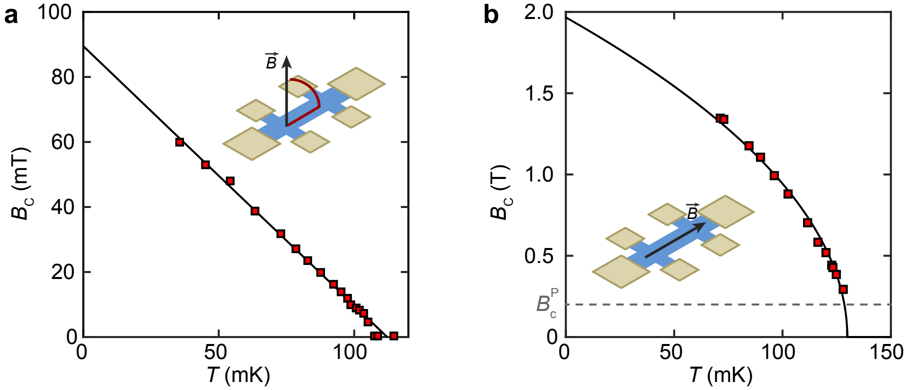

Figure 4.3: (a) Out-of-plane and (b) in-plane critical magnetic field as a function of temperature. Dashed line: Pauli-limiting field.

For a quantitative estimation of both the superconducting coherence length (ξ) and the layer thickness d, we carried out an analysis based on the Ginzburg–Landau formalism. To this purpose, a quantitative criterion was chosen in order to determine the out-of-plane ($B_c^{\perp}$) and in-plane ($B_c^{\parallel}$) critical magnetic fields. At each temperature, $V(I)$ characteristics are recorded for increasing values of applied magnetic field. As shown in the

Supplemental Information, for small applied magnetic fields, the values of $dV/dI_{I=0\,\mathrm{nA}}$ are zero at low currents, corresponding to the superconducting state. As the current rises, dV/dI increases until a saturating value, $dV/dI_{I=200\,\mathrm{nA}}$, which corresponds to the normal state resistance. For larger applied magnetic fields, $dV/dI_{I=0\,\mathrm{nA}}$ is non-zero, and its value increases with the magnitude of the applied magnetic field. We define the critical magnetic field as the value at which $dV/dI_{I=0\,\mathrm{nA}}$ reaches 50% of the normal state resistance, i.e., $(dV/dI)_{I=0\,\mathrm{nA}}/(dV/dI)_{I=200\,\mathrm{nA}} = 0.5$. We track the temperature evolution of the critical magnetic field for the out-of-plane and in-plane orientations, which are shown in Figs. 4.3a and 4.3b, respectively. The black lines represent a fit to the expected dependence for a 2D superconductor, i.e.,

$$B_{\mathrm{c}}^{\perp} = \frac{\Phi_0}{2\pi\xi^2}(1 - T/T_{\mathrm{c}}) \tag{4.1}$$

and

$$B_{\mathrm{c}}^{\parallel} = \frac{\Phi_0\sqrt{12}}{2\pi\xi d}(1 - T/T_{\mathrm{c}})^{1/2}. \tag{4.2}$$

From the extrapolation of the critical magnetic fields at $T = 0\,\mathrm{K}$, we extracted the in-plane coherence length $\xi = \sqrt{\frac{\Phi 0}{2\pi B_{\mathrm{c,0K}}^{\perp}}} \approx 60\,\mathrm{nm}$ and the thickness of the superconducting layer $d = \frac{\Phi_0\sqrt{3}}{\pi\xi B_{\mathrm{c,0K}}^{\parallel}} \approx 10\,\mathrm{nm}$. The fact that the superconducting coherence length is larger than the estimated thickness is consistent with the 2D character of superconductivity.

In fact, $B_{\mathrm{c}}^{\parallel}$ can seemingly go far beyond the Pauli paramagnetic limit, which gives a higher bound for the upper critical magnetic field resulting from field-induced pair-breaking [121, 122]. For weak coupling Bardeen-Cooper-Schrieffer (BCS) superconductors, this value is given by

$$B_{\mathrm{c}}^{\mathrm{P}} \approx 1.76 k_{\mathrm{B}} T_{\mathrm{c}}/\sqrt{2}\mu_{\mathrm{B}}, \tag{4.3}$$

where k_{B} is the Boltzmann's constant and μ_{B} is the Bohr magneton.

Violation of the paramagnetic limit has been observed in (001)- and (110)-oriented LAO/STO interfaces[48, 101, 118], as well as in other STO-based superconductors [123]. In these systems, the paramagnetic limit is exceeded by a factor of approximately 3-5. In our case, we find $B_{\mathrm{c}}^{\mathrm{P}} \approx 200\,\mathrm{mT}$, which results in a violation of the Pauli paramagnetic limit by a factor of 10, since $B_{\mathrm{c,0K}}^{\parallel} \approx 2000\,\mathrm{mT}$. As a matter of fact, the violation is already present at temperatures very close to T_{c}, as shown by the dashed line in Fig. 4.3b. The enhancement of $B_{\mathrm{c}}^{\parallel}$ well beyond the BCS prediction has been reported in superconductors which display strong spin–orbit effects [124–126]. These are expected to cause randomization of electron spins, and thus result in suppression of the effect of spin paramagnetism [127]. Indeed, we have confirmed the presence of strong spin–orbit fluctuations in the system by magnetotransport measurements (see Supplemental Information), suggesting that spin–orbit coupling plays an important role in the violation of the Pauli paramagnetic limit.

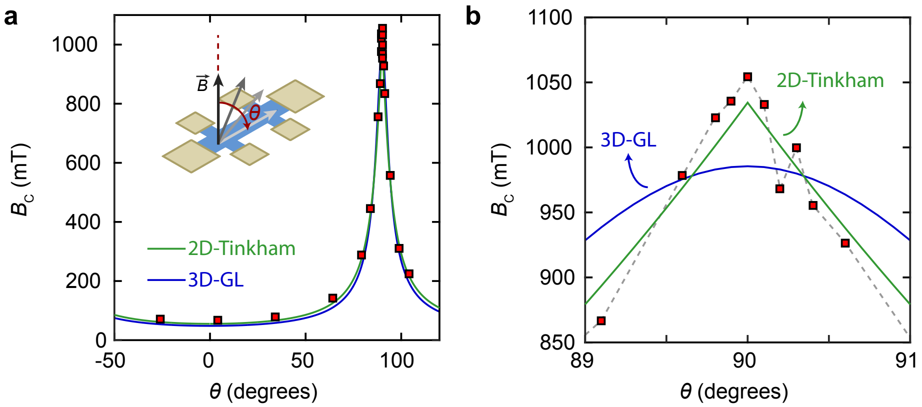

Figure 4.4: (a) Angular dependence of the critical magnetic field B_c, where θ is the angle between the magnetic field and the surface normal. Green line: fit to the 2D Tinkham formula. Blue: fit to the 3D anisotropic Ginzburg-Landau model. (b) Magnified view of the region around $\theta = 90°$.

4.4. ANGULAR DEPENDENCE OF B_c

To further investigate the dimensionality of the superconducting layer, we have studied the angular dependence of the critical magnetic field at $T = 82\,\text{mK}$. Figure 4.4a shows the critical magnetic field as a function of the angle θ, defined between the magnetic field vector and the normal to the surface. The data was fitted with the 2D Tinkham formula (green curve) and the 3D anisotropic Ginzburg–Landau model (blue curve), given by

$$\frac{B_c^\theta\,|\cos(\theta)|}{B_c^\perp} + \left(\frac{B_c^\theta \sin(\theta)}{B_c^\parallel}\right)^2 = 1 \tag{4.4}$$

and

$$\left(\frac{B_c^\theta \cos(\theta)}{B_c^\perp}\right)^2 + \left(\frac{B_c^\theta \sin(\theta)}{B_c^\parallel}\right)^2 = 1, \tag{4.5}$$

respectively. For the overall range, the data seems to be well described by both models. However, a closer look at the region around $\theta = 90°$ in Fig. 4.4b reveals a clear difference between the two models: the 3D model yields a rounded maximum when the magnetic field vector is completely in plane, while the observed cusp-shaped peak can only be well captured by the 2D model.

4.5. CONCLUSION

In summary, by means of systematic (magneto)transport measurements we have demonstrated that the electrons hosted at the (111)LAO/STO interface condense into a superconducting ground state with $T_c \approx 117\,\text{mK}$. The estimated thickness of the 2D superconducting layer is approximatelly 10 nm, very similar to the one usually reported for (001)-oriented interfaces. The $V(I)$ characteristics are consistent with a BKT transition, and the two-dimensional character of the superconducting layer was further corroborated by the angular dependence of the critical magnetic field. The Pauli paramagnetic limit is exceeded by a factor of 10, indicating strong spin–orbit coupling in the system. In view of the differences between the symmetries, electronic structure, and orbital ordering of the confined states at the (001)- and (111)-oriented LAO/STO interfaces, further investigation of the latter can extend the current understanding of the link between orbital symmetry and superconductivity at LAO/STO interfaces.

4.6. SUPPLEMENTAL INFORMATION

4.6.1. FABRICATION DETAILS

The steps for the fabrication of the Hall bars are illustrated in Fig. 4.5. The process relied on (1) pulsed laser deposition for the growth, (2) e-beam evaporation of metal contacts and (3) argon dry etching in order to define the channel. To this purpose, we use multiple aligned e-beam lithography steps.

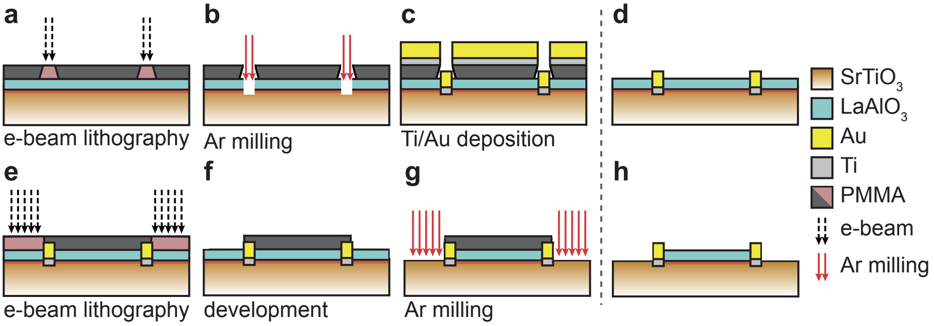

Figure 4.5: Fabrication process of the Hall bars. (a) E-beam lithography to define the areas for Ohmic contacts. (b) Ar milling to etch the LAO film in the regions exposed after step (a). (c) Evaporation of Ti/Au. (d) Sample with Ohmic contacts. (e) E-beam lithography to define the areas of the Hall bars. (f) Development leaves the areas of the Hall bars protected. (g) Ar milling to etch the LAO film in the regions exposed after step (f). (h) Sample with Ohmic contacts and Hall bars defined.

The process starts off with a single-crystal Ti-rich terminated (111)$SrTiO_3$ (STO) substrate, where an $LaAlO_3$ (LAO) layer with a thickness of 9 u.c. is epitaxially is grown via pulsed laser deposition (PLD). As discussed in the main text, the oxide growth is monitored in-situ by reflection high-energy electron diffraction (RHEED) to confirm layer-by-layer growth. The RHEED diffraction pattern corroborates the two-dimensional nature of the growth.

The LAO/STO interface is coated with a single-layer layer of positive resist (PMMA 495kDa), after which the first e-beam lithography step is performed in order to define Ohmic contacts to the interface (see Fig. 4.5a). The dose used for a beam-spot size of ≈ 100 nm was 800 $\mu C/cm^2$. After exposure, the PMMA is developed using a diluted methyl isobutyl ketone (MIBK) solution, revealing the pattern. Next, as shown in Fig. 4.5b, argon milling is used to etch away the LAO layer on the exposed regions. Thereafter, a Ti/Au (3 nm/77 nm) layer is evaporated as shown in Fig. 4.5c, contacting the 2DES through the etched regions. After lift-off in warm acetone, the Ti/Au layer is removed from the regions protected by PMMA, resulting in a structure as depicted in as shown in Fig. 4.5d.

The second e-beam lithography step is used to define the channel of the Hall bar. As shown in Figs. 4.5e and 4.5f, after e-beam exposure and development the area of the metal contacts and the channel is protected by a PMMA layer, while the remaining regions are exposed. Finally, an argon milling step is performed to etch away the exposed LAO layer (see Fig. 4.5g), which defined the channels and isolates the different Hall bars (Fig. 4.5h).

4.6.2. DETERMINATION OF THE CRITICAL MAGNETIC FIELD

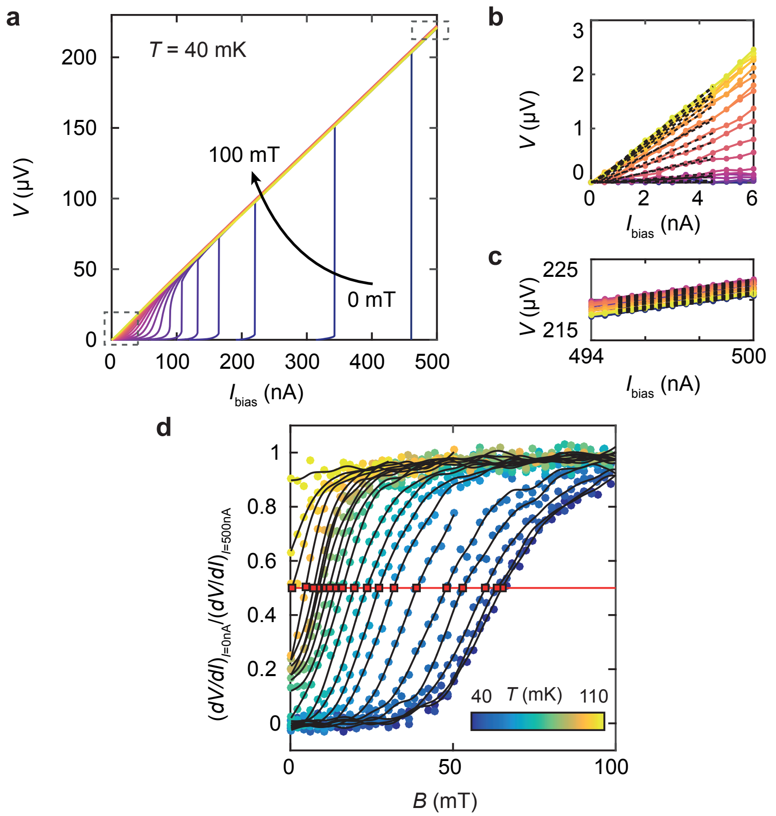

Figure 4.6: Determination of the critical magnetic field. (a) $V(I)$ characteristics at $T = 40\,\mathrm{mK}$ with applied out-of-plane magnetic field. (b) Linear fits performed around $I = 0\,\mathrm{nA}$. (c) Linear fits performed around $I = 500\,\mathrm{nA}$. (d) Ratio between $dV/dI_{I=0\,\mathrm{nA}}$ and $dV/dI_{I=500\,\mathrm{nA}}$ for different temperatures. Red dots indicate the critical magnetic field B_C.

The determination of the critical magnetic field is done by analysis of the differential resistance dV/dI, which is extracted from the $V(I)$ characteristics. Figure 4.6a shows $V(I)$ characteristics recorded at $T = 40\,\mathrm{mK}$ for values of out-of-plane magnetic field between 0 and $100\,\mathrm{mT}$. For each $V(I)$ curve, two values are considered: the differential resistance at low measuring currents, $dV/dI_{I=0\,\mathrm{nA}}$, and in the normal state, $dV/dI_{I=500\,\mathrm{nA}}$. These values are extracted from the slope of the linear fit in the ranges $I \in [0,5]$ nA and $I \in [495,500]$ nA, as shown in Figs. 4.6b and 4.6c, respectively. The magnetic field at which the resistance $dV/dI_{I=0\,\mathrm{nA}}$ recovers to half that of the normal value, i.e., $dV/dI_{I=0\,\mathrm{nA}}/dV/dI_{I=500\,\mathrm{nA}} = 0.5$, was defined as the critical field B_c. Figure 4.6d shows the quantity $dV/dI_{I=0\,\mathrm{nA}}/dV/dI_{I=500\,\mathrm{nA}}$ as a function of applied magnetic field for different temperatures. For each temperature, the critical magnetic field corresponds to the intersection with the horizontal red line.

4.6.3. SPIN–ORBIT COUPLING

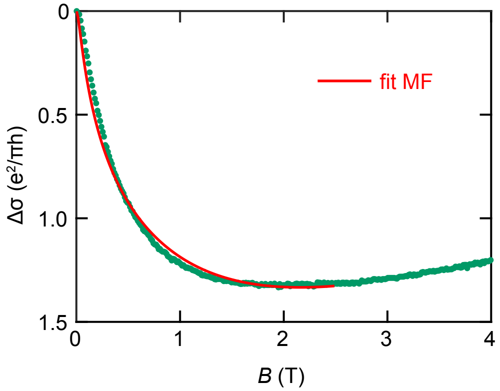

Figure 4.7: Variation of conductance ($\Delta\sigma$) as a function of applied magnetic field (B) and the best fit according to the Maekawa–Fukuyama theory.

We investigate the spin–orbit interaction of the system by magnetotransport measurements. A shown in Fig. 4.7, under an externally applied magnetic field B, a negative correction due the conductance is apparent, pointing towards weak anti-localization. In a 2D system with in-plane spin–orbit relaxation time, the first order correction to the conductance, $\Delta\sigma = \sigma(B) - \sigma(0)$, is given by the Maekawa–Fukuyama (MF) formula [128]:

$$\begin{aligned}\frac{\Delta\sigma}{\sigma_0} &= \Psi\left(\frac{B}{B_\mathrm{i}+B_\mathrm{SO}}\right) + \frac{1}{2\sqrt{1-\gamma^2}}\Psi\left(\frac{B}{B_\mathrm{i}+B_\mathrm{SO}(1+\sqrt{1-\gamma^2})}\right)\\ &-\frac{1}{2\sqrt{1-\gamma^2}}\Psi\left(\frac{B}{B_\mathrm{i}+B_\mathrm{SO}(1-\sqrt{1-\gamma^2})}\right),\end{aligned} \tag{4.6}$$

where $\Psi(x) = \ln(x) + \psi\left(\frac{1}{2}+\frac{1}{x}\right)$, ψ being the digamma function. The parameters of the theory are the inelastic and spin–orbit fields $B_\mathrm{i,SO} = \hbar/4eD\tau_\mathrm{i,SO}$, and the g-factor g which enters into the Zeeman correction $\gamma = g\mu_\mathrm{B}B/4eDB_\mathrm{SO}$. From the best fit of the data in Fig. 4.7 to the MF formula, we obtain $B_\mathrm{SO} \approx 1.31\,\mathrm{T}$ and $B_\mathrm{i} \approx 0.01\,\mathrm{T}$. The fact that we obtain $B_\mathrm{SO} \gg B_\mathrm{i}$ indicates the presence of strong spin–orbit coupling, in good agreement with the weak anti-localization scenario.

5

BAND INVERSION DRIVEN BY ELECTRONIC CORRELATIONS AT THE (111)LAALO$_3$/SRTIO$_3$ INTERFACE

Quantum confinement at complex oxide interfaces establishes a complex hierarchy of the strongly correlated d-orbitals which is widely recognized as a source of emergent physics. The most prominent example is the (001)LaAlO$_3$/SrTiO$_3$ (LAO/STO) interface, which features a dome-shaped phase diagram of superconducting critical temperature and spin–orbit coupling as a function of electrostatic doping, arising from a selective occupancy of t_{2g} orbitals of different character. Here we study (111)-oriented LAO/STO interfaces — where splitting of the t_{2g} manifold due to quantum confinement is absent — and investigate the impact of this unique feature on electronic transport. We show that transport occurs through two sets of electron-like sub-bands, and the carrier density of one of the sets shows a non-monotonic dependence on the sample conductance. Using tight-binding modelling, we demonstrate that this behavior stems from a band inversion driven by on-site Coulomb interactions. The balanced contribution of all t_{2g} orbitals to electronic transport is shown to result in strong SOC with reduced electrostatic modulation.

Parts of this chapter have appeared online in preprint arXiv:1808.03063 and are submitted for peer review [129].

Tight-binding modelling was performed by M. Vivek, P. Bruneel, and M. Gabay. High magnetic field experiments were performed in collaboration with I. Leermakers and U. Zeitler.

Complex oxide interfaces display a variety of emergent physical properties that arise from their highly correlated d-electrons and are therefore absent in conventional semiconductor quantum wells [14, 130]. The two-dimensional electron system (2DES) at the interface between $LaAlO_3$ (LAO) and (001)-oriented $SrTiO_3$ (STO) is the prototypical oxide quantum well [16], featuring several interesting phenomena that include 2D superconductivity [36] and Rashba spin–orbit coupling (SOC) [47, 48]. The hierarchy of d-orbitals with different symmetries imposed by two-dimensional confinement has been recognized as a key element in determining the properties of the system [37]. In particular, it has been proposed that the dome-shaped behavior of the superconducting critical temperature (T_c) and SOC strength with electrostatic doping is related to the selective occupancy of orbitals of different character, detected by a transition from one- to two-carrier transport [39]. On the other hand, recent works have shown that the crystallographic direction of confinement is a powerful tool enabling selective modification of this band hierarchy [107, 109, 131]. (111)-oriented LAO/STO interfaces are of particular interest owing to the absence of splitting of the t_{2g} manifold due to quantum confinement, resulting from their equal projection along this direction [18, 111, 132]. Transport studies have shown that the system condenses into a superconducting ground state [104, 133, 134] and proposed a link between T_c and SOC [134]. More strikingly, field-effect measurements have brought to light an unconventional behavior of the Hall coefficient (R_H), which has been interpreted as a signature of a hole-like band [115, 134, 135].

In this chapter, we investigate the electronic properties of (111)-oriented LAO/STO interfaces and show that (i) transport occurs through electron-like bands and (ii) a band inversion triggered by on-site Coulomb interactions is key to explain the unusual behavior of R_H. Importantly, we show that this band inversion occurs between two sets of t_{2g} sub-bands, each with a balanced contribution of d_{xy}, d_{yz} and d_{xz} character. As a direct consequence of this unique feature, SOC is strong and displays reduced electrostatic tunability.

5.1. POLAR INSTABILITY AND ORIGIN OF THE 2DES

Initially, the study of LAO/STO interfaces was restricted to the (001) crystallographic direction, where the emergence of conduction was originally explained in terms of the polar-catastrophe scenario [16, 24]. In this model, a polar discontinuity arises at the interface between LAO and (001)STO [16] as a consequence of the stacking of charged ionic LAO planes (with alternating valency of $+1e$ and $-1e$) over the neutral STO planes. As a result, the voltage grows with the thickness of the LAO film until the built-in potential becomes larger than ΔE (Fig. 5.1a). At a critical thickness $t_c \approx 3.5\,\text{u.c.}$, this triggers an electronic reconstruction in which half an electron per unit cell is transferred from the surface of the LAO film to Ti $3d$ states at the interface [105, 136]. More recent works have shown that the polar field triggers the spontaneous formation of surface oxygen vacancies, leading to interface conductivity [32, 35].

Viewed along the (111) crystallographic direction, the cubic perovskite lattice consists of three interspersing triangular lattices of Ti atoms, as shown in Fig. 5.1b (where the labels Ti 1, 2 and 3 refer to the distance of the Ti layer with respect to the interface). If

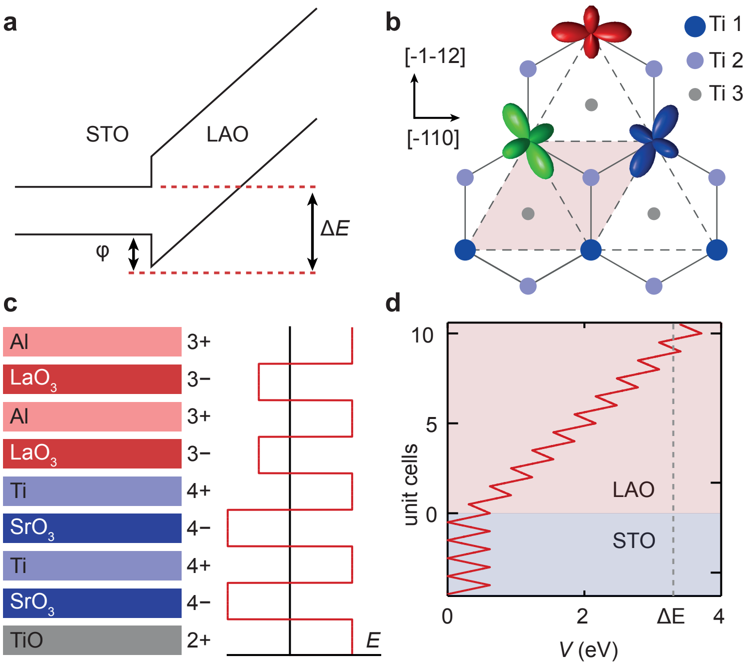

Figure 5.1: (a) Band diagram of the LAO/STO interface before electronic reconstruction. ΔE: critical potential build-up. ϕ: valence-band offset. (b) Top view of three consecutive (111)Ti^{4+} layers. The red shaded area represents the unit cell cross-section of a bilayer. The three t_{2g} orbitals are shown to evidence their equivalent projection onto the 2DES plane. (c) Left: stacking of ionic planes across the interface. The bottom-most Ti^{4+} plane is considered to react with oxygen to form TiO^{2+}. Right: resulting electric field across the interface before the electronic reconstruction takes place. (d) Electrostatic potential as a function of the number of unit cells.

a bilayer of atoms is considered, the projection of the Ti atoms onto the same plane yields an hexagonal lattice, similar to the one found in graphene. A variety of recent works have probed this 6-fold symmetry, which was corroborated by the 2D Fermi surface [110, 111] and anisotropic magnetotransport measurements [112, 113]. The (111)-orientation features highly charged planes both for STO and LAO ($4e+/-$ and $3e+/-$, respectively). In the most simplistic ionic picture, this would bring about a diverging electrostatic potential in the STO substrate itself. To overcome this, we consider an STO(111) slab where the bottom Ti layer is oxidized (see Fig. 5.1c). In this model, the resulting potential on the STO side no longer diverges and, upon growth of the LAO layer, a polar discontinuity at the interface takes place. At the (111)-oriented interface, the interplanar distance is given by $d = a_{\mathrm{LAO}}/\sqrt{3}$ and the unit-cell cross-section A is given by the red shaded region in Fig. 5.1b. Figure 5.1d shows the calculated potential build-up as a function of the number of unit cells of (111)LAO. On the STO side, the potential oscillates between a finite value and zero, starting to diverge on the LAO side. It is worth noticing that the different formal polarization of the successive A-site and B-site sublayers gives rise to an oscillatory potential also on the LAO side, in contrast with the step-like behavior observed in the (001)-oriented case. This simple model for the intrinsic doping mechanism yields a threshold thickness $t_c \approx 8.7$ u.c., in good agreement with recent experimental studies that report a critical thickness of 9 u.c. [137]. The exact value can be slightly affected by defect states or a valence band offset (φ), as observed in the (001)-oriented case [138, 139].

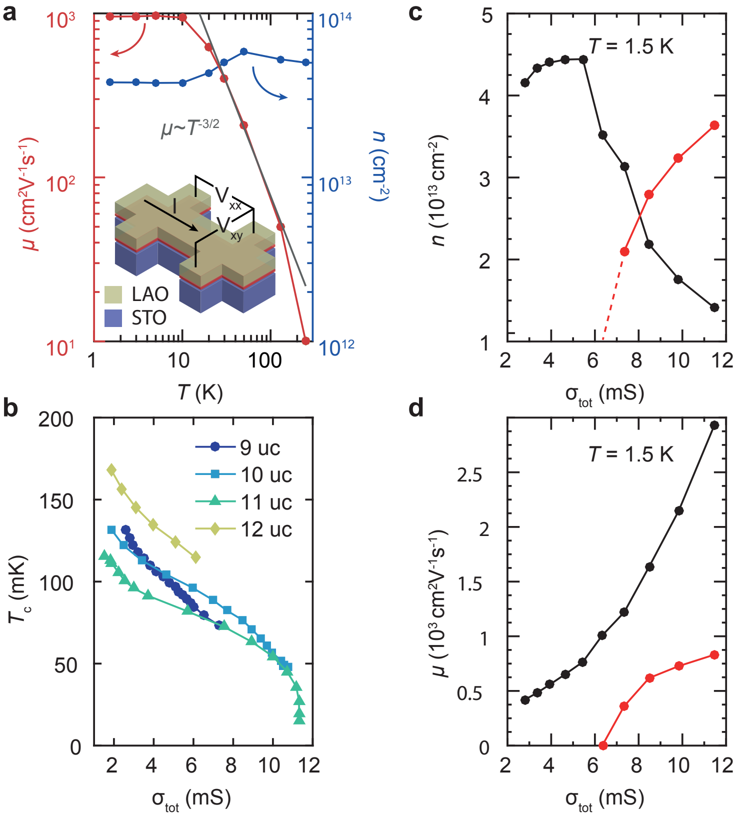

Figure 5.2: (a) Carrier density (n) and mobility (μ) as a function of temperature (T) measured for the pristine state. Inset: schematic representation of the measurement configuration. (b) Superconducting critical temperature (T_c) as a function of sample conductance (σ_tot) for different thicknesses of the LAO film. (c) Carrier densities and (d) mobilities as a function of σ_tot.

5.2. ELECTROSTATIC MODULATION OF CARRIER DENSITY AND SUPERCONDUCTIVITY

Having proposed a possible solution for the polar instability at (111)-oriented LAO/STO interfaces, we investigate the evolution of electronic properties as a function of temperature and electrostatic doping. The temperature dependence of carrier density (n) and mobility (μ) for a 9 u.c. LAO/STO(111) interface is shown in Fig. 5.2a. In the pristine state, the Hall effect remains linear down to 1.5 K in a range of 10 T. The extracted carrier density remains fairly constant around 3-5 × $10^{13}\,\mathrm{cm}^{-2}$ in the entire temperature range. The mobility increases rapidly from $10\,\mathrm{cm}^2\mathrm{V}^1\mathrm{s}^{-1}$ at room temperature to a maximum value of $1000\,\mathrm{cm}^2\mathrm{V}^{-1}\mathrm{s}^{-1}$ at 1.5 K, with saturation occurring below 10 K. The gray line represents the phonon-limited mobility $\mu_{\mathrm{ph}} \propto T^{-3/2}$, showing good accordance with the data at high temperatures. Moreover, the carrier density values obtained are comparable with those reported for (001)-oriented interfaces.

At 1.5 K, we use a back-gate geometry to perform high-field magnetotransport measurements as a function of electrostatic doping. At high conductance values, a transition from linear to non-linear Hall curves is observed, indicating a transition from one- to two-carrier transport. In contrast with previous works [115, 134, 135], the observation of this non-linearity enables us to unequivocally ascertain that the two bands involved in transport are electron-like, and in the Supplemental Material we analytically show that the evolution of R_{H} as a function of B is incompatible with an electron-hole scenario. Figures 5.2c and 5.2d show the extracted values of carrier density ($n_{1,2}$) and mobility ($\mu_{1,2}$) by fitting the Hall curves to a two-band model (see Supplemental Material). The appearance of the second band at $\sigma \approx 6\,\mathrm{mS}$ is readily evident: at this point, n_2 increases rapidly, seemingly at the cost of n_1. Moreover, the second band has a mobility which is roughly 3 times smaller than the first band.

In the millikelvin regime, the system condenses into a superconducting ground state [104] and measurements in the same conductance range reveal a monotonic decrease of T_{c}. This suggests that superconductivity is unaffected by the population of the second electron band at the cost of the first. As shown in Fig. 5.2b, this behavior is consistently observed in several samples, with LAO thicknesses ranging from 9 to 12 u.c.. This is in stark contrast with (001)-oriented interfaces, where the maximum of the superconducting dome occurs concomitantly with the onset of population of the $d_{xz,yz}$ bands at the Lifshitz point. In the (111) crystallographic direction, all the t_{2g} orbitals have the same geometrical projection onto the 2DES plane (see Fig. 5.1b), therefore the observed transition must have an intrinsically different origin than the one observed in the (001) counterpart.

5.3. TIGHT-BINDING MODEL

Tight-binding calculations of the electronic structure of the (111)STO surface derived from photoemission spectra [110, 111] show that for the experimentally accessible range of carrier concentrations, two sets of sub-bands lie close to the Fermi energy E_{F}. Since the 2DES resides on the STO side of the LAO/STO interface, one expects similar tight-binding dispersions for (111)-oriented STO and LAO/STO (this is indeed the case for the (001) orientation [140]). These two sets of sub-bands, labeled 1 and 2 in Fig. 5.3, each contain six branches. However, due to time reversal symmetry, there are only 3 different energies per set, thus leading to a six-band low energy model. In our tight-binding calculations we include the effects of (i) confinement, (ii) bulk SOC, (iii) trigonal field, and (iv) on-site Coulomb interactions, obtaining the band structures in Figs. 5.3a and 5.3b. Here we show the energy E vs. k (along the $k_x = 0$ direction) for two different filling levels after the addition of local Coulomb interactions. k_y corresponds to ΓM of the hexagonal Brillouin Zone (BZ) and k_x corresponds to ΓK of the hexagonal BZ. Both k_x and k_y are in

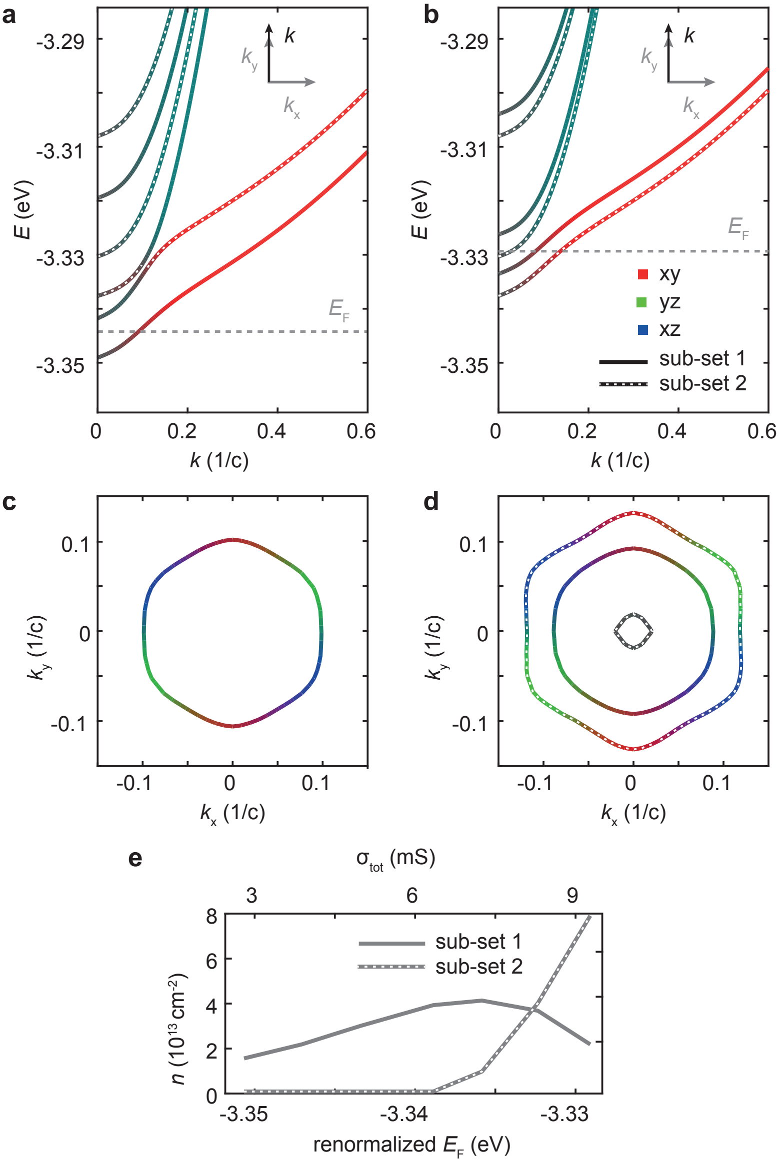

Figure 5.3: (a),(b) Band structure at low and high filling, respectively. Color indicates the orbital character. Stoke indicates the band sub-set. Inset denotes the direction of the k-vector in the reciprocal space. (c),(d) Corresponding Fermi surfaces. (e) Evolution of the carrier density pertaining to the first (n_1) and second (n_2) sub-set of bands as a function of renormalized Fermi level and respective sample conductance.

units of $1/c$, where $c = \sqrt{2/3}a$, and a is the Ti-Ti inter-atomic distance. Hubbard type interactions are added between like (U) and unlike (U$^{'}$) orbitals, which cause the bands to shift by unequal amounts resulting in bands crossings and in changes in the individual carrier concentrations of the bands. In order to keep the total carrier density constant before and after the inclusion of interactions, the Fermi level renormalises. This renormalisation of the Fermi level is performed in a self-consistent way (see Supplemental Material for further details on the theoretical model).

Careful analysis of Figs. 5.3a and 5.3b readily highlights the crucial role of electron correlations in reproducing our experimental observations. At low E_F (Fig. 5.3a), only the first set of sub-bands is populated. At high E_F (Fig. 5.3b), the second set of sub-bands, which extends deeper into the substrate, becomes populated and—most importantly—a band inversion takes place. The second set of sub-bands becomes lower in energy, while the first sub-set is pushed upwards. The consequences of this can be more clearly seen in the corresponding Fermi surfaces plotted in Figs. 5.3c and 5.3d, where the contour of the first set of sub-bands is reduced with increasing E_F. Conversely, it is evident in Fig. 5.3d that the second sub-band becomes heavily populated, its contour becoming larger than that of the first sub-band. It is worth underscoring that, while the orbital character of each band is highly dependent on the crystallographic direction in the BZ, their overall contributions to electronic transport are nearly equal. The concentrations of the carriers in each band are summed for each sub-set and are shown in Fig. 5.3e as a function of E_F. The resemblance with the experimental data is striking: at low filling only the first set of sub-bands contributes to transport and, at a critical filling, the population of the second set of sub-bands starts increasing, concomitantly with a decline of the population of the first one. Our model highlights that, in contrast with the (001) case, the transition from one- to two-carrier transport in the (111) direction stems from the occupation of a second set of t_{2g} sub-bands as a consequence of Coulomb repulsion.

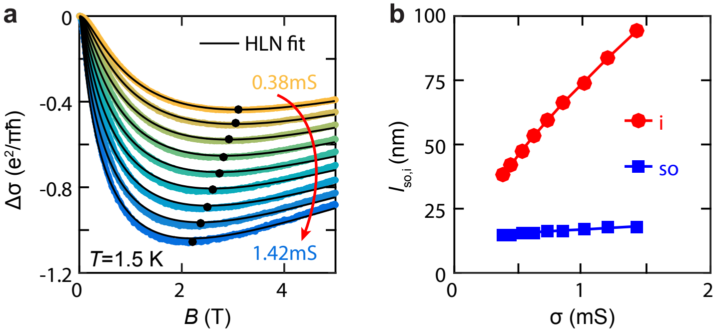

Figure 5.4: (a) Variation of conductance $\Delta\sigma$ as a function of B-field for different levels of electrostatic doping. Black dots: B_min. Black lines: fit to the HLN equation. (b) Extracted characteristic lengths $l_\mathrm{i,so}$.

5.4. SPIN–ORBIT COUPLING

To investigate the effects of the orbital hierarchy of (111)-oriented LAO/STO on SOC, we analysed the field dependence of the magnetoconductance (MC) as a function of electrostatic doping. We restrict our analysis to low conductance values, where the Hall effect is linear and the classical magnetoconductance contribution is negligible (see Supplemental Material). As shown in Fig. 5.4a, negative MC is observed in the entire range of conductance explored, in accordance with previous work [134]. For a 2D diffusive metallic system placed in a perpendicular magnetic field (B), the quantum corrections to conductance are given by the Hikami–Larkin–Nagaoka (HLN) model [141]:

$$\begin{aligned}\frac{\Delta\sigma(B)}{\sigma_0} = & -\frac{1}{2}\Psi\left(\frac{1}{2}+\frac{B_\mathrm{i}}{B}\right)+\frac{1}{2}\ln\frac{B_\mathrm{i}}{B} \\ & +\Psi\left(\frac{1}{2}+\frac{B_\mathrm{i}+B_\mathrm{SO}}{B}\right)-\ln\frac{B_\mathrm{i}+B_\mathrm{SO}}{B} \\ & +\frac{1}{2}\Psi\left(\frac{1}{2}+\frac{B_\mathrm{i}+2B_\mathrm{SO}}{B}\right)-\frac{1}{2}\ln\frac{B_\mathrm{i}+2B_\mathrm{SO}}{B},\end{aligned} \tag{5.1}$$

where Ψ is the digamma function and $B_\mathrm{i,SO}$ are the effective fields related to the inelastic and spin–orbit relaxation lengths, respectively. Figure 5.4a shows $\Delta\sigma$ and the respective quantum correction from the HLN model (black lines). $\Delta\sigma$ displays a local minimum at a field B_min, which indicates the point where weak antilocalization (WAL) is overcome by weak localization (WL). It has been demonstrated that B_min is proportional to the characteristic magnetic field B_SO [142]. Therefore, the gradual shift of B_min to smaller values of B as a function of electrostatic doping indicates a monotonic decrease of the SOC strength. In contrast with previous work [134], no classical component was required to fit the data and the local minima of the data are well captured. The characteristic lengths of inelastic and spin–orbit scattering $l_\mathrm{i,so}$ are related to the effective fields by $B_\mathrm{i,SO} = \hbar/4el^2_\mathrm{i,SO}$ and are shown as a function of applied electrostatic doping in Fig. 5.4b. We find that $l_\mathrm{SO} < l_\mathrm{i}$ throughout the entire range, indicating WAL. Moreover, we observe a relatively small value of l_SO which is constant with electrostatic doping, indicating that SO interactions are strong ($\varepsilon_\mathrm{SO} \approx 4.26\,\mathrm{meV}$ at $0.38\,\mathrm{mS}$), but overall display reduced tunability with respect to the (001)-oriented case. This can be understood by recalling the hallmark feature of this crystallographic direction — the identical projection of all t_{2g} orbitals onto the 2DES plane. The magnitude of B_SO, which is proportional to the out-of-plane component of the orbitals involved in transport [143], is therefore expected to be large and independent of band occupation, in very good agreement with our experimental results.

5.5. CONCLUSION

In summary, we have studied (111)-oriented LAO/STO interfaces where t_{2g} manifold splitting by quantum confinement is absent. We show that transport occurs through electron-like bands and on-site correlations drive an inversion between two sets of t_{2g} sub-bands, each containing a balanced contribution of all three orbital characters. This captures the non-monotonic dependence of R_H on electrostatic doping and rules out the presence of a hole-like band. The results of this work strongly underline the importance of orbital hierarchy and electron-electron interactions in determining the properties of LAO/STO interfaces.

5.6. SUPPLEMENTAL INFORMATION

5.6.1. THEORETICAL MODELING

The (111)-oriented interface features a very different geometry than that of its (001)-oriented counterpart. When the cubic structure with Titanium (Ti) atoms is projected on one plane, three interspersing Ti lattices are found (Ti 1, 2 and 3), as shown in Fig. 5.5, which forms a hexagonal structure. In our modeling, only two layers are considered, assuming the coupling of the third layer to be weak as it is further away from the surface.

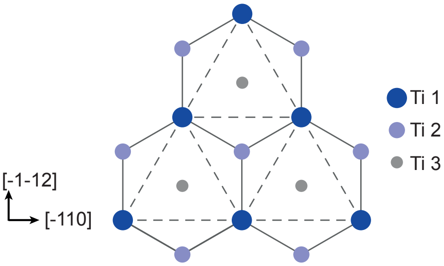

Figure 5.5: Top view of three consecutive Ti^{4+} layers in (111)-oriented STO. The number indicates the distance of the respective atomic layer to the STO surface. For theoretical calculations, only two Ti^{4+} layers are taken in to account.

In a tight-binding formalism, there exist two kinds of hopping for the two layers-inter-layer and intra-layer, the amplitude of which depends on the distance between the concerned atoms. If only intra-layer coupling is added, three bands, one of each t_{2g} orbitals, is observed, 4 times degenerate, twice in spin and twice for each layer. The intra-layer coupling is described by

$$a_{d_{xy}} = -2t_1\cos(\sqrt{3}k_x) \tag{5.2}$$

$$a_{d_{yz}} = -2t_1\cos(-\tfrac{\sqrt{3}}{2}k_x + \tfrac{3}{2}k_y) \tag{5.3}$$

$$a_{d_{xz}} = -2t_1\cos(\tfrac{\sqrt{3}}{2}k_x + \tfrac{3}{2}k_y) \tag{5.4}$$

where $t_1 = 0.05\,\mathrm{eV}$ is the intra-layer hopping amplitude. The inter-layer coupling then splits this manifold into three bonding and three anti-bonding bands, twice degenerate in spin, each. The inter-layer coupling is described by

$$a'_{d_{xy}} = -t_2 - 2t_3\cos(\tfrac{\sqrt{3}}{2}k_x)e^{-\mathrm{I}\frac{3}{2}k_y} \tag{5.5}$$

$$a'_{d_{yz}} = -t_3(1 + e^{\mathrm{I}(\frac{\sqrt{3}}{2}k_x - \frac{3}{2}k_y)}) - t_2 e^{-\mathrm{I}(\frac{\sqrt{3}}{2}k_x + \frac{3}{2}k_y)} \tag{5.6}$$

$$a'_{d_{xz}} = -t_3(1 + e^{-\mathrm{I}(\frac{\sqrt{3}}{2}k_x - \frac{3}{2}k_y)}) - t_2 e^{\mathrm{I}(\frac{\sqrt{3}}{2}k_x - \frac{3}{2}k_y)} \tag{5.7}$$

where $t_3 = 1.6\,\mathrm{eV}$ and $t_2 = 0.07\,\mathrm{eV}$ are first and third nearest neighbour hoppings between layers. Since the 2DES resides on the STO side of the LAO/STO interface, one expects similar tight-binding dispersions for (111)-oriented STO and LAO/STO, allowing us to use photoemission data for the (111) STO surface [144, 145] (this is indeed the case for the (001) orientation [140]). Only the lower energy bonding states are then required which lie close to the Fermi level. An inter-layer electrostatic potential is added to distinguish between the two layers in terms of their distance from the surface, which increases the distance between the bonding and the anti-bonding orbitals without changing their character. Using Dirac's notation, the Hamiltonian H_o in basis of $\{dxy_{1,\sigma}, dyz_{1,\sigma}, dxz_{1,\sigma}, dxy_{2,\sigma}, dyz_{2,\sigma}, dxz_{2,\sigma}\}$ for the two layers and where $1,2$ is the layer index and σ for spin $\uparrow, \downarrow$, is given by

$$H_{o;\sigma} = \sum_{P=(dxy,dyz,dxz)} |d_{P,1,\sigma}, d_{P,2,\sigma}\rangle \mathbf{M} \langle d_{P,2,\sigma}, d_{P,1,\sigma}| \tag{5.8}$$

where $M = \begin{bmatrix} a_P & a_P^{'} \\ a_P^{'*} & b_P \end{bmatrix}$ and $b_P = a_p + \Delta V$, ΔV being the difference of potential between the two layers owing to their different location with respect to the surface.

The next term in the modeling is the trigonal crystal field, the magnitude of which is given by $tf = 10\,\text{meV}$, which arises as a result of the changed (111) symmetry at the surface. This lifts further the degeneracy at Γ and is represented in the $\{d_{xy}, d_{yz}, d_{xz}\}$ basis by $H_{trf} = \begin{bmatrix} 0 & tf & tf \\ tf & 0 & tf \\ tf & tf & 0 \end{bmatrix}$. The trigonal field needs to be added separately to each layer and each spin. Bulk spin–orbit interaction, $H_{so} = \lambda \vec{L}.\vec{S}$, couples the orbital and spin degrees of freedom within each layer and changes the character of a band from pure t_{2g} to a mixture of all three t_{2g} orbitals. It also creates a spin-split off band at Γ.

The final term before the addition of correlations is the modeling of the quantum confinement at the surface of the (111)-oriented interface. Poisson–Schrodinger (P–S) calculations show that the bands introduced above give rise to sub-bands in the quantum well, created by the surface potential, and lying very close to each other. At least, two of these sets of sub-bands lie close to the Fermi level and must be considered in the effective tight-binding modeling. The Hamiltonian of one set of sub-bands can be constructed with $H_{0,\uparrow}, H_{0,\uparrow}, H_{1,so}, H_{2,so}$ and H_{trf} in the basis of $|d_{P,1,\uparrow}, d_{P,2,\uparrow}, d_{P,1,\downarrow}, d_{P,2,\downarrow}\rangle$. A similar matrix exists for the sub-band set two with a shift of the bands by 20 meV as given by P-S calculations. Correlations become important in this modeling as the experimental data shows that the back-gate voltage tunes the number of carriers in the system and they increase with increasing back-gate voltage.

A Hartree-Fock interaction is then added which acts on individual orbitals. From therein stem two contributions to the correlation term, those between like (U) and unlike (U$^{'}$) orbitals, whose product with the band populations of like and unlike orbitals respectively. The band populations take the following form for each orbital $\alpha \in \{xy, yz, xz\}$

$$< N_\alpha >= \sum_i < n_{i\alpha} > \tag{5.9}$$

In Eq. (5.9), $< n_{i\alpha} >$ are the populations of the individual orbitals, i is the band index and the summation is performed for bands with energies less than E_F over all degrees of freedom; $< N_\alpha >$ is the total population of the α orbital. The addition of U and U$^{'}$ gives rise to the following Hartree-Fock contribution

$$\mu_\alpha = U < N_\alpha > + U^{'} \sum_{\gamma \neq \alpha} < N_\gamma > \tag{5.10}$$

In Eq. (5.10) μ_α plays the role of an orbital dependent chemical potential which shifts the bands. As U and $U^{'}$ are added, all orbitals are not equally punished which results in bands being shifted unequally causing band crossings. Before the addition of U and $U^{'}$, the total population, N_0 ,is calculated and this should remain constant even after the addition of U and $U^{'}$. At each iteration of the code, U and $U^{'}$ shift the bands while the Fermi level remains unchanged. The total band population, N_i, is then calculated by summing up individual populations and compared to N_0. The Fermi level is re-adjusted to regain the original total population which again changes the band populations and causes the U and $U^{'}$ to shift the bands at the next iteration. This process is repeated until self-consistency is achieved. Figure 5.6 shows the evolution of the band structure as one goes around the BZ. The filling chosen is such that, after correlations are added, both sub-bands are occupied. The bands are color-labeled according to their orbital character as in the main text. Upon changing the orientation along which one views the band structure, one finds that the lower most occupied band changes character. The integral over the entire BZ yields almost equal population of each orbital character within the manifold of a single sub-band and hence the average of the populations is considered in the calculations for Fig. 5.3.

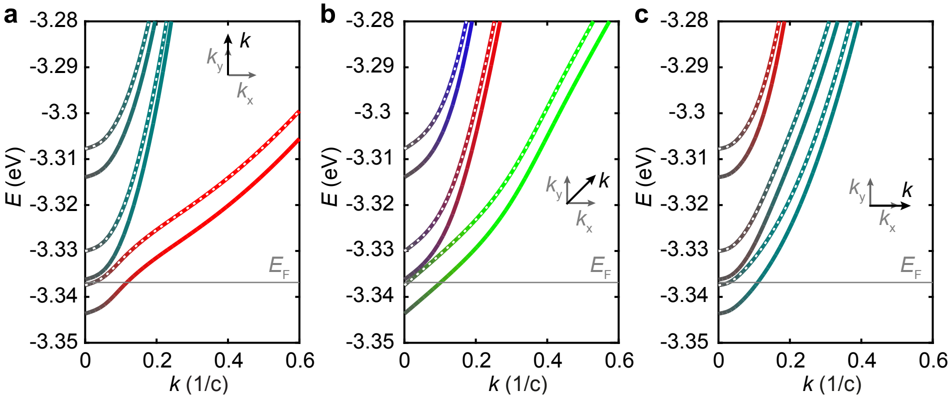

Figure 5.6: Band structure decomposed into the three t_{2g} orbitals of each sub-band in different orientations of the BZ for a filling of the bands where both sub-bands are occupied. Gray line indicates the renormalized Fermi level. (a) With k along the $k_x = 0$ direction. (b) With k along the $k_x = k_y$ direction. (c) With k along the $k_y = 0$ direction.

5.6.2. ANALYSIS OF THE HALL EFFECT AND MAGNETORESISTANCE DATA

The Hall data has been fitted to a two-carrier model given by the expression:

$$\rho_{xy} = \frac{(\sigma_1\mu_1 + \sigma_2\mu_2) + (\sigma_1\mu_2 + \sigma_2\mu_1)\mu_1\mu_2 B^2}{(\sigma_1 + \sigma_2)^2 + (\sigma_1\mu_2 + \sigma_1\mu_1)^2 B^2} B, \tag{5.11}$$

where $\sigma_{1,2}$ are the conductivities and $\mu_{1,2}$ are the mobilities of each one of the bands. The condition $\sigma_{\text{total}} = \sigma_1 + \sigma_2$ is imposed in the fit, since σ_{total} is experimentally known. The experimental data and respective fits are shown in Fig. 5.7.

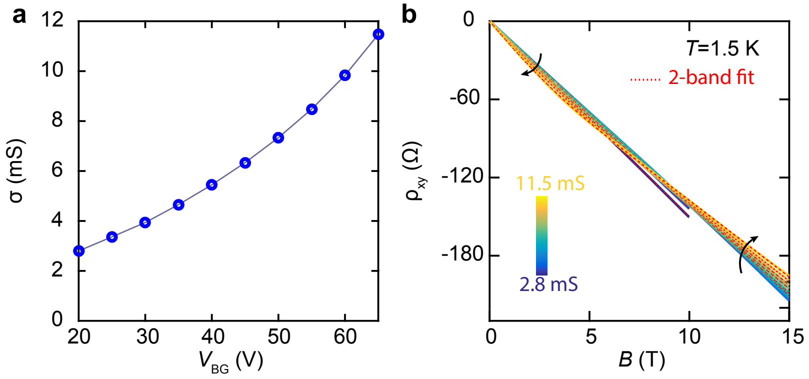

Figure 5.7: (a) Total conductance as a function of applied back-gate voltage. (b) Hall resistance (ρ_{xy}) as a function of applied magnetic field (B) for different levels of electrostatic doping, measured at 1.5 K. Red dashed lines are the fits to a two-carrier model. Black arrows illustrate the trend of the slope at low and high magnetic fields.

The depopulation of the first band can also be qualitatively observed in the Hall traces, where the slope at low field follows the opposite trend of the slope at high field as a function electrostatic doping (denoted by the black arrows in Fig. 5.7). The parameters extracted from the fitting are shown in Fig. 5.2.

Figure 5.8 shows the magnetoresistance (MR) as a function of applied magnetic field for different levels of electrostatic doping, where magnetoresistance is defined as

$$\mathrm{MR} = \frac{\rho(B) - \rho(B=0)}{\rho(B=0)}. \tag{5.12}$$

The red traces indicate the electrostatic doping levels for which the Hall effect becomes non-linear, clearly indicting a two-carrier transport. As mentioned in the main text, these traces display a large classical B^2 component, which increases with electrostatic doping. This classical component can be as large as 30% at $B = 10\,\mathrm{T}$ for the highest doping level.

5.6.3. CARRIER TYPE OF THE 2 BANDS

In the two-band model, the Hall effect saturates towards a linear behaviour at sufficiently high magnetic fields and the sign of R_H provides direct information on the carrier type of the higher-density band. In the case of an electron-like and a hole-like band, the high-field ($B \to \infty$) and low-field ($B \to 0$) limits of R_H are given by

$$\lim_{B\to\infty} R_\mathrm{H} = -\frac{1}{n_e - n_h} \qquad \text{and} \qquad \lim_{B\to 0} R_\mathrm{H} = -\frac{n_e\mu_e^2 - n_h\mu_h^2}{(n_e\mu_e + n_h\mu_h)^2},$$

where $n_{e,h}$ and $\mu_{e,h}$ are the electron and hole carrier densities and mobilities of the two bands, respectively. In our measurements, we access a regime of high conductance and observe a nonlinearity of the Hall data around 5 T, as shown in Fig. 5.9a. From the corresponding derivative (Fig. 5.9b) it can be seen that at higher magnetic fields the Hall

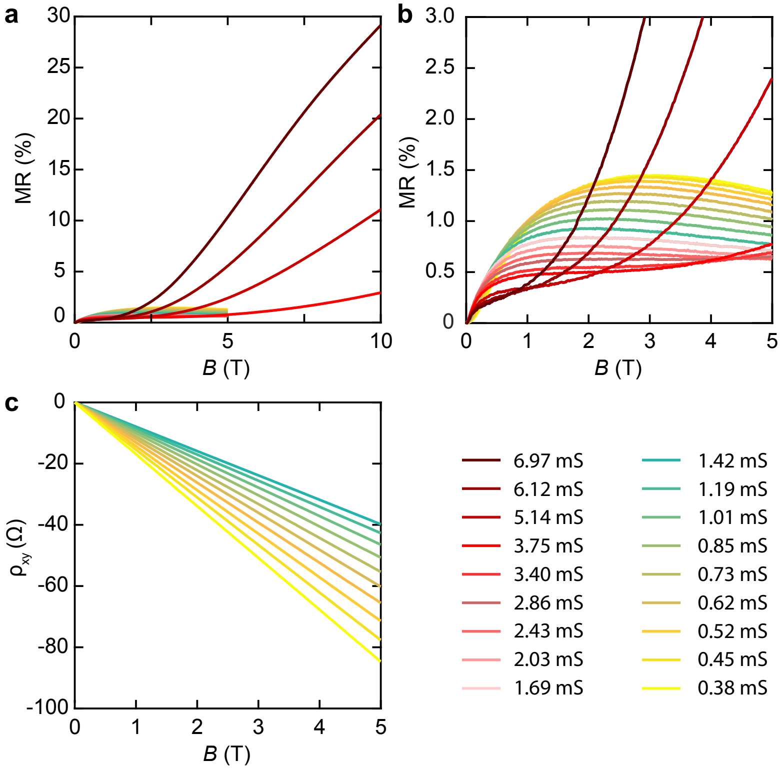

Figure 5.8: Magnetoresistance as a function of applied of applied magnetic field for different levels of electrostatic doping. (a) Entire B-field range. (b) Zoom-in. Red-shaded curves correspond to curves which were not fitted in the MC analysis Fig. 5.4. (c) Hall effect data corresponding to the same levels of electrostatic doping of the MC data of Fig. 5.4.

curve is saturated towards a linear behavior (R_H = constant), indicating that the high-field limit has been reached.

Since $R_\mathrm{H}(B \to \infty) < 0$, we can unequivocally ascertain that the higher-density band is electron-like. From the low-field behavior it can be readily seen that $R_\mathrm{H}(B \to \infty) > R_\mathrm{H}(B \to 0)$. To prove that this is only compatible with two electron-like bands, we will show analytically that our data cannot be described by an electron-hole scenario, irrespective of the mobility values. Since the higher-density band is electron-like, we consider the situation where the second band is hole-like, i.e., $n_e > n_h$, where $n_e = xn_h$ and $x > 1$. Then

$$\lim_{B\to\infty} R_\mathrm{H} = -\frac{1}{xn_h - n_h} = -\frac{1}{n_h}\frac{1}{(x-1)}$$

and

$$\lim_{B\to 0} R_\mathrm{H} = -\frac{xn_h\mu_e^2 - n_h\mu_h^2}{(xn_h\mu_e + n_h\mu_h)^2} = -\frac{1}{n_h}\frac{x\mu_e^2 - \mu_h^2}{(x\mu_e + \mu_h)^2}.$$

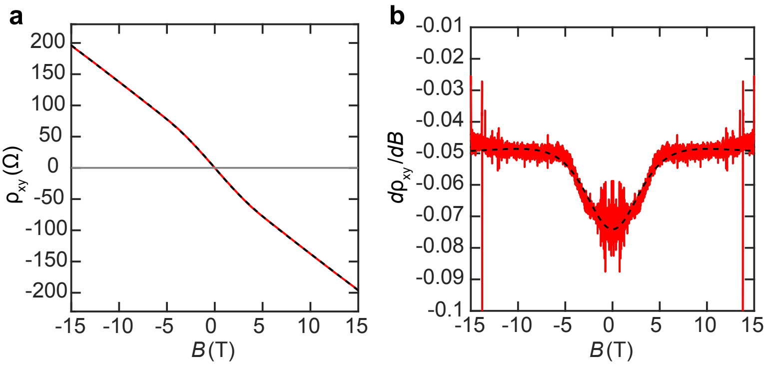

Figure 5.9: (a) Experimental Hall curves for the highest electrostatic doping (red) and respective fit (dashed black). (b) Derivative of the curves presented in (a).

We now check whether this is compatible with our data, where $R_\mathrm{H}(B\to\infty) > R_\mathrm{H}(B\to 0)$.

$$\begin{aligned}
R_\mathrm{H}(B\to\infty) &> R_\mathrm{H}(B\to 0)\\
\frac{x\mu_e^2-\mu_h^2}{(x\mu_e+\mu_h)^2} &> \frac{1}{(x-1)}\\
\frac{x\mu_e^2-\mu_h^2}{x^2\mu_e^2+2x\mu_e\mu_h+\mu_h^2} &> \frac{1}{(x-1)}\\
(x-1)(x\mu_e^2-\mu_h^2) &> x^2\mu_e^2+2x\mu_e\mu_h+\mu_h^2\\
(x^2-x)\mu_e^2-(x-1)\mu_h^2 &> x^2\mu_e^2+2x\mu_e\mu_h++\mu_h^2\\
-x(\mu_e^2+\mu_h^2) &> 2x\mu_e\mu_h\\
-x &> \frac{2x\mu_e\mu_h}{\mu_e^2+\mu_h^2}
\end{aligned}$$

The expression of the right hand side is always positive because x, μ_e and $\mu_h > 0$, and therefore the solution does not exist. This proves that our data cannot be described by an electron-hole scenario, irrespective of the mobility values. Moreover, we show that the data is very well fitted by the two-band model with two electron-like bands (dashed black lines in Figs. 5.9a and 5.9b), which provides the carrier densities and mobilities shown in Figs. 5.2c and 5.2d.

6

MAGNETOTRANSPORT IN FREE-STANDING $SrRuO_3$ NANO-FLAKES

Two-dimensional (2D) materials exhibit a wide range of exceptional electronic and optical properties at nanometer-scale thicknesses. 2D ferromagnets are, however, scarce, and transport in such compounds is largely unexplored. Here, we investigate the properties of free-standing single-crystal $SrRuO_3$ *(SRO), a 4d metallic ferromagnet with strong spin–orbit coupling. Free-standing ultrathin films are obtained by etching of a water-soluble buffer layer and exhibit ferromagnetic behavior down to at least 3 nm thickness. Magnetotransport measurements show that the anomalous Hall conductivity, which is determined by the Berry curvature of the spin–orbit coupled bands, is modified with respect to epitaxial SRO films grown on* $SrTiO_3$*. We show that the data can be well described by a phenomenological model comprising two channels with opposite signs of their anomalous Hall conductivity. The results presented in this chapter pave the way for the integration of complex oxides with van der Waals materials to engineer new phases in hybrid devices.*

The vast family of two-dimensional (2D) materials covers a wide range of electronic properties, ranging from metals such as graphene [146, 147], to small band-gap semiconductors such as the transition metal dichalogenides [148] and black phosphorus [149], and wide band-gap insulators such as hexagonal boron nitride [150]. 2D magnetic materials are however scarce, with insulating ferromagnets such as CrI_3 and $Cr_2Ge_2Te_6$ being discovered only recently [151, 152]. There has been a long-standing effort to obtain 2D ferromagnetic metallic materials, the first (Fe_3GeTe_2) being discovered only this year [153]. A different family of materials that is particularly resourceful is that of the transition metal oxides, where 3D metallic ferromagnets such as $SrRuO_3$ (SRO) and $La_{2/3}Sr_{1/3}MnO_3$ are ubiquitous [154]. SRO is of particular interest due to its strong spin–orbit coupling (SOC), a basic ingredient for spintronics that can give rise to various topological properties. These compounds are typically grown epitaxially by pulsed laser deposition on single-crystal substrates. Recently, Lu et al. demonstrated the release and transfer of epitaxially grown single-crystal layers of these materials, enabling the study of their electronic and magnetic properties in free-standing form [155]. This opens the door for transition metal oxides such as SRO to join the 2D materials family, to be implemented in similar device architectures and to be stacked to create hybrid structures. While free-standing SRO films were previously obtained through chemical etching of the $SrTiO_3$ (STO) substrate with hydrofluoric acid, these studies were limited to films with thicknesses down to 55 nm and no magnetotransport measurements were performed [156, 157]. This is a crucial point, as the modification of the conducting and ferromagnetic properties stemming from strain relaxation and the release process need to be fully addressed to exploit the full potential of free-standing oxide films for nano-electronics. In this chapter, we study the structural and (magneto)transport properties of free-standing single-crystal SRO films and establish a comparison with epitaxial films. We obtain high-quality ferromagnetic films and show that their free-standing nature substantially impacts their anomalous Hall conductivity.

6.1. METHODS AND SAMPLE CHARACTERIZATION

Epitaxial and buffered SRO films are deposited by pulsed laser deposition on commercially available TiO_2-terminated (001)STO substrates. $Sr_3Al_2O_6$ (SAO) films are grown at 800°C in an oxygen pressure of 10^{-6} mbar. SRO films are grown at 550°C in an oxygen pressure of 0.1 mbar. The laser pulses are supplied by a KrF excimer source ($\lambda = 248\,\mathrm{nm}$) with an energy density of $1.2\,\mathrm{J/cm^2}$. The growth was followed by an annealing step in order to remove potential oxygen vacancies. The chamber was filled with 300 mbar of oxygen and the sample temperature was kept at 600°C for 1 hour. The sample was then cooled down to room temperature at a rate of 20°C/min in the same oxygen atmosphere. As shown in the supplementary information, the growth process was monitored in-situ using reflection high-energy electron diffraction (RHEED), which indicates a layer-by-layer growth mode for both SAO and SRO.

To obtain free-standing SRO films, the SAO-buffered samples are immersed in deionized water. After the release, the SRO films are transferred onto Si/SiO_2 or STO substrates following the work of Lu et al. [155]. The SRO films are then contacted by e-beam

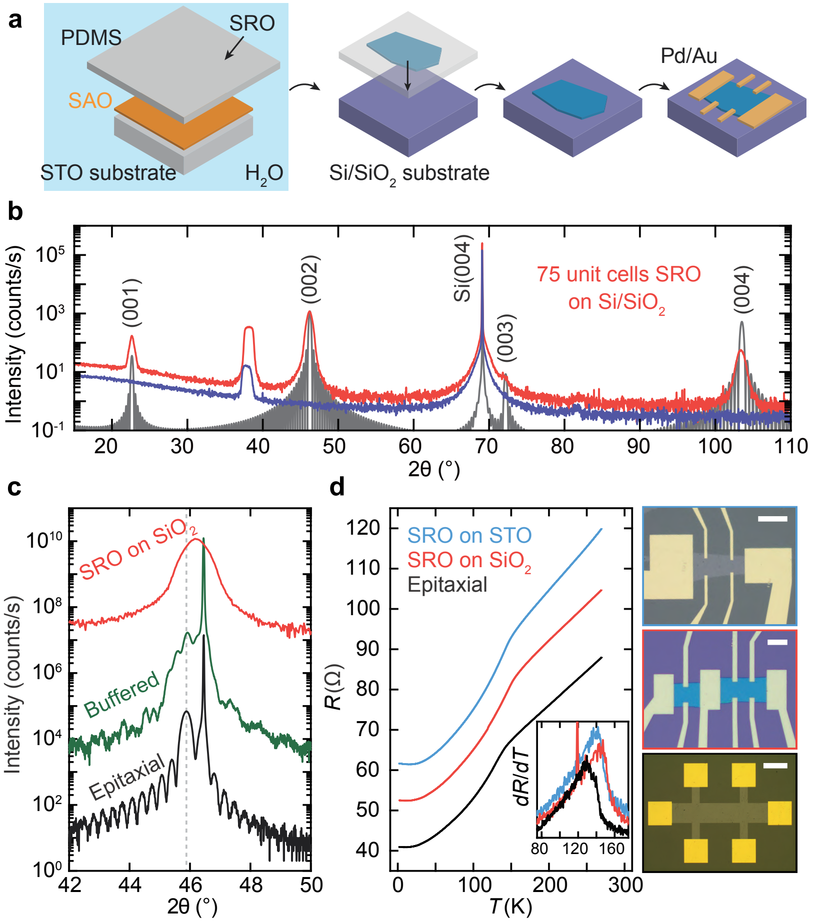

Figure 6.1: (a) Preparation of free-standing SRO films and definition of Hall bars. (b) XRD measurements of free-standing SRO on Si/SiO_2 and a reference Si/SiO_2 substrate. The gray line is a simulation of the diffracted intensity. (c) XRD measurement around the (002) reflection of epitaxial, buffered and free-standing SRO. (d) Resistance (R) as a function of temperature (T) of epitaxial and free-standing SRO films. The inset shows the derivative dR/dT and the shift of T_C. Right: optical images of the measured devices. The scale bars (from top to bottom) are 50, 20, and 300 μm.

lithography and evaporation of Pd/Au electrodes. Appropriate regions of the transferred SRO film are located using e-beam alignment markers pre-patterned on the Si/SiO_2 and STO substrates. Magnetotransport measurements were performed in a He flow cryostat with a 10 T superconducting magnet and a base temperature of 1.5 K. Measurements in current-bias configuration were performed using lock-in amplifiers and custom-made low noise current sources and voltage amplifiers.

The procedure for obtaining free-standing SRO films from the buffered samples is schematically depicted in Fig. 6.1a. First, a polydimethylsiloxane (PDMS) layer is adhered to the SRO surface and the entire stack is immersed in deionized water [155]. After the dissolution of the $Sr_3Al_2O_6$ layer, the SRO is transferred onto other substrates such as Si/SiO_2 or STO using a deterministic dry-transfer technique [158]. Micrometer-sized Hall bars are then defined using e-beam lithography and Ohmic contact is established by deposition of Pd/Au. An X-ray diffraction (XRD) measurement of a 75 u.c. SRO film on a Si/SiO_2 substrate is shown in Fig. 6.1b. As a reference, an XRD measurement of a patterned Si/SiO_2 substrate is included, showing the Si(004) peak at approximately 69° and a peak at 38° arising from evaporated Au. The four orders of diffraction of the SRO film are clearly visible, and their positions match the simulation of the diffracted intensity (gray line) using a c-axis lattice parameter of 3.923 Å and a thickness of 75 unit cells. The thickness is in excellent agreement with the estimate from the RHEED oscillations during the growth (see supplementary information).

Figure 6.1c shows XRD measurements of epitaxial, buffered and free-standing SRO films around the (002) diffraction peak. The epitaxial and buffered films show clear Laue oscillations, indicating that the films are of excellent crystalline quality. Simulations of the diffracted intensity are included in the supplementary information, showing that the film thickness of the SRO layer is 75 u.c. as intended. The c-axis lattice parameter of the epitaxial and buffered SRO films is 3.953 Å, which is expected considering the compressive strain supplied by the STO substrate. The (002) diffraction peak of the free-standing SRO displays a clear shift, consistent with the reduction of the c-axis lattice parameter associated with the release of compressive strain. The lattice parameter of the free-standing film is 3.923 Å, which is consistent with the value for bulk SRO [159].

Next, we investigate the electronic properties of free-standing and epitaxial films. The resistance (R) of epitaxial SRO is known to display a kink at the Curie temperature (T_C), showing linear behavior at $T > T_C$ and Fermi liquid behavior at $T < T_C$ [160]. T_C is further known to depend sensitively on epitaxial strain [156, 161, 162]. $R(T)$ measurements of a patterned epitaxial film and devices fabricated from free-standing films on STO and Si/SiO_2 are shown in Fig. 6.1d. Optical images of the three devices are shown on the right. All devices display metallic behavior and their $R(T)$ curves show a kink, indicating that both epitaxial and free-standing films undergo a transition to a ferromagnetic state. The films have similar resistance values and residual resistance ratios of approximately 2, indicating that the free-standing films are of similar quality as their epitaxial counterpart. The inset shows the derivative ($\mathrm{d}R/\mathrm{d}T$), and most notably T_C is higher for free-standing SRO, which is consistent with the reduced c-axis lattice parameter [156].

6.2. THICKNESS DEPENDENCE

We now turn our attention to the evolution of the transport properties of free-standing SRO films with thickness. $R(T)$ measurements of three free-standing SRO films of different thicknesses on Si/SiO_2 are shown in Fig. 6.2a. The corresponding derivatives are shown in the inset for the 75 and 25 u.c. films. With decreasing thickness, T_C is lowered and the resistance upturn at low temperature becomes more pronounced. The thinnest (12 u.c.) film is no longer metallic and displays semiconducting behavior. A thickness-dependent metal–insulator for epitaxial SRO has previously been measured, showing a gradual decrease of T_C and an enhanced upturn at low temperature due to 2D weak localization [163]. For epitaxial films, the minimum thickness for metallic behav-

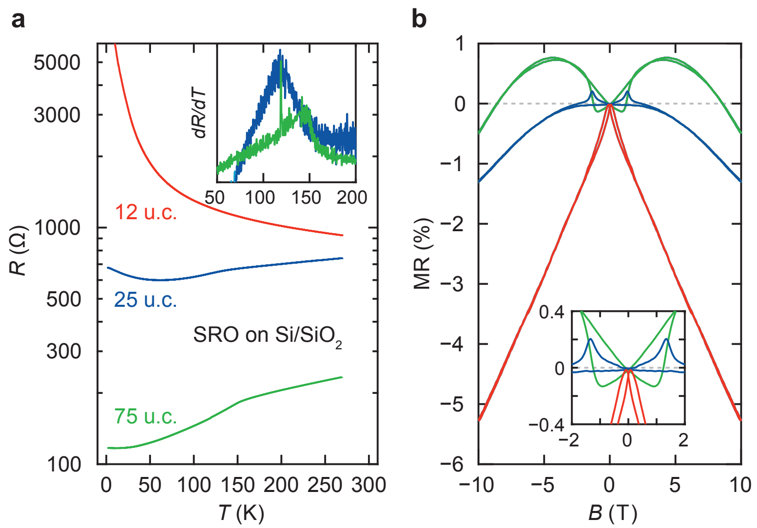

Figure 6.2: (a) Resistance (R) as a function of temperature (T) of free-standing SRO with thicknesses of of 75, 25 and 12 unit cells. The inset shows the derivative dR/dT and the shift of T_C. (b) Out-of-plane magnetoresistance (MR) measured at $T = 20$ K. The inset shows the behavior at low magnetic fields.

ior was found to be 5 unit cells. This critical thickness is hence significantly higher for free-standing films, which could be related to the release of strain, interfacial effects or structural/electronic inhomogeneities within the SRO film.

To study the ferromagnetic properties in more detail, we measured the out-of-plane magnetoresistance (MR) at 20 K (see Fig. 6.2b). The measurements show a “butterfly-loop”, characteristic of ferromagnets. The measurement of the 12 u.c. thick film still displays a clear resistance change at the coercive field (B_c see inset), indicating that, despite the loss of metallicity, the ultrathin free-standing SRO film is still in a ferromagnetic state.

6.3. FREE-STANDING VERSUS EPITAXIAL

A characteristic feature of SRO is its anomalous Hall effect (AHE), which is proportional to the out-of-plane component of the magnetization. As a consequence, the total Hall resistance is given by $R_{xy} = R^{\mathrm{o}}_{xy} + R^{\mathrm{AH}}_{xy}$, where R^{o}_{xy} and R^{AH}_{xy} are the ordinary and anomalous Hall components, respectively. It is well established that both intrinsic deflection and extrinsic sources of scattering can contribute to R^{AH}_{xy} [164]. For SRO, it is generally accepted that the intrinsic mechanism is responsible for its AHE, as its temperature dependence is well reproduced by first-principles calculations and reflects the exchange splitting proportional to the temperature-dependent magnetization [165]. Having established that there is a change in the magnetic anisotropy of the free-standing film, it is expected that this will also impact the AHE. To investigate this, we compare the Hall effect of a free-standing (top) and epitaxial (bottom) SRO film of 75 u.c. in Fig. 6.3a. The curves are offset horizontally for clarity. On first inspection, the curves appear strikingly different. The epitaxial film develops a positive AHE below T_C, after which R^{AH}_{xy} changes

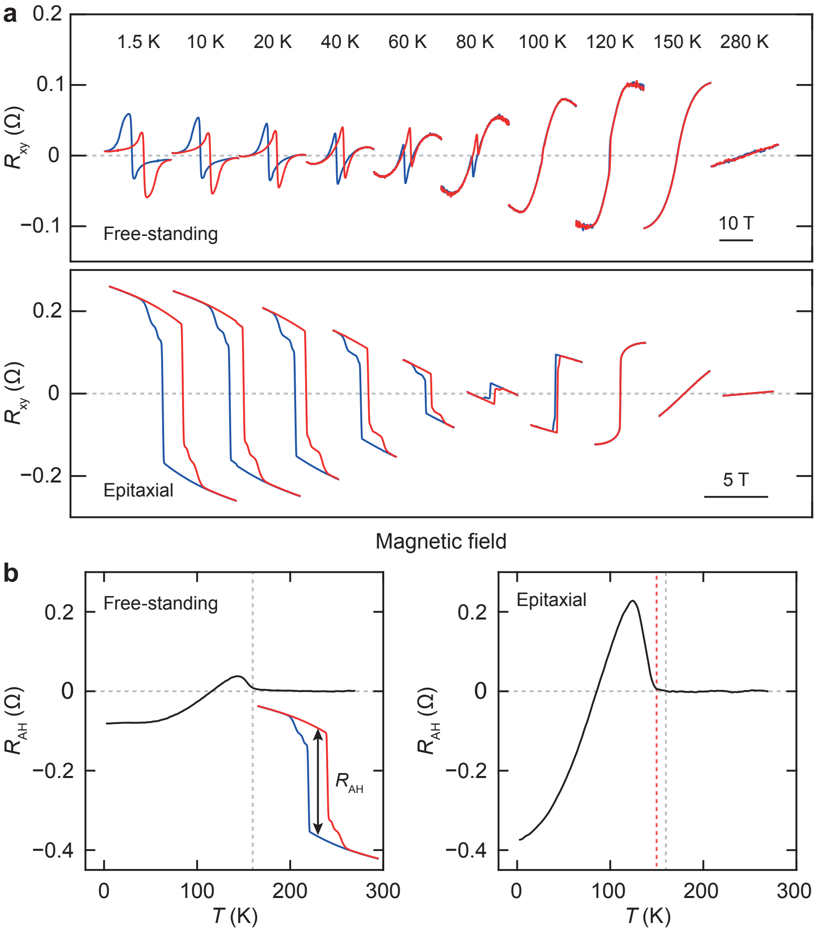

Figure 6.3: (a) Hall effect measured at different temperatures for free-standing (top) versus epitaxial (bottom) SRO films. The curves are offset horizontally. (b) Anomalous Hall resistance (R_{AH}) versus temperature (T) for free-standing (left) versus epitaxial (right) SRO films.

sign and increases in magnitude at low temperatures. The sharp switching at B_{c}, which coincides with the magnetization reversal, is followed by an additional tail which is likely due to pinned sites that align with the field at slightly higher values. The free-standing film also develops a positive AHE below T_{C}, which then changes sign, but additional features appear above B_{c}. Furthermore, the AH loops only close at 10 T, while the loops of the epitaxial film already close at approximately 2 T.

To continuously monitor the magnitude of R_{xy}^{AH} at zero field (defined as R_{AH}), we measure the Hall resistance while cooling down and applying a field of ±50 mT. Taking the difference between the two $R_{xy}(T)$ curves removes the longitudinal component and yields the height of the loop at $B = 0$ T. The contribution from the ordinary Hall component is negligible. The resulting R_{AH} is shown in Fig. 6.3b for the free-standing (top) and epitaxial (bottom) films. While the AHE in Fig. 6.3a appeared to be very different, the $R_{\mathrm{AH}}(T)$ curves are similar, apart from a factor 4 difference in magnitude. The behavior, including the sign change below T_{C}, can also be identified from the curves in Fig. 6.3a and is characteristic for epitaxial SRO [165].

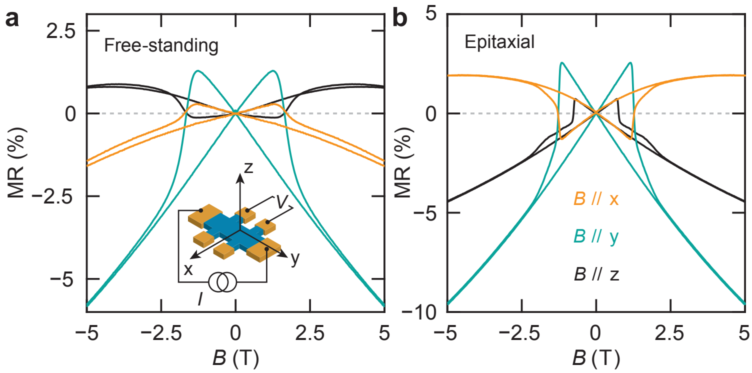

Figure 6.4: Magnetoresistance (MR) measured along the axes defined in the schematic (inset bottom panel) for (a) free-standing and (b) epitaxial SRO films.

We now investigate the magnetic anisotropy by measuring the MR when the magnetic field (B) is applied along x, y, and z, as defined in the insets of Fig. 6.4. For the free-standing film, the coercive fields along all axes are equal, while the coercive field of the epitaxial film is smaller for $B \parallel z$. This indicates that the magnetization is predominantly oriented along z for the epitaxial film, while for the free-standing film it is oriented more in-plane. This is consistent with previous reports, where the compressive strain supplied by the STO substrate results in a more out-of-plane magnetization [166]. In addition, the change in resistance at B_{c} is more gradual for the free-standing film, which can indicate a different switching mechanism or the presence of a magnetic multidomain state [167].

6.4. PHENOMENOLOGICAL TWO-CHANNEL MODEL

The peaks close to B_{c} have also been observed in SRO-based epitaxial heterostructures and are usually interpreted as a topological Hall effect due to skyrmions [168–170]. In Fig. 6.5a, we show that the AH loops of the free-standing film can be fitted to a phenomenological model that comprises two channels with contributions of opposite signs. The curves are fitted to $R^{\mathrm{AH}}_{xy} = R^{\mathrm{AH}}_{xy,\mathrm{I}} \tanh(\omega_{\mathrm{I}}(B - B_{\mathrm{c,I}})) + R^{\mathrm{AH}}_{xy,\mathrm{II}} \tanh(\omega_{\mathrm{II}}(B - B_{\mathrm{c,II}}))$, where ω is a parameter describing the slope at B_{c}. We note that the ordinary Hall component is small compared to the anomalous components and does not impact the fit substantially. The individual AH components, that together constitute the total AHE, are shown in Fig. 6.5b. It is immediately apparent that their behavior is very different: the negative AHE (dark blue curve) displays a sharp switching behavior, while the positive contribution (light blue) switches more gradually. This indicates that the free-standing SRO film comprises two, very different magnetic phases. The parameters extracted from the AH components are shown in Figs. 6.5c to 6.5e. From Fig. 6.5c, we see that the positive contribution has a larger B_{c} at 1.5 K but decreases more rapidly with increasing temperature,

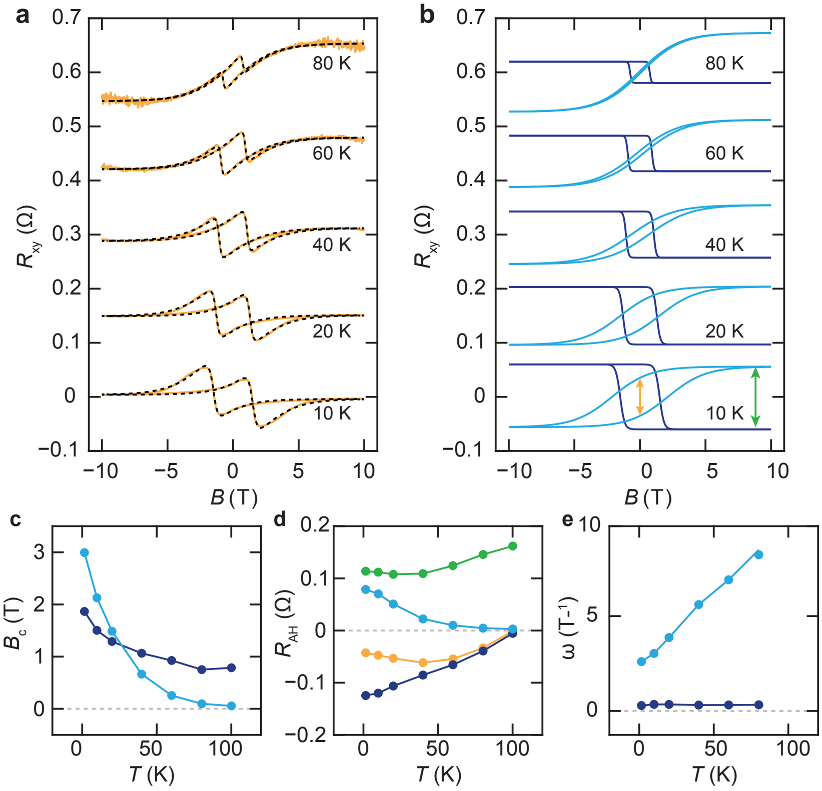

Figure 6.5: (a) Hall resistance (R_{xy}) measured at different temperatures. The black dashed lines are fits to the data and the curves are offset vertically. (b) The two anomalous Hall components that add up to the total R_{xy} curves in (a). (c) Extracted coercive fields (B_c) and (d) loop heights R^0_{AH} as function of temperature (T). (e) Extracted slope (ω) as function of T.

going to zero at approximately 100 K. B_c of the negative contribution is still around 1 T at 100 K. Comparing the magnitude of B_c and the switching behavior to the epitaxial film, we can identify the dark blue AH component of the free-standing case as the AHE of the epitaxial SRO. A possible origin for the second magnetic phase can be related to the interface with SiO_2, due to temperature-dependent strain induced by van der Waals forces at the film/substrate interface. To test this hypothesis, we investigated the temperature dependence of the AHE of a free-standing SRO film of the same thickness on STO (see supplementary material). The observed behaviour is qualitatively the same as the one on SiO_2, indicating that the second magnetic phase has a different origin, for example charge inhomogeneity due to interdiffusion across the SAO/SRO interface.

$R_{AH}(T)$ of the two AH components and their sum are shown in Fig. 6.5d. At low temperature, the contribution of the positive component reduces R_{AH} by a factor of 2–3, which explains both the different magnitude compared to the epitaxial SRO and the saturation at low temperature. Looking back at Fig. 6.5b, we note that it is important to distinguish between the magnitude of the AHE at $B = 0$ and the magnitude at saturation. While $R_{AH}(B = 0)$ is zero at 100 K, the magnitude at saturation in fact increases with increasing temperature, as shown in Fig. 6.5d (green points). This indicates that this magnetic phase does not disappear at 100 K, but shows more paramagnetic behavior.

6.5. CONCLUSION

In summary, we have realized free-standing ultrathin SRO films and confirmed their high crystalline quality. We have demonstrated that the AHE of free-standing SRO is strikingly different from its epitaxial counterpart on STO. Interestingly, the AHE of free-standing SRO is well described by a phenomenological model comprising two channels with contributions of opposite signs, indicating the presence of two magnetically distinct phases. We tentatively attribute this to charge inhomogeneity originating from the release process. The ability to obtain free-standing SRO films provides exciting prospects for continuous variation of strain and engineering desired interfacial effects.

6.6. SUPPLEMENTAL INFORMATION

6.6.1. GROWTH AND STRUCTURAL CHARACTERIZATION

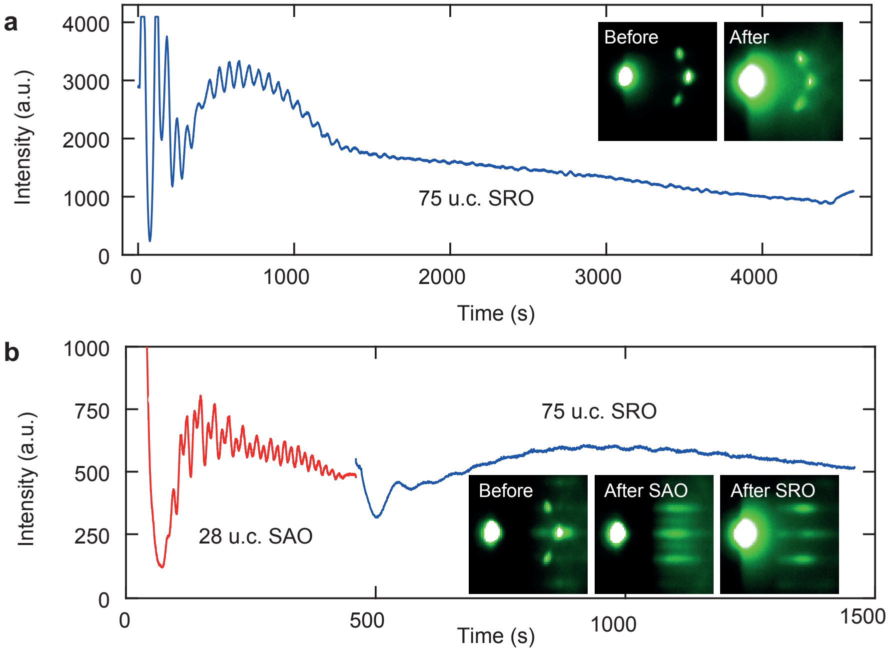

Figure 6.6: (a) RHEED intensity oscillations of the specular spot during the growth of epitaxial SRO. Inset: diffraction patterns before and after growth of epitaxial SRO. (b) RHEED intensity oscillations of the specular spot during the growth of SAO-buffered SRO. Inset: diffraction patterns before and after growth of SAO and SRO.

The RHEED intensity the specular spot for epitaxial and SAO-buffered SRO is shown in Fig. 6.6. For the SAO-buffered SRO film, the growth of SAO is displayed in its entirety, while for the SRO film only the first 17 oscillations are shown. In both samples, the growth rate of SRO is determined from the first 15 oscillations, which are clearly defined. This allows for extrapolation of the film thickness at the end of the growth, when the RHEED oscillations are no longer discernible.

Figure 6.7 shows two X-ray reflectivity measurements of a 75 u.c. SRO films, the first grown epitaxially on STO and the second with an intermediate SAO buffer layer. Superimposed to the data, we show the simulated diffracted intensity for the film thicknesses estimated from the RHEED oscillations. In both cases, the good agreement between the X-ray data and the simulations corroborates that the film thickness estimated from the RHEED oscillations are accurate.

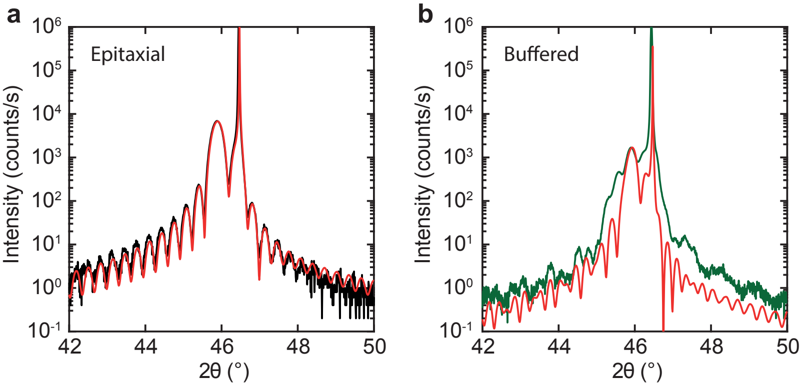

Figure 6.7: XRD measurements around the (002) reflection of (a) SRO and (b) SAO-buffered SRO grown epitaxially on STO. The red lines represent simulations of the diffracted intensity.

Figure 6.8 a shows a complete flowchart of the various steps involved in the fabrication of the devices discussed in the main text. The light blue arrow shows the fabrication process of the epitaxial SRO device, and the dark blue arrow pertains the more convoluted fabrication process of free-standing SRO devices. Bold black arrows indicate optical images of the free-standing device at different stages of the device fabrication.

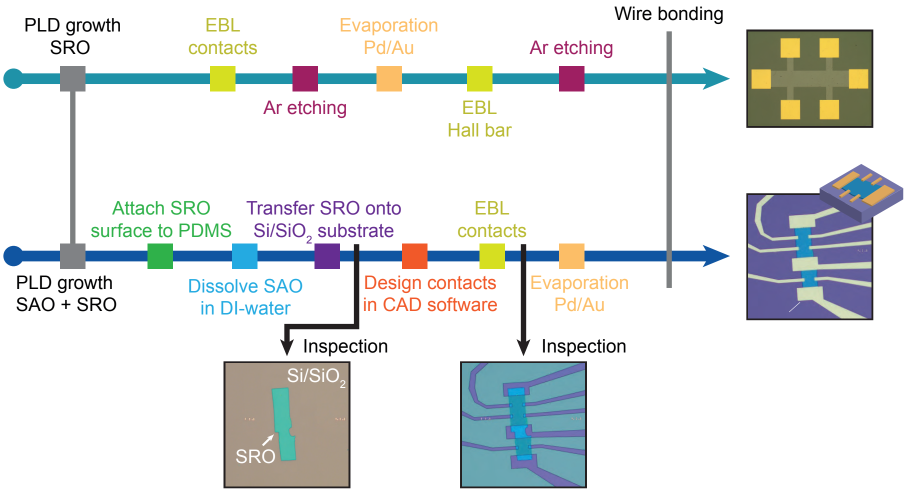

Figure 6.8: Hall bar fabrication procedure for epitaxial (top) and free-standing (bottom) SRO films.

7

CONCLUSION

> *It is strange that only extraordinary men make the discoveries, which later appear so easy and simple.*
>
> G. C. Lichtenberg

Since Ohtomo and Hwang's seminal discovery of conductivity at the interface between LAO and STO [16], numerous research efforts — both experimental and theoretical — have been devoted to the field of oxide interfaces. In this thesis, we experimentally investigated some fundamental aspects of its complex behavior.

From an extensive list of exotic properties, one of the most surprising experimental observations is the peculiar anisotropy of magnetotransport under externally applied magnetic fields of large magnitude [39, 55–57]. When the field is applied in the plane of the 2DES, a large negative magnetoresistance is observed, showing a dramatic bell-shaped drop in resistance with respect to its zero-field value. In Chapter 2 we demonstrate that spin–orbit coupling and scattering from finite-range impurities can explain the giant in-plane magnetoresistance observed at the LAO/STO interface, as well as the temperature and electron density dependence. Since the onset of superconductivity occurs in the same electrostatic doping range, it would be interesting to investigate whether spin–orbit coupling plays a dominant role in that transition as well.

Over the course of this thesis we have showcased the unique advantages of complex oxide interfaces as a platform for exploring highly-varied physical phenomena. Within the same interface, one may simultaneously find a rich set of fundamental physical phenomena. Faced with this complex, disordered landscape of coexisting phenomena, we used nanoscale probes to circumvent the elements that currently evade our control. In Chapter 3 we employed a single-step lithographic process to realize gate-tunable Josephson junctions through a combination of lateral confinement and local side gating. This technique is particularly advantageous because the interfacial properties of the 2DES appear to be very sensitive to the LAO top surface. Polar adsorbates, for instance, cause a change in the carrier density [90], and metallic capping has even been used to trigger conductivity in nominally insulating 1 u.c. thick LAO/STO interfaces [91].

Recent works have demonstrated that a 2DES can also be hosted at LAO/STO interfaces oriented along different crystallographic directions [109], opening novel possibilities for the realization of distinct electronic structures. In this thesis, we have set out to explore the properties of (111)-oriented LAO/STO interfaces, both in the superconducting (Chapter 4) and normal-state (Chapter 5) regimes. We find that the new orbital hierarchy established in this direction of confinement has deep implications for electronic transport. In particular, the role of electronic correlations is enhanced due to the absence of a Lifshitz point and it plays a pivotal role in explaining the evolution of magnetotransport with electrostatic doping.

Finally, in Chapter 6 we make use of an innovative technique to obtain free-standing oxide films by etching a water-soluble sacrificial SAO layer [155]. From a technological perspective, this is perhaps the most exciting chapter, paving the way for the integration of complex oxides with van der Waals materials to engineer new phases in hybrid devices. We study the structural and (magneto)transport properties of free-standing single-crystal SRO films and establish a comparison with their epitaxial counterparts. This allows us to address changes in their electronic and magnetic properties stemming from strain relaxation and the release process. This is essential to fully exploit the potential of free-standing oxide films for nano-electronics.

7.1. FUTURE PERSPECTIVES

The coexistence of different phenomena naturally occurring at LAO/STO interfaces can be exploited to realize novel nanoscale systems that are presently too difficult to intentionally engineer but can be readily studied with existing probes such as the new generation of nanoscale scanning SQUIDs. One such interesting arrangement is the investigation of one-dimensional conducting channels at domain walls. Figure 7.1a shows a device designed for this purpose. A 50 μm-wide LAO/STO channel is crossed by voltage probes with separations of $1, 2, 4, 8, ..., 128\,\mu$m. The fortuitous location of a domain wall across the channel as shown in Fig. 7.1b provides the ideal experimental setup for such an investigation. The usage of etch-and-filled Ti/Au voltage probes allows for an extra tuning knob to be used, namely electrostatic field-effect via a back gate. This might allow for the on-demand placement of domain walls inside or outside the LAO/STO channel, without the possibility of measurements being hampered by voltage probes turning insulating first.

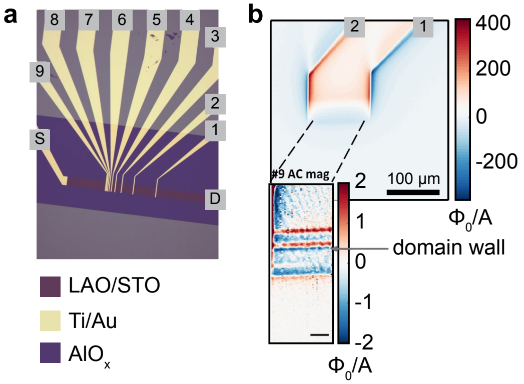

Figure 7.1: (a) Optical image of an LAO/STO channel with etch-and-filled Ti/Au voltage probes with separations of $1, 2, 4, 8, ..., 128\,\mu$m. (b) Magnetic flux image from current flowing in the region where the voltage probes are separated by 128 μm. Inset: zoom-in showing a domain wall spanning the distance between the voltage probes.

Nanoscale scanning SQUIDs might also shine light on the depletion/accumulation process by electrostatic field effect via top gates. Figure 7.2a shows a schematic representation of an LAO/STO channel crossed by an Au top gate. Surprisingly, in this configuration the spatial changes to the current flow induced by applying a voltage to the top gate are not limited to the region underneath the gate. Vast and, more surprisingly, irreversible changes were detected in the vicinity of domain walls. The magnetic flux images in Fig. 7.2b shows that the current flow is rather homogeneous throughout the channel in the as-cooled state, with weak modulations of the current flow at domain walls. By contrast, when the top gate is swept to -4 V and back to 0 V, the current flow is squeezed into a narrow path. By taking a close look at Fig. 7.2c, we can see that this dramatic change happens at the location of a domain wall. This observation showcases the importance of addressing and understanding electronic transport at domain walls before complex and reliable nanoscale circuits at oxide interfaces can be designed.

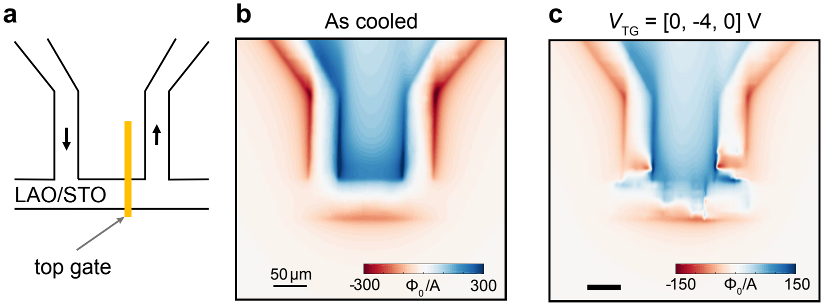

Figure 7.2: (a) Schematic representation of an LAO/STO channel crossed by a top gate. Arrows indicate the direction of the current flow. (b) Magnetic flux image from current flowing in the LAO/STO channel as cooled. (c) Magnetic flux image from current flowing in the LAO/STO channel after the top gate is swept to −4 V and back to 0 V.

REFERENCES

[1] C. Tudge, *Neanderthals, bandits and farmers: How agriculture really began* (CT: Yale University Press, 1998).

[2] L. T. C. Rolt, *Isambard Kingdom Brunel* (Longmans, Green & Co., 1957).

[3] A. Wilson, *The living rock: The story of metals since earliest times and their impact on civilization* (Woodhead Publishing, 1994).

[4] J. J. Thomson, *XL. Cathode rays,* The London, Edinburgh, and Dublin Philosophical Magazine and Journal of Science **44**, 293 (1897).

[5] L. D. Forest, *Space telegraphy,* U.S. Patent 8,795,32A (1907).

[6] J. Bardeen and W. Brattain, *Three electrode circuit element utilizing semiconductive materials,* U.S. Patent 2,524,035 (1948).

[7] W. Shockley, *Circuit element utilizing semiconductive material,* U.S. Patent 2,569,347 (1948).

[8] T. N. Theis and P. M. Solomon, *It's time to reinvent the transistor!* Science **327**, 1600 (2010).

[9] H. Kroemer, *Nobel lecture: Quasielectric fields and band offsets: teaching electrons new tricks,* Reviews of Modern Physics **73**, 783 (2001).

[10] C. N. R. Rao and A. K. Cheetham, *Giant magnetoresistance in transition metal oxides,* Science **272**, 369 (1996).

[11] S. Jin, T. H. Tiefel, M. McCormack, R. A. Fastnacht, R. Ramesh, and L. H. Chen, *Thousandfold change in resistivity in magnetoresistive La-Ca-Mn-O films,* Science **264**, 413 (1994).

[12] N. W. Ashcroft and N. D. Mermin, *Solid state physics* (Holt, Rinehart and Winston, 1976).

[13] A. Liebsch, *Surface versus bulk Coulomb correlations in photoemission spectra of* $SrVO_3$ *and* $CaVO_3$*,* Physical Review Letters **90**, 096401 (2003).

[14] H. Y. Hwang, Y. Iwasa, M. Kawasaki, B. Keimer, N. Nagaosa, and Y. Tokura, *Emergent phenomena at oxide interfaces,* Nature Materials **11**, 103 (2012).

[15] A. D. Caviglia, S. Gariglio, N. Reyren, D. Jaccard, T. Schneider, M. Gabay, S. Thiel, G. Hammerl, J. Mannhart, and J.-M. Triscone, *Electric field control of the* $LaAlO_3/SrTiO_3$ *interface ground state,* Nature **456**, 624 (2008).

[16] A. Ohtomo and H. Y. Hwang, *A high-mobility electron gas at the* $LaAlO_3/SrTiO_3$ *heterointerface,* Nature **427**, 423 (2004).

[17] G. Herranz, M. Basletić, M. Bibes, C. Carrétéro, E. Tafra, E. Jacquet, K. Bouzehouane, C. Deranlot, A. Hamzić, J.-M. Broto, A. Barthélémy, and A. Fert, *High mobility in $LaAlO_3$/$SrTiO_3$ heterostructures: Origin, dimensionality, and perspectives,* Physical Review Letters **98**, 216803 (2007).

[18] K. Song, S. Ryu, H. Lee, T. R. Paudel, C. T. Koch, B. Park, J. K. Lee, S.-Y. Choi, Y.-M. Kim, J. C. Kim, H. Y. Jeong, M. S. Rzchowski, E. Y. Tsymbal, C.-B. Eom, and S. H. Oh, *Direct imaging of the electron liquid at oxide interfaces,* Nature Nanotechnology **13**, 198 (2018).

[19] H. P. R. Frederikse and W. R. Hosler, *Hall mobility in $SrTiO_3$,* Physical Review **161**, 822 (1967).

[20] A. Fête, C. Cancellieri, D. Li, D. Stornaiuolo, A. D. Caviglia, S. Gariglio, and J.-M. Triscone, *Growth-induced electron mobility enhancement at the $LaAlO_3$/$SrTiO_3$ interface,* Applied Physics Letters **106**, 051604 (2015).

[21] Y. Xie, Y. Bell, C.and Hikita, S. Harashima, and H. Y. Hwang, *Enhancing electron mobility at the $LaAlO_3$/$SrTiO_3$ interface by surface control,* Advanced Materials **25**, 4735 (2013).

[22] M. Huijben, G. Koster, M. K. Kruize, S. Wenderich, J. Verbeeck, S. Bals, E. Slooten, B. Shi, H. J. A. Molegraaf, J. E. Kleibeuker, S. van Aert, J. B. Goedkoop, A. Brinkman, D. H. A. Blank, M. S. Golden, G. van Tendeloo, H. Hilgenkamp, and G. Rijnders, *Defect engineering in oxide heterostructures by enhanced oxygen surface exchange,* Advanced Functional Materials **23**, 5240 (2013).

[23] Y. Z. Chen, F. Trier, T. Wijnands, R. J. Green, N. Gauquelin, R. Egoavil, D. V. Christensen, G. Koster, M. Huijben, N. Bovet, S. Macke, F. He, R. Sutarto, N. H. Andersen, J. A. Sulpizio, M. Honig, G. E. D. K. Prawiroatmodjo, T. S. Jespersen, S. Linderoth, S. Ilani, J. Verbeeck, G. Van Tendeloo, G. Rijnders, G. A. Sawatzky, and N. Pryds, *Extreme mobility enhancement of two-dimensional electron gases at oxide interfaces by charge-transfer-induced modulation doping,* Nature Materials **14**, 801 (2015).

[24] N. Nakagawa, A. Y. Hwang, and A. D. Muller, *Why some interfaces cannot be sharp,* Nature Materials **5**, 204 (2006).

[25] M. B. Shalom, A. Ron, A. Palevski, and Y. Dagan, *Shubnikov–de haas oscillations in $SrTiO_3$/$LaAlO_3$ interface,* Physical Review Letters **105**, 206401 (2010).

[26] A. D. Caviglia, S. Gariglio, C. Cancellieri, B. Sacepe, A. Fete, N. Reyren, M. Gabay, A. F. Morpurgo, and J.-M. Triscone, *Two-dimensional quantum oscillations of the conductance at $LaAlO_3$/$SrTiO_3$ interfaces,* Physical Review Letters **105**, 236802 (2010).

[27] Z. S. Popović, S. Satpathy, and R. M. Martin, *Origin of the two-dimensional electron gas carrier density at the $LaAlO_3$ on $SrTiO_3$ interface,* Physical Review Letters **101**, 256801 (2008).

[28] S. Gariglio, A. Fête, and J.-M. Triscone, *Electron confinement at the $LaAlO_3$/$SrTiO_3$ interface,* Journal of Physics: Condensed Matter **27**, 283201 (2015).

[29] P. R. Willmott, S. A. Pauli, R. Herger, C. M. Schlepütz, D. Martoccia, B. D. Patterson, B. Delley, R. Clarke, D. Kumah, C. Cionca, and Y. Yacoby, *Structural basis for the conducting interface between* $LaAlO_3$ *and* $SrTiO_3$, Physical Review Letters **99**, 155502 (2007).

[30] A. Kalabukhov, R. Gunnarsson, J. Börjesson, E. Olsson, T. Claeson, and D. Winkler, *Effect of oxygen vacancies in the* $SrTiO_3$ *substrate on the electrical properties of the* $LaAlO_3/SrTiO_3$ *interface,* Physical Review B **75**, 121404 (2007).

[31] W. Siemons, G. Koster, H. Yamamoto, W. A. Harrison, G. Lucovsky, T. H. Geballe, D. H. A. Blank, and M. R. Beasley, *Origin of charge density at* $LaAlO_3$ *on* $SrTiO_3$ *heterointerfaces: Possibility of intrinsic doping,* Physical Review Letters **98**, 196802 (2007).

[32] L. Yu and A. Zunger, *A polarity-induced defect mechanism for conductivity and magnetism at polarnonpolar oxide interfaces,* Nature Communications **5**, 5118 (2014).

[33] Z. Zhong, P. X. Xu, and P. J. Kelly, *Polarity-induced oxygen vacancies at* $LaAlO_3/SrTiO_3$ *interfaces,* Physical Review B **82**, 165127 (2010).

[34] Y. Li, S. N. Phattalung, S. Limpijumnong, J. Kim, and J. Yu, *Formation of oxygen vacancies and charge carriers induced in the* n*-type interface of a* $LaAlO_3$ *overlayer on* $SrTiO_3$*(001),* Physical Review B **84**, 245307 (2011).

[35] N. C. Bristowe, P. B. Littlewood, and E. Artacho, *Surface defects and conduction in polar oxide heterostructures,* Physical Review B **83**, 205405 (2011).

[36] N. Reyren, S. Thiel, A. D. Caviglia, L. Fitting Kourkoutis, G. Hammerl, C. Richter, C. W. Schneider, T. Kopp, A.-S. Rüetschi, D. Jaccard, M. Gabay, D. A. Muller, J.-M. Triscone, and J. Mannhart, *Superconducting interfaces between insulating oxides,* Science **317**, 1196 (2007).

[37] M. Salluzzo, J. Cezar, N. Brookes, V. Bisogni, G. De Luca, C. Richter, S. Thiel, J. Mannhart, M. Huijben, A. Brinkman, G. Rijnders, and G. Ghiringhelli, *Orbital reconstruction and the two-dimensional electron gas at the* $LaAlO_3/SrTiO_3$ *interface,* Physical Review Letters **102**, 166804 (2009).

[38] P. Delugas, A. Filippetti, V. Fiorentini, D. I. Bilc, D. Fontaine, and P. Ghosez, *Spontaneous 2-dimensional carrier confinement at the* n*-type* $SrTiO_3/LaAlO_3$ *interface,* Physical Review Letters **106**, 166807 (2011).

[39] A. Joshua, S. Pecker, J. Ruhman, E. Altman, and S. Ilani, *A universal critical density underlying the physics of electrons at the* $LaAlO_3/SrTiO_3$ *interface,* Nature Communications **3**, 1129 (2012).

[40] J. Biscaras, N. Bergeal, S. Hurand, C. Grossetête, A. Rastogi, R. C. Budhani, D. LeBoeuf, C. Proust, and J. Lesueur, *Two-dimensional superconducting phase in* $LaTiO_3/SrTiO_3$ *heterostructures induced by high-mobility carrier doping,* Physical Review Letters **108**, 247004 (2012).

[41] A. E. M. Smink, J. C. De Boer, M. P. Stehno, A. Brinkman, W. G. Van Der Wiel, and

H. Hilgenkamp, *Gate-tunable band structure of the $LaAlO_3$-$SrTiO_3$ interface,* Physical Review Letters **118**, 106401 (2017).

[42] M. Diez, A. M. R. V. L. Monteiro, G. Mattoni, E. Cobanera, T. Hyart, E. Mulazimoglu, N. Bovenzi, C. W. J. Beenakker, and A. D. Caviglia, *Giant negative magnetoresistance driven by spin–orbit coupling at the $LaAlO_3$/$SrTiO_3$ interface,* Physical Review Letters **115**, 016803 (2015).

[43] W. Niu, Y. Zhang, Y. Gan, D. V. Christensen, M. V. Soosten, E. J. Garcia-Suarez, A. Riisager, X. Wang, Y. Xu, R. Zhang, N. Pryds, and Y. Chen, *Giant tunability of the two-dimensional electron gas at the interface of γ-Al_2O_3/$SrTiO_3$,* Nano Letters **17**, 6878 (2017).

[44] C. Cancellieri, M. L. Reinle-Schmitt, M. Kobayashi, V. N. Strocov, P. R. Willmott, D. Fontaine, P. Ghosez, A. Filippetti, P. Delugas, and V. Fiorentini, *Doping-dependent band structure of $LaAlO_3$/$SrTiO_3$ interfaces by soft X-ray polarization-controlled resonant angle-resolved photoemission,* Physical Review B **89**, 121412 (2014).

[45] G. Khalsa and A. H. MacDonald, *Theory of the $SrTiO_3$ surface state two-dimensional electron gas,* Physical Review B **86**, 125121 (2012).

[46] L. W. van Heeringen, G. A. de Wijs, A. McCollam, J. C. Maan, and A. Fasolino, *$k{\cdot}p$ subband structure of the $LaAlO_3$/$SrTiO_3$ interface,* Physical Review B **88**, 205140 (2013).

[47] A. D. Caviglia, M. Gabay, S. Gariglio, N. Reyren, C. Cancellieri, and J.-M. Triscone, *Tunable Rashba spin–orbit interaction at oxide interfaces,* Physical Review Letters **104**, 126803 (2010).

[48] M. B. Shalom, M. Sachs, D. Rakhmilevitch, A. Palevski, and Y. Dagan, *Tuning spin–orbit coupling and superconductivity at the $SrTiO_3$/$LaAlO_3$ interface: a magnetotransport study,* Physical Review Letters **104**, 126802 (2010).

[49] E. Maniv, M. B. Shalom, A. Ron, M. Mograbi, A. Palevski, M. Goldstein, and Y. Dagan, *Strong correlations elucidate the electronic structure and phase diagram of $LaAlO_3$/$SrTiO_3$ interface,* Nature Communications **6**, 8239 (2015).

[50] C. Richter, H. Boschker, W. Dietsche, E. Fillis-Tsirakis, R. Jany, F. Loder, L. F. Kourkoutis, D. A. Muller, J. R. Kirtley, C. W. Schneider, and J. Mannhart, *Interface superconductor with gap behaviour like a high-temperature superconductor,* Nature **502**, 528 (2013).

[51] A. Brinkman, M. Huijben, M. Van Zalk, J. Huijben, U. Zeitler, J. C. Maan, W. G. van der Wiel, G. J. H. M. Rijnders, D. H. A. Blank, and H. Hilgenkamp, *Magnetic effects at the interface between non-magnetic oxides,* Nature Materials **6**, 493 (2007).

[52] J. A. Bert, B. Kalisky, C. Bell, M. Kim, Y. Hikita, H. Y. Hwang, and K. A. Moler, *Direct imaging of the coexistence of ferromagnetism and superconductivity at the $LaAlO_3$/$SrTiO_3$ interface,* Nature Physics **7**, 767 (2011).

[53] L. Li, C. Richter, J. Mannhart, and R. C. Ashoori, *Coexistence of magnetic order and*

two-dimensional superconductivity at $LaAlO_3/SrTiO_3$ interfaces, Nature Physics **7**, 762 (2011).

[54] B. Kalisky, J. A. Bert, B. B. Klopfer, C. Bell, H. K. Sato, M. Hosoda, H. Y. Hikita, Y.and Hwang, and K. A. Moler, *Critical thickness for ferromagnetism in $LaAlO_3/SrTiO_3$ heterostructures,* Nature Communications **3**, 922 (2012).

[55] M. B. Shalom, C. W. Tai, Y. Lereah, M. Sachs, E. Levy, D. Rakhmilevitch, A. Palevski, and Y. Dagan, *Anisotropic magnetotransport at the $LaAlO_3/SrTiO_3$ interface,* Physical Review B **80**, 140403 (2009).

[56] X. Wang, W. M. Lü, A. Annadi, Z. Q. Liu, K. Gopinadhan, S. Dhar, T. Venkatesan, and Ariando, *Magnetoresistance of two-dimensional and three-dimensional electron gas in $LaAlO_3/SrTiO_3$ heterostructures: Influence of magnetic ordering, interface scattering, and dimensionality,* Physical Review B **84**, 075312 (2011).

[57] A. Joshua, J. Ruhman, S. Pecker, E. Altman, and S. Ilani, *Gate-tunable polarized phase of two-dimensional electrons at the $LaAlO_3/SrTiO_3$ interface,* Proceedings of the National Academy of Sciences **110**, 9633 (2013).

[58] J. Ruhman, A. Joshua, S. Ilani, and E. Altman, *Competition between Kondo screening and magnetism at the $LaAlO_3/SrTiO_3$ interface,* Physical Review B **90**, 125123 (2014).

[59] M. Trushin, K. Výborný, P. Moraczewski, A. A. Kovalev, J. Schliemann, and T. Jungwirth, *Anisotropic magnetoresistance of spin–orbit coupled carriers scattered from polarized magnetic impurities,* Physical Review B **80**, 134405 (2009).

[60] E. Flekser, M. B. Shalom, M. Kim, C. Bell, Y. Hikita, H. Y. Hwang, and Y. Dagan, *Magnetotransport effects in polar versus non-polar $SrTiO_3$ based heterostructures,* Physical Review B **86**, 121104 (2012).

[61] A. Fête, S. Gariglio, A. D. Caviglia, J.-M. Triscone, and M. Gabay, *Rashba induced magnetoconductance oscillations in the $LaAlO_3$-$SrTiO_3$ heterostructure,* Physical Review B **86**, 201105 (2012).

[62] S. Caprara, F. Peronaci, and M. Grilli, *Intrinsic instability of electronic interfaces with strong Rashba coupling,* Physical Review Letters **109**, 196401 (2012).

[63] D. Bucheli, M. Grilli, F. Peronaci, G. Seibold, and S. Caprara, *Phase diagrams of voltage-gated oxide interfaces with strong Rashba coupling,* Physical Review B **89**, 195448 (2014).

[64] L. F. Mattheiss, *Energy bands for $KNiF_3$, $SrTiO_3$, $KMoO_3$, and $KTaO_3$,* Physical Review B **6**, 4718 (1972).

[65] A. F. Santander-Syro, O. Copie, T. Kondo, F. Fortuna, S. Pailhes, R. Weht, X. G. Qiu, F. Bertran, A. Nicolaou, A. Taleb-Ibrahimi, P. Le Fèvre, G. Herranz, M. Bibes, N. Reyren, Y. Apertet, P. Lecoeur, A. Barthélémy, and M. J. Rozenberg, *Two-dimensional electron gas with universal subbands at the surface of $SrTiO_3$,* Nature **469**, 189 (2011).

[66] Z. Zhong, A. Tóth, and K. Held, *Theory of spin–orbit coupling at $LaAlO_3/SrTiO_3$*

interfaces and $SrTiO_3$ surfaces, Physical Review B **87**, 161102 (2013).

[67] K. V. Shanavas, Z. S. Popović, and S. Satpathy, *Theoretical model for Rashba spin–orbit interaction in d electrons,* Physical Review B **90**, 165108 (2014).

[68] N. C. Plumb, M. Salluzzo, E. Razzoli, M. Månsson, M. Falub, J. Krempasky, C. E. Matt, J. Chang, M. Schulte, J. Braun, H. Ebert, J. Minár, B. Delley, K.-J. Zhou, T. Schmitt, M. Shi, J. Mesot, L. Patthey, and M. Radović, *Mixed dimensionality of confined conducting electrons in the surface region of $SrTiO_3$,* Physical Review Letters **113**, 086801 (2014).

[69] A. Fête, S. Gariglio, C. Berthod, D. Li, D. Stornaiuolo, M. Gabay, and J.-M. Triscone, *Large modulation of the Shubnikov–de Haas oscillations by the Rashba interaction at the $LaAlO_3/SrTiO_3$ interface,* New Journal of Physics **16**, 112002 (2014).

[70] J. M. Ziman, *Approximate calculation of the anisotropy of the relaxation time of the conduction electrons in the noble metals,* Physical Review **121**, 1320 (1961).

[71] J. M. Ziman, *Principles of the Theory of Solids* (Cambridge university press, 1972).

[72] D. I. Pikulin, C.-Y. Hou, and C. W. J. Beenakker, *Nernst effect beyond the relaxation-time approximation,* Physical Review B **84**, 035133 (2011).

[73] S. Thiel, C. W. Schneider, L. F. Kourkoutis, D. A. Muller, N. Reyren, A. D. Caviglia, S. Gariglio, J.-M. Triscone, and J. Mannhart, *Electron scattering at dislocations in $LaAlO_3/SrTiO_3$ interfaces,* Physical Review Letters **102**, 046809 (2009).

[74] M. H. Fischer, S. Raghu, and E.-A. Kim, *Spin–orbit coupling in $LaAlO_3/SrTiO_3$ interfaces: magnetism and orbital ordering,* New Journal of Physics **15**, 023022 (2013).

[75] A. M. R. V. L. Monteiro, D. J. Groenendijk, N. Manca, E. Mulazimoglu, S. Goswami, Y. Blanter, L. M. K. Vandersypen, and A. D. Caviglia, *Side gate tunable Josephson junctions at the $LaAlO_3/SrTiO_3$ interface,* Nano Letters **17**, 715 (2017).

[76] C. Cen, S. Thiel, J. Mannhart, and J. Levy, *Oxide nanoelectronics on demand,* Science **323**, 1026 (2009).

[77] B. Kalisky, E. M. Spanton, H. Noad, J. R. Kirtley, K. C. Nowack, C. Bell, H. K. Sato, M. Hosoda, Y. Xie, Y. Hikita, C. Woltmann, G. Pfanzelt, R. Jany, C. Richter, H. Y. Hwang, J. Mannhart, and K. A. Moler, *Locally enhanced conductivity due to the tetragonal domain structure in $LaAlO_3/SrTiO_3$ heterointerfaces,* Nature Materials **12**, 1091 (2013).

[78] M. Honig, J. A. Sulpizio, J. Drori, A. Joshua, E. Zeldov, and S. Ilani, *Local electrostatic imaging of striped domain order in $LaAlO_3/SrTiO_3$,* Nature Materials **12**, 1112 (2013).

[79] J. A. Bert, K. C. Nowack, B. Kalisky, H. Noad, J. R. Kirtley, C. Bell, H. K. Sato, M. Hosoda, Y. Hikita, H. Y. Hwang, and K. A. Moler, *Gate-tuned superfluid density at the superconducting $LaAlO_3/SrTiO_3$ interface,* Physical Review B **86**, 060503 (2012).

[80] C. Bell, S. Harashima, Y. Kozuka, M. Kim, B. G. Kim, Y. Hikita, and H. Y. Hwang,

Dominant mobility modulation by the electric field effect at the LaAlO$_3$/SrTiO$_3$ interface, Physical Review Letters **103**, 226802 (2009).

[81] G. Cheng, M. Tomczyk, S. Lu, J. P. Veazey, M. Huang, P. Irvin, S. Ryu, H. Lee, C.-B. Eom, C. S. Hellberg, and J. Levy, *Electron pairing without superconductivity,* Nature **521**, 196 (2015).

[82] K. Michaeli, A. C. Potter, and P. A. Lee, *Superconducting and ferromagnetic phases in SrTiO$_3$/LaAlO$_3$ oxide interface structures: possibility of finite momentum pairing,* Physical Review Letters **108**, 117003 (2012).

[83] B. Liu and X. Hu, *Local electronic structure of the superconducting interface LaAlO$_3$/SrTiO$_3$,* Physical Review B **81**, 144504 (2010).

[84] S. Banerjee, O. Erten, and M. Randeria, *Ferromagnetic exchange, spin–orbit coupling and spiral magnetism at the LaAlO$_3$/SrTiO$_3$ interface,* Nature Physics **9**, 626 (2013).

[85] P. Gallagher, M. Lee, J. R. Williams, and D. Goldhaber-Gordon, *Gate-tunable superconducting weak link and quantum point contact spectroscopy on a strontium titanate surface,* Nature Physics **10**, 748 (2014).

[86] S. Goswami, E. Mulazimoglu, L. M. K. Vandersypen, and A. D. Caviglia, *Nanoscale electrostatic control of oxide interfaces,* Nano Letters **15**, 2627 (2015).

[87] V. V. Bal, M. M. Mehta, S. Ryu, C. M. Lee, H. ans Folkman, C. B. Eom, and V. Chandrasekhar, *Gate-tunable superconducting weak link behavior in top-gated LaAlO$_3$/SrTiO$_3$,* Appplied Physics Letters **106**, 212601 (2015).

[88] S. Goswami, E. Mulazimoglu, A. M. R. V. L. Monteiro, R. Wölbing, D. Koelle, R. Kleiner, Y. M. Blanter, L. M. K. Vandersypen, and A. D. Caviglia, *Quantum interference in an interfacial superconductor,* Nature Nanotechnology **11**, 861 (2016).

[89] W. Dai, S. Adhikari, A. C. Garcia-Castro, A. H. Romero, H. Lee, J.-W. Lee, S. Ryu, C.-B. Eom, and C. Cen, *Tailoring LaAlO$_3$/SrTiO$_3$ interface metallicity by oxygen surface adsorbates,* Nano Letters **16**, 2739 (2016).

[90] Y. Xie, Y. Hikita, C. Bell, and H. Y. Hwang, *Control of electronic conduction at an oxide heterointerface using surface polar adsorbates,* Nature Communications **2**, 494 (2011).

[91] E. Lesne, N. Reyren, D. Doennig, R. Mattana, H. Jaffrès, V. Cros, F. Petroff, F. Choueikani, P. Ohresser, R. Pentcheva, A. Barthélémy, and M. Bibes, *Suppression of the critical thickness threshold for conductivity at the LaAlO$_3$/SrTiO$_3$ interface,* Nature Communications **5**, 4291 (2014).

[92] A. Kristensen, H. Bruus, A. E. Hansen, J. B. Jensen, P. E. Lindelof, C. J. Marckmann, J. Nygård, C. B. Sørensen, F. Beuscher, A. Forchel, and M. Michel, *Bias and temperature dependence of the 0.7 conductance anomaly in quantum point contacts,* Physical Review B **62**, 10950 (2000).

[93] C. W. Schneider, S. Thiel, G. Hammerl, C. Richter, and J. Mannhart, *Microlithography of electron gases formed at interfaces in oxide heterostructures,* Applied Physics

Letters **89**, 122101 (2006).

[94] N. Banerjee, M. Huijben1, G. Koster, and G. Rijnders, *Direct patterning of functional interfaces in oxide heterostructures,* Applied Physics Letters **100**, 041601 (2012).

[95] L. D. Landau, E. M. Lifshitz, and L. P. Pitaevskii, *Electrodynamics of continuous media*, 2nd ed., Vol. 8 (Elsevier, 1981).

[96] C. Ang and Z. Yu, *dc electric-field dependence of the dielectric constant in polar dielectrics: Multipolarization mechanism model,* Phyical Review B **69**, 174109 (2004).

[97] D. Stornaiuolo, S. Gariglio, A. Fête, M. Gabay, D. Li, D. Massarotti, and J.-M. Triscone, *Weak localization and spin–orbit interaction in side-gate field effect devices at the $LaAlO_3$/$SrTiO_3$ interface,* Physical Review B **90**, 235426 (2014).

[98] P. A. Lee, A. D. Stone, and H. Fukuyama, *Universal conductance fluctuations in metals: Effects of finite temperature, interactions, and magnetic field,* Physical Review B **35**, 1039 (1987).

[99] D. Stornaiuolo, S. Gariglio, N. J. G. Couto, A. Fête, A. D. Caviglia, G. Seyfarth, D. Jaccard, A. F. Morpurgo, and J.-M. Triscone, *In-plane electronic confinement in superconducting $LaAlO_3$/$SrTiO_3$ nanostructures,* Applied Physics Letters **101**, 222601 (2012).

[100] C. W. J. Beenakker, *Universal limit of critical-current fluctuations in mesoscopic Josephson junctions,* Physical Review Letters **67**, 3836 (1991).

[101] N. Reyren, S. Gariglio, A. D. Caviglia, D. Jaccard, T. Schneider, and J.-M. Triscone, *Anisotropy of the superconducting transport properties of the $LaAlO_3$/$SrTiO_3$ interface,* Applied Physics Letters **94**, 112506 (2009).

[102] B. L. Al'tshuler and B. Z. Spivak, *Mesoscopic fluctuations in a superconductor–normal metal–superconductor junction,* Soviet Physics JETP **65**, 343 (1987).

[103] D. Rakhmilevitch, M. B. Shalom, M. Eshkol, A. Tsukernik, A. Palevski, and Y. Dagan, *Phase coherent transport in $SrTiO_3$/$LaAlO_3$ interfaces,* Physical Review B **82**, 235119 (2010).

[104] A. M. R. V. L. Monteiro, D. J. Groenendijk, I. Groen, J. de Bruijckere, R. Gaudenzi, H. S. J. van der Zant, and A. D. Caviglia, *Two-dimensional superconductivity at the (111) $LaAlO_3$/$SrTiO_3$ interface,* Physical Review B **96**, 020504 (2017).

[105] S. Thiel, G. Hammerl, A. Schmehl, C. W. Schneider, and J. Mannhart, *Tunable quasi-two-dimensional electron gases in oxide heterostructures,* Science **313**, 1942 (2006).

[106] C. Cen, S. Thiel, G. Hammerl, C. W. Schneider, K. E. Andersen, C. S. Hellberg, J. Mannhart, and J. Levy, *Nanoscale control of an interfacial metal–insulator transition at room temperature,* Nature Materials **7**, 298 (2008).

[107] G. Herranz, G. Singh, N. Bergeal, A. Jouan, J. Lesueur, M. Gázquez, J.and Varela, M. Scigaj, N. Dix, F. Sánchez, and J. Fontcuberta, *Engineering two-dimensional su-*

perconductivity and Rashba spin–orbit coupling in $LaAlO_3$/$SrTiO_3$ quantum wells by selective orbital occupancy, Nature Communications **6**, 6028 (2015).

[108] D. Xiao, W. Zhu, Y. Ran, N. Nagaosa, and S. Okamoto, *Interface engineering of quantum Hall effects in digital transition metal oxide heterostructures,* Nature Communications **2**, 596 (2011).

[109] G. Herranz, F. Sánchez, N. Dix, M. Scigaj, and J. Fontcuberta, *High mobility conduction at (110) and (111) $LaAlO_3$/$SrTiO_3$ interfaces,* Scientific Reports **2**, 758 (2012).

[110] T. C. Rödel, C. Bareille, F. Fortuna, C. Baumier, F. Bertran, P. Le Fèvre, M. Gabay, O. Hijano Cubelos, M. J. Rozenberg, T. Maroutian, P. Lecoeur, and A. F. Santander-Syro, *Orientational tuning of the fermi sea of confined electrons at the $SrTiO_3$ (110) and (111) surfaces,* Physical Review Applied **1**, 051002 (2014).

[111] S. McKeown Walker, A. de la Torre, F. Y. Bruno, A. Tamai, T. K. Kim, M. Hoesch, M. Shi, M. S. Bahramy, P. D. C. King, and F. Baumberger, *Control of a two-dimensional electron gas on $SrTiO_3$(111) by atomic oxygen,* Physical Review Letters **113**, 177601 (2014).

[112] L. Miao, R. Du, Y. Yin, and Q. Li, *Anisotropic magneto-transport properties of electron gases at $SrTiO_3$ (111) and (110) surfaces,* Applied Physics Letters **109**, 261604 (2016).

[113] P. K. Rout, I. Agireen, E. Maniv, M. Goldstein, and Y. Dagan, *Six-fold crystalline anisotropic magnetoresistance in the (111) $LaAlO_3$/$SrTiO_3$ oxide interface,* Physical Review B **95**, 241107 (2017).

[114] M. S. Scheurer, D. F. Agterberg, and J. Schmalian, *Selection rules for Cooper pairing in two-dimensional interfaces and sheets,* npj Quantum Materials **9**, 2 (2017).

[115] S. K. Davis, Z. Huang, K. Han, T. Venkatesan, and V. Chandrasekhar, *Electrical transport anisotropy controlled by oxygen vacancy concentration in (111) $LaAlO_3$/$SrTiO_3$ interface structures,* Advanced Materials Interfaces **4** (2017).

[116] J. M. Kosterlitz and D. J. Thouless, *Long range order and metastability in two dimensional solids and superfluids (application of dislocation theory),* Journal of Physics C: Solid State Physics **5**, L124 (1972).

[117] J. M. Kosterlitz and D. J. Thouless, *Ordering, metastability and phase transitions in two-dimensional systems,* Journal of Physics C: Solid State Physics **6**, 1181 (1973).

[118] Y.-L. Han, S.-C. Shen, J. You, H.-O. Li, Z.-Z. Luo, G.-L. Li, C.-J.and Qu, C.-M. Xiong, R.-F. Dou, L. He, D. Naugle., G.-P. Guo, and J. C. Nie, *Two-dimensional superconductivity at (110) $LaAlO_3$/$SrTiO_3$ interfaces,* Applied Physics Letters **105**, 192603 (2014).

[119] H. Noad, E. M. Spanton, K. C. Nowack, H. Inoue, M. Kim, T. A. Merz, C. Bell, Y. Hikita, R. Xu, W. Liu, *et al.*, *Variation in superconducting transition temperature due to tetragonal domains in two-dimensionally doped $SrTiO_3$,* Physical Review B **94**, 174516 (2016).

[120] P. G. Baity, X. Shi, Z. Shi, L. Benfatto, and D. Popović, *Effective two-dimensional thickness for the Berezinskii–Kosterlitz–Thouless-like transition in a highly underdoped $La_{2-x}Sr_xCuO_4$*, Physical Review B **93**, 024519 (2016).

[121] B. Chandrasekhar, *A note on the maximum critical field of high-field superconductors,* Applied Physics Letters **1**, 7 (1962).

[122] A. Clogston, *Upper limit for the critical field in hard superconductors,* Physical Review Letters **9**, 266 (1962).

[123] M. Kim, Y. Kozuka, C. Bell, Y. Hikita, and H. Hwang, *Intrinsic spin–orbit coupling in superconducting δ-doped $SrTiO_3$ heterostructures,* Physical Review B **86**, 085121 (2012).

[124] Y. Lu, T. Takayama, A. F. Bangura, Y. Katsura, D. Hashizume, and H. Takagi, *Superconductivity at 6K and the violation of Pauli limit in $Ta_2Pd_xS_5$*, Journal of the Physical Society of Japan **83**, 023702 (2013).

[125] S. Khim, B. Lee, J. W. Kim, E. S. Choi, G. R. Stewart, and K. H. Kim, *Pauli-limiting effects in the upper critical fields of a clean LiFeAs single crystal,* Physical Review B **84**, 104502 (2011).

[126] H. J. Gardner, A. Kumar, L. Yu, P. Xiong, M. P. Warusawithana, L. Wang, O. Vafek, and D. G. Schlom, *Enhancement of superconductivity by a parallel magnetic field in two-dimensional superconductors,* Nature Physics **7**, 895 (2011).

[127] K. Maki, *Effect of Pauli paramagnetism on magnetic properties of high-field superconductors,* Physical Review **148**, 362 (1966).

[128] S. Maekawa and H. Fukuyama, *Magnetoresistance in two-dimensional disordered systems: effects of Zeeman splitting and spin–orbit scattering,* Journal of the Physical Society of Japan **50**, 2516 (1981).

[129] A. M. R. V. L. Monteiro, M. Vivek, D. J. Groenendijk, P. Bruneel, I. Leermakers, U. Zeitler, M. Gabay, and A. D. Caviglia, *Band inversion driven by electronic correlations at the (111) $LaAlO_3/SrTiO_3$ interface,* arXiv:1808.03063 (2018).

[130] E. Dagotto, *Complexity in strongly correlated electronic systems,* Science **309**, 257 (2005).

[131] D. Pesquera, P. Scigaj, M .and Gargiani, A. Barla, J. Herrero-Martín, E. Pellegrin, S. Valvidares, J. Gázquez, M. Varela, N. Dix, J. Fontcuberta, F. Sánchez, and G. Herranz, *Two-dimensional electron gases at $LaAlO_3/SrTiO_3$ interfaces: orbital symmetry and hierarchy engineered by crystal orientation,* Physical Review Letters **113**, 156802 (2014).

[132] D. Doennig, W. E. Pickett, and R. Pentcheva, *Massive symmetry breaking in $LaAlO_3/SrTiO_3$ (111) quantum wells: A three-orbital strongly correlated generalization of graphene,* Physical Review Letters **111**, 126804 (2013).

[133] S. Davis, Z. Huang, K. Han, T. Venkatesan, and V. Chandrasekhar, *Magnetoresistance in the superconducting state at the (111) $LaAlO_{3/}SrTiO_3$ interface,* Physical Review B **96**, 134502 (2017).

[134] P. K. Rout, E. Maniv, and Y. Dagan, *Link between the superconducting dome and spin–orbit interaction in the (111) LaAlO$_3$/SrTiO$_3$ interface,* Phys. Rev. Lett. **119**, 237002 (2017).

[135] S. Davis, V. Chandrasekhar, Z. Huang, K. Han, and T. Venkatesan, *Anisotropic multicarrier transport at the (111)LaAlO$_3$/SrTiO$_3$ interface,* Physical Review B **95**, 035127 (2017).

[136] M. Reinle-Schmitt, C. Cancellieri, D. Li, D. Fontaine, M. Medarde, E. Pomjakushina, C. Schneider, S. Gariglio, P. Ghosez, J.-M. Triscone, and P. Willmott, *Tunable conductivity threshold at polar oxide interfaces,* Nature Communications **3**, 932 (2012).

[137] G. Herranz, F. Sánchez, N. Dix, and J. Scigaj, M.and Fontcuberta, *High mobility conduction at (110) and (111) LaAlO$_3$/SrTiO$_3$ interfaces,* Scientific Reports **2**, 758 (2012).

[138] G. Drera, G. Salvinelli, A. Brinkman, M. Huijben, G. Koster, H. Hilgenkamp, G. Rijnders, D. Visentin, and L. Sangaletti, *Band offsets and density of Ti^{3+} states probed by X-ray photoemission on LaAlO$_3$/SrTiO$_3$ heterointerfaces and their LaAlO$_3$ and SrTiO$_3$ bulk precursors,* Physical Review B **87**, 075435 (2013).

[139] G. Berner, A. Müller, F. Pfaff, J. Walde, C. Richter, J. Mannhart, S. Thiess, A. Gloskovskii, W. Drube, M. Sing, and R. Claessen, *Band alignment in LaAlO$_3$/SrTiO$_3$ oxide heterostructures inferred from hard X-ray photoelectron spectroscopy,* Physical Review B **88**, 115111 (2013).

[140] V. N. Strocov, C. Cancellieri, and A. S. Mishchenko, *Electrons and polarons at oxide interfaces explored by soft-X-ray ARPES,* in *Spectroscopy of Complex Oxide Interfaces* (Springer, 2018) pp. 107–151.

[141] S. Hikami, A. Larkin, and Y. Nagaoka, *Spin–orbit interaction and magnetoresistance in the two dimensional random system,* Progress of Theoretical Physics **63**, 707 (1980).

[142] H. Liang, L. Cheng, L. Wei, Z. Luo, G. Yu, C. Zeng, and Z. Zhang, *Nonmonotonically tunable Rashba spin–orbit coupling by multiple-band filling control in SrTiO$_3$-based interfacial d-electron gases,* Physical Review B **92**, 075309 (2015).

[143] G. Khalsa, B. Lee, and A. H. MacDonald, *Theory of t_{2g} electron-gas Rashba interactions,* Physical Review B **88**, 041302 (2013).

[144] S. McKeown Walker, A. de la Torre, F. Y. Bruno, A. Tamai, T. K. Kim, M. Hoesch, M. Shi, M. S. Bahramy, P. D. C. King, and F. Baumberger, *Control of a two-dimensional electron gas on SrTiO$_3$(111) by atomic oxygen,* Physical Review Letters **113**, 177601 (2014).

[145] T. C. Rödel, C. Bareille, F. Fortuna, C. Baumier, F. Bertran, P. Le Fèvre, M. Gabay, O. Hijano Cubelos, M. J. Rozenberg, T. Maroutian, P. Lecoeur, and A. F. Santander-Syro, *Orientational tuning of the Fermi sea of confined electrons at the SrTiO$_3$ (110) and (111) surfaces,* Physical Review Applied **1**, 051002 (2014).

[146] K. S. Novoselov, A. K. Geim, S. V. Morozov, D. Jiang, M. I. Katsnelson, I. V. Grigorieva, S. V. Dubonos, and A. A. Firsov, *Two-dimensional gas of massless Dirac fermions in graphene,* Nature **438**, 197 (2005).

[147] K. S. Novoselov, A. K. Geim, S. V. Morozov, D. A. Jiang, Y. Zhang, S. V. Dubonos, I. V. Grigorieva, and A. A. Firsov, *Electric field effect in atomically thin carbon films,* Science **306**, 666 (2004).

[148] Q. H. Wang, K. Kalantar-Zadeh, A. Kis, J. N. Coleman, and M. S. Strano, *Electronics and optoelectronics of two-dimensional transition metal dichalcogenides,* Nature Nanotechnology **7**, 699 (2012).

[149] A. Castellanos-Gomez, L. Vicarelli, E. Prada, J. O. Island, K. L. Narasimha-Acharya, S. I. Blanter, D. J. Groenendijk, M. Buscema, G. A. Steele, J. V. Alvarez, H. W. J Zandbergen, J. J. Palacios, and H. S. J. van der Zant, *Isolation and characterization of few-layer black phosphorus,* 2D Materials **1**, 025001 (2014).

[150] L. Song, L. Ci, H. Lu, P. B. Sorokin, C. Jin, J. Ni, A. G. Kvashnin, D. G. Kvashnin, J. Lou, B. I. Yakobson, and P. M. Ajayan, *Large scale growth and characterization of atomic hexagonal boron nitride layers,* Nano Letters **10**, 3209 (2010).

[151] C. Gong, L. Li, Z. Li, H. Ji, A. Stern, Y. Xia, T. Cao, W. Bao, C. Wang, Y. Wang, Z. Q. Qiu, R. J. Cava, S. G. Louie, J. Xia, and X. Zhang, *Discovery of intrinsic ferromagnetism in two-dimensional van der Waals crystals,* Nature **546**, 265 (2017).

[152] B. Huang, G. Clark, E. Navarro-Moratalla, D. R. Klein, R. Cheng, K. L. Seyler, D. Zhong, E. Schmidgall, M. A. McGuire, D. H. Cobden, W. Yao, D. Xiao, P. Jarillo-Herrero, and X. Xu, *Layer-dependent ferromagnetism in a van der Waals crystal down to the monolayer limit,* Nature **546**, 270 (2017).

[153] C. Tan, J. Lee, S.-G. Jung, T. Park, S. Albarakati, M. R. Partridge, J.and Field, D. G. McCulloch, L. Wang, and C. Lee, *Hard magnetic properties in nanoflake van der Waals* Fe_3GeTe_2*,* Nature Communications **9**, 1554 (2018).

[154] Y. Tokura and N. Nagaosa, *Orbital physics in transition-metal oxides,* Science **288**, 462 (2000).

[155] D. Lu, D. J. Baek, S. S. Hong, L. F. Kourkoutis, Y. Hikita, and H. Y. Hwang, *Synthesis of freestanding single-crystal perovskite films and heterostructures by etching of sacrificial water-soluble layers,* Nature Materials **15**, 1255 (2016).

[156] Q. Gan, R. A. Rao, C. B. Eom, J. L. Garrett, and M. Lee, *Direct measurement of strain effects on magnetic and electrical properties of epitaxial* $SrRuO_3$ *thin films,* Applied Physics Letters **72**, 978 (1998).

[157] R. Paskiewicz, D. M.and Sichel-Tissot, E. Karapetrova, L. Stan, and D. D. Fong, *Single-crystalline* $SrRuO_3$ *nanomembranes: a platform for flexible oxide electronics,* Nano Letters **16**, 534 (2015).

[158] A. Castellanos-Gomez, M. Buscema, R. Molenaar, V. Singh, L. Janssen, H. S. J. van der Zant, and G. A. Steele, *Deterministic transfer of two-dimensional materials by all-dry viscoelastic stamping,* 2D Materials **1**, 011002 (2014).

[159] C.-B. Eom, R. J. Cava, R. M. Fleming, J. M. Phillips, J. H. Marshall, J. W. P. Hsu, J. J. Krajewski, and W. F. Peck, *Single-crystal epitaxial thin films of the isotropic metallic oxides* $Sr_{1-x}Ca_xRuO_3$ $(0 < x < 1)$, Science **258**, 1766 (1992).

[160] G. Koster, L. Klein, W. Siemons, G. Rijnders, J. S. Dodge, C.-B. Eom, D. H. A. Blank, and M. R. Beasley, *Structure, physical properties, and applications of* $SrRuO_3$ *thin films,* Reviews of Modern Physics **84**, 253 (2012).

[161] D. Kan, R. Aso, H. Kurata, and Y. Shimakawa, *Epitaxial strain effect in tetragonal* $SrRuO_3$ *thin films,* Journal of Applied Physics **113**, 173912 (2013).

[162] W. Lu, W. Song, P. Yang, J. Ding, G. M. Chow, and J. Chen, *Strain engineering of octahedral rotations and physical properties of* $SrRuO_3$ *films,* Scientific Reports **5**, 10245 (2015).

[163] X. Shen, X. Qiu, D. Su, S. Zhou, A. Li, and D. Wu, *Thickness-dependent metal–insulator transition in epitaxial* $SrRuO_3$ *ultrathin films,* Journal of Applied Physics **117**, 015307 (2015).

[164] N. Nagaosa, J. Sinova, S. Onoda, A. H. MacDonald, and N. P. Ong, *Anomalous Hall Effect,* Reviews of Modern Physics **82**, 1539 (2010).

[165] Z. Fang, N. Nagaosa, K. S. Takahashi, A. Asamitsu, R. Mathieu, T. Ogasawara, H. Yamada, M. Kawasaki, Y. Tokura, and K. Terakura, *The anomalous Hall effect and magnetic monopoles in momentum space,* Science **302**, 92 (2003).

[166] C. U. Jung, H. Yamada, M. Kawasaki, and Y. Tokura, *Magnetic anisotropy control of* $SrRuO_3$ *films by tunable epitaxial strain,* Applied Physics Letters **84**, 2590 (2004).

[167] S. H. Chang, Y. J. Chang, S. Y. Jang, D. W. Jeong, C. U. Jung, Y.-J. Kim, J.-S. Chung, and T. W. Noh, *Thickness-dependent structural phase transition of strained* $SrRuO_3$ *ultrathin films: the role of octahedral tilt,* Physical Review B **84**, 104101 (2011).

[168] J. Matsuno, N. Ogawa, K. Yasuda, F. Kagawa, W. Koshibae, N. Nagaosa, Y. Tokura, and M. Kawasaki, *Interface-driven topological Hall effect in* $SrRuO_3$*-*$SrIrO_3$ *bilayer,* Science Advances **2**, e1600304 (2016).

[169] B. Pang, L. Zhang, Y. Chen, J. Zhou, S. Yao, S. Zhang, and Y. Chen, *Spin-glass-like behavior and topological Hall effect in* $SrRuO_3/SrIrO_3$ *superlattices for oxide spintronics applications,* ACS Applied Materials & Interfaces (2017).

[170] Y. Ohuchi, J. Matsuno, N. Ogawa, Y. Kozuka, M. Uchida, Y. Tokura, and M. Kawasaki, *Electric-field control of anomalous and topological Hall effects in oxide bilayer thin films,* Nature Communications **9**, 213 (2018).

CURRICULUM VITÆ

Mafalda MONTEIRO

26/03/1991 Born in Vila Real, Portugal.

EDUCATION

2003–2009 High School
Colégio de S. Gonçalo
Amarante, Portugal

2009–2014 Integrated Masters in Physics Engineering
Universidade do Porto
Porto, Portugal
Thesis: *Fundamental aspects of the 2-dimensional electron system at the $LaAlO_3$/$SrTiO_3$ interface*
Supervisors: Dr. A. D. Caviglia
Dr. J. A. Moreira

2015–2018 Ph.D. in Applied Physics
Delft University of Technology
Delft, The Netherlands
Thesis: *Quantum Transport at Oxide Interfaces*
Promotors: Dr. A. D. Caviglia
Prof. dr. ir. H. S. J. van der Zant

LIST OF PUBLICATIONS

16. D. Davidovikj, D. J. Groenendijk, **A. M. R. V. L. Monteiro**, A. Dijkhoff, D. Afanasiev, Y. Huang, E. van Heumen, H. S. J. van der Zant, A. D. Caviglia, and P. G. Steeneken, *Ultrathin complex oxide nanomechanical resonators*, under review.

15. **A. M. R. V. L. Monteiro**, M. Vivek, D. J. Groenendijk, P. Bruneel, I. Leermakers, U. Zeitler, M. Gabay, and A. D. Caviglia, *Band inversion driven by electronic correlations at the (111) $LaAlO_3/SrTiO_3$ interface*, arXiv:1808.03063, under review.

14. N. Manca, D. Bothner, **A. M. R. V. L. Monteiro**, D. Davidovikj, Y. G. Saglam, M. Jenkins, M. Gabay, G. Steele, A. D. Caviglia, *Bimodal phase diagram of the superfluid density in $LaAlO_3/SrTiO_3$ revealed by an interfacial waveguide resonator*, arXiv:1809.10993, accepted in Physical Review Letters.

13. **A. M. R. V. L. Monteiro**, A. D. Caviglia, and N. Reyren, *Transport properties of TMO interfaces*, Chapter 3 in "Spectroscopy of Transition-Metal Oxide Interfaces", Springer, ISBN: 978-3-319-74988-4, (2018).

12. S. Gariglio, M. Scheurer, J. Schmalian, **A. M. R. V. L. Monteiro**, S. Goswami, and A. D. Caviglia, *Surface and interface superconductivity*, Chapter 7 in "The Oxford Handbook of Small Superconductors", Oxford University Press, ISBN: 9780198738169, (2017).

11. D. J. Groenendijk, C. Autieri, J. Girovsky, M. Carmen Martinez-Velarte, N. Manca, G. Mattoni, **A. M. R. V. L. Monteiro**, N. Gauquelin, J. Verbeeck, A. F. Otte, M. Gabay, S. Picozzi, and A. D. Caviglia, *Spin–orbit semimetal $SrIrO_3$ in the two-dimensional limit*, Physical Review Letters, **119**, 256403 (2017).

10. **A. M. R. V. L. Monteiro**, D. J. Groenendijk, I. Groen, J. de Bruijckere, R. Gaudenzi, H. S. J. van der Zant, and A. D. Caviglia, *Two-dimensional superconductivity at the (111)$LaAlO_3/SrTiO_3$ interface*, Physical Review B, **96**, 020504(R) (2017).

9. **A. M. R. V. L. Monteiro**, D. J. Groenendijk, N. Manca , E. Mulazimoglu , S. Goswami, Ya. Blanter, L. M. K. Vandersypen, and A. D. Caviglia, *Side gate tunable Josephson junctions at the $LaAlO_3/SrTiO_3$ interface*, Nano Letters **17(2)**, 715720 (2017).

8. S. Goswami, E. Mulazimoglu, **A. M. R. V. L. Monteiro**, R. Wölbing, D. Koelle, R. Kleiner, Ya. M. Blanter, L. M. K. Vandersypen, and A. D. Caviglia, *Quantum interference in an interfacial superconductor*, Nature Nanotechnology **11**, 861865 (2016).

7. M. Diez, **A. M. R. V. L. Monteiro**, G. Mattoni, E. Cobanera, T. Hyart, E. Mulazimoglu, N. Bovenzi, C. W. J. Beenakker, and A. D. Caviglia, *Giant negative magnetoresistance driven by spin–orbit coupling at the $LaAlO_3/SrTiO_3$ interface*, Physical Review Letters **115**, 016803 (2015).

6. A. Avgoustidis, C. J. A. P. Martins, **A. M. R. V. L. Monteiro**, P. E. Vielzeuf, and G. Luzzi, *Cosmological effects of scalar–photon couplings: dark energy and varying-α models*, Journal of Cosmology and Astroparticle Physics **06**, 062 (2014).

5. R. P. J. Tilanus *et al.*, *Future mmVLBI Research with ALMA: A European vision*, arXiv:1406.4650 (2014).

4. M. C. Ferreira, O. Frigola, C. J. A. P. Martins, **A. M. R. V. L. Monteiro**, and J. Solà, *Consistency tests of the stability of fundamental couplings and unification scenarios*, Physical Review D **89**, 083011 (2014).

3. M. C. Ferreira, M. D. Julião, C. J. A. P. Martins, and **A. M. R. V. L. Monteiro**, *A test of unification towards the radio source PKS1413+135*, Physical Letters B **724**, 14 (2013).

2. M. C. Ferreira, M. D. Julião, C. J. A. P. Martins, and **A. M. R. V. L. Monteiro**, *Probing unification scenarios with atomic clocks*, Physical Review D **86**, 125025 (2012).

1. A. Avgoustidis, G. Luzzic, C. J. A. P. Martins, and **A. M. R. V. L. Monteiro**, *Constraints on the CMB temperature-redshift dependence from SZ and distance measurements*, Journal of Cosmology and Astroparticle Physics **02**, 013 (2012).

ACKNOWLEDGEMENTS

First and foremost, I would like to express my gratitude to my advisor and promotor Andrea Caviglia, who deserves thanks for many things. Notably, for creating the research environment in which I have performed my PhD research. He has provided guidance at key moments in my work while also allowing me to work independently the vast majority of the time. I am also grateful to my co-promotor Herre van der Zant, whose advice has helped me many times, even in matters beyond science.

I would like to extend my gratitude to the members of my doctoral committee: Yaroslav Blanter, Marc Gabay, Hans Hilgenkamp, Alix McCollam, Gervasi Herranz and Sander Otte. Thank you for reading my thesis, providing insightful feedback and being part of my committee. A special thanks to those who travelled from abroad to make it possible.

At TU Delft I have crossed paths with many PhD students, postdocs and PIs who have influenced and enhanced my research. Naturally, the direction and success of my PhD research has been strongly influenced by all the members of the Caviglia Lab. We shared beautiful scientific (and non-scientific) discussions, which I very much enjoyed. Being part of a young lab, I believe a special mention of those who joined before me is in order — namely Giordano and Emre, whose efforts in setting up the lab allowed me to hit the ground running. I wish you lots of success in your future scientific careers! Another important source of support throughout these years were the postdocs who joined the Caviglia Lab. Nicola and Dima, I appreciate all your guidance and advice. I hope one day you'll be leading your own labs and your future students can benefit from your wisdom. Jorrit and Thierry, two of the smartest people I have had the pleasure of working with, I am certain your PhDs will be very successful and I hope you have fun throughout. Thank you for all your patience while I practiced my Dutch at lunch! Yildiz, I wish you the best navigating between the worlds of oxides and resonators. Edouard, we have only worked together briefly, but I am glad to see the research on LAO/STO continuing in the hands of someone so capable, good luck! Dirk, we started the PhD on the very same day, and what a journey it was! We made many discoveries together, including the first free-standing oxides in our lab. Thank you for all the help and support! I have also learnt a lot by supervising Inge during her Master's project. I taught her the technical aspects of this field, but with her I learnt invaluable leadership lessons: how to foster trust, celebrate success and maintain motivation. It brings me immense joy to see you pursuing a PhD degree after our time working together.

Outside of Caviglia Lab, I must start by thanking my Paranymphs. João, it is hard to believe I have known you for ten years already, time does fly! There are so many stories which I will remember with great fondness, but I particularly liked how we used to tell other people "it's *our* birthday", making everyone confused! Thank you for always be-

ing there for me, you are an amazing friend! Davide, your kindness and generosity are your best qualities, please be sure to never change! Thank you for all the dinners, board games and absolutely delicious cakes. I truly wish you the best, which of course includes a cat in the near future!

Next I must thank my officemate of many years, Dejan. I hold you partially responsible for the fact that I have landed my dream job at the moment of this writing. Your job search adventure propelled me to start my own at a very early stage, so thank you for that! I am also grateful for all the discussions and the occasional Friday afternoon riddle which completely ruined my productivity! The *other* Balkan guy, Ranko. I am glad I got to know you well before you left the 3$^{\text{rd}}$ floor. Thank you for all the advice, I truly believe you have a lot of wisdom to share. Nikos, I wish you lots of success for the coming months, you are almost there! Thanks for all the nice parties, and for being Max's best staycation destination! Holger and Marc, please remember "Nein, nein, nein!!". Holger, it was a pleasure to see you being sucked into the oxides world, I hope you never leave! Marc, thank you for your amazing laughter, I didn't know it is actually possible to "laugh in German". Joeri, it was a pleasure to have worked with you, you are truly brilliant and I am sure a lot of success awaits during and after your PhD!

It is no overstatement to say that the Cleanroom was, for the first years of my PhD, my second home. As such, I am grateful to the technical staff of the Kavli Nanolab Delft for their help and support. I would also like to thank Tino and Ron, who brought into existence many of the Caviglia Lab's designs. A special thanks to Marijke and Etty, who work everyday behind the scenes to make QN such an enjoyable place.

Finally, this journey would not have been possible without the support of my family. I am forever grateful to my parents, who provided unconditional support and encouragement to pursue my interests from an early age, and to my sister Teresa, who is — and always will be — a role model in my life.